Design of Multifunctional Magnetic Nanostructures for Targeted Delivery of Anticancer Drugs

Thesis Submitted to

National Institute of Technology Rourkela

for the Degree of

Doctor of Philosophy

By

Smruti Ranjan Rout

Department of Chemistry
National Institute of Technology
Rourkela-769008

Dedicated to My Parents

CERTIFICATE

Dr.(Mrs.) Sasmita Mohapatra
Assistant Professor
Department of Chemistry
National Institute of Technology
Rourkela
Odisha-769008
India
Email: sasmitam@nitrkl.ac.in

This is to certify that the thesis entitled **"Design of Multifunctional Magnetic Nanostructures for Targeted Delivery of Anticancer Drugs"** being submitted by **Mr. Smruti Ranjan Rout** to the National Institute of Technology, Rourkela, Odisha, India, for the award of the degree of **Doctor of Philosophy** is a record of bonafide research work carried out by him under my supervision. I am satisfied that the thesis has reached the standard fulfilling the requirements of the regulations relating to the nature of the degree. The contents of the thesis have not been submitted to any other university or institute for the award of any degree**.**

Date: **Dr.(Mrs.) Sasmita Mohapatra**

NIT Rourkela

Acknowledgement

First of all, I would like to express my profound gratitude to my supervisor Prof. Sasmita Mohapatra for her excellent guidance, constant encouragement, continuous support, generous help and inspiration during the entire period of my research work. I would believe myself really fortunate to be associated with her at the important turn of my carrier.

I wish to express my sincere thanks to Prof. Sunil K. Sarangi, Director, NIT Rourkela for providing necessary facilities to carry out this research. I am grateful to Prof. Niranjan Panda, Head, Department of chemistry, NIT Rourkela for his valuable guidance and contribution to my scientific work at the time of requirement.

I sincerely thank my DSC members Prof. S. Mishra, Prof. G. Hota and Prof. S. Patel for their valuable suggestions during this program.

I wish to place on record my appreciation to numerous technical and nontechnical staffs of chemistry department, NIT, Rourkela who have lent their expertise and cooperation at various stages of this endeavor. Especially, I would like to mention Samir, Pratap and Arup, Department of Chemistry for their help during this program.

I am indebted to our collaborators, Prof. T.K. Maiti and Prof. S. K. Ghosh, Department of Biotechnology, IIT Kharagpur for their brilliant input in carrying out all biological work. I sincerely thank Dr. M. Majhi, Department of Radiodiagnosis, Ispat General Hospital, Rourkela for his unconditional support in performing MRI experiments. I owe my appreciation to Birendra Behera, Rajan Narayan and Santoshi Nayak for their cooperation.

It is a great pleasure for me to acknowledge all my lab mates Swagatika, Rahul, Ranjita and Mihir for being friendly, helpful and supportive throughout. I am highly gratified to Rahul and Ranjita for their help during last part of my thesis work.

I place on record my thankfulness to collogues and friends for making my stay in this campus a memorable one. Specially to Dinesh bahi and Sashi da.

A special thanks to my family members. Words cannot express how grateful I am to my parents, uncle, aunty, grandfather, brother and other family members for all of their support. Your prayer for me was what sustained me thus far.

Date: **Smruti Ranjan Rout**

NIT Rourkela, Odisha, India

Biography

Mr. Smruti Ranjan Rout was born on 8th July 1985 and grown up in Jagatsinghpur, Odisha, India. He has received his B.Sc. Degree with 1st class (Honors) in Chemistry in 2005 from Sarala Mahavidyalaya Rahama, Jagatsinghpur under Utkal University, Odisha. He has been awarded M.Sc. Degree with 1st class 1st in 2008 from Ganagadhar Meher Autonomous College Sambalpur under Sambalpur University, Odisha. After that he joined School of chemistry, Sambalpur University for his M. Phil. degree in Inorganic chemistry. He joined as a junior research fellow in DBT sponsored project at National Institute of Technology, Rourkela, Odisha, India, to pursue his doctoral research in 2010. During his doctoral studies, he has published several scientific papers in various international journals like *Journal of Material Chemistry, Dalton Transaction, Colloids and surfaces A: physicochemical engineering aspects, Tetrahedron Letters, Langmuir*. His research work has been presented in many national and international conferences. His research interest includes synthesis and characterization of functionalized magnetic nanostructures for biomedical applications.

Abstract

The present dissertation entitled, "***Design of Multifunctional Magnetic Nanostructures for Targeted Delivery of Anticancer Drugs***" is an embodiment of the investigations aimed at developing multifunctional magnetic nanoparticles intended for administration of some leading anticancer drugs and simultaneous monitoring of the treatment by imaging techniques. The possible diagnostic and therapeutic applications of these multifunctional nanosystems have been explored *in vitro.* The thesis has been divided into seven chapters.

Monodispersed amine functionalized MFe_2O_4 (M= Co, Mn, Ni) spherical nanoassemblies of size 35-50 nm have been prepared following simple solvochemical approach. The synthesis was accomplished by refluxing metal chloride precursors in ethylene glycol in presence of sodium acetate and ethanolamine. Due to large surface area, high density of amine groups and good aqueous dispersion stability these ferrites may serve as potential materials in biomedical application. Further, $CoFe_2O_4$ made by this method was conjugated to anticancer drug methotrexate or doxorubincin, marker molecule folic acid and a fluorescent marker molecule rhodamine isothiocyanate to develop a multifunctional nanoparticle. These drug loaded particles shows combined advantages of superparamagnetism, receptor mediated endocytosis and pH sensitive drug release behavior. Magnetic mesoporous amorphous calcium phosphate nanoparticles with a size of 62 nm and abundant –COOH groups on the surface have been prepared by a simple method. The presence of high surface area and large number of carboxylate groups, facilitate the incorporation of platinum pharmacophore cis-diaquadiamine platinum (II), folic acid and rhodamine isothiocyanate within its porous network. The cytotoxicity and

internalization efficiency of these nanocarriers have been evaluated on folate receptor overexpressed HeLa cells. These drug loaded nanoagents exhibit elevated cytotoxicity and induce apoptosis in HeLa cells. Furthermore development of theranostic mesoporous hollow silica nanospheres having therapeutic and diagnostic functions has been established. The internal space of the hollow spheres was utilised to clutch the hydrophobic anticancer drug pemetrexed and superparamagnetic $CoFe_2O_4$ nanoparticles while the external surface was chemically modified to grasp the platinum pharmacophore CDDP [cis-diaquadiamino platinum (II)], the marker molecule folic acid and the fluorescent dye RITC. Magnetic hollow spheres loaded with multiple therapeutic cargoes as well as magnetic resonance imaging (MRI) contrast agent exhibit enhanced cytotoxicity as compared to individual drugs. Simple inexpensive magnetic mesoporous carbon-based multimodal theranostic nanoagent best owed with magnetic targeting, T2 contrast behavior, fluorescence imaging, high loading and controlled release of the anticancer drug doxorubicin has been developed. Due to surface modification with carboxylic acid groups the nanoparticles are highly stable in aqueous buffer. The dual optical and magnetic properties of the mesoporous spheres may be utilized in advanced imaging technologies to track the curative responses. The transverse relaxivity value (r_2) of the drug absorbed particles was found to be 380.25 $mM^{-1}S^{-1}$.

Table of Contents

Chapter-1

A short review on multifunctional nanoparticles for multimodal imaging and therapy

1.1. Preface

The application of nanoparticles in biomedical field continues to be a growing field. The unique properties of nanoparticles based systems have been proven to be advantageous over pure molecular therapeutics as well as diagnostics.[1-3] The major applications of nanomaterials in the biomedical field can be mainly divided into imaging and therapy. Most of the clinically used imaging and therapeutic modalities are small molecules, such as the gadolinium complexes used as T1 magnetic resonance imaging (MRI) contrast agents and anticancer chemical drugs. The limitations of these small molecules are their very short blood circulation time and nonspecific biodistribution, which causes many unwanted side effects.[4] Nanostructured materials can be employed to overcome these limitations. For example, the blood circulation times can be increased significantly by the size control and surface modification. More recently, the combinations of various nanostructured materials with different properties have been explored which are capable to offer synergetic multifunctional nanomedical platforms, which make it possible to achieve simultaneous diagnosis and therapy.[5] Particularly, the synthesis of multifunctional magnetic nanoparticles is a highly active area of current research located at the interface between material science, biotechnology and medicine.[6-8] By virtue of their unique physical properties magnetic nanostructures have been revealed as potential agents in drug delivery, magnetic resonance imaging and hyperthermia. Moreover, the conjugation of targeting moieties on the surface of these multifunctional nanomaterials gives them specific targeted imaging and therapeutic properties. The unique characteristics of such multifunctional nanoparticles based systems lead to strategic advantages over pure molecular diagnostics as well as therapeutics.

However, the new intricacies owing to the integration of multiple functionalities must be explored to make the nanoparticle based applications a viable option to clinics. The successful development of multifunctional nanoparticles with

appropriate surface functionalization with regards to their therapeutic application is a contemporary challenge in this field. Our present investigation in this area deals with the development of multifunctional nanoparticles for simultaneous drug delivery, fluorescence imaging and magnetic resonance imaging by incorporating cobalt ferrite as the magnetic component in carrier matrix. In subsequent sections a brief overview on the characteristic properties of nanoparticles which make them advantageous for a wide range of biomedical applications, types of nanomaterials used in medical diagnosis as well as therapy and recent progresses in designing multifunctional magnetic nanoparticles for medical applications will be reviewed as it is relevant to our work.

1.2. Physical properties of nanomaterials

High surface to volume ratio

One of the most valuable properties of nanomaterials which makes them technologically important is their huge surface-to-volume ratio. In contrast to the extremely small surface to volume ratio of bulk materials and maximum for molecules, nanomaterials exhibit intermediate values which can effectively be controlled by tuning the size of the material. Novel properties of the nanomaterials arise from the large fraction of atoms which reside on the surface of the particle (e.g. for particle size of 100, 10 and 5 nm it corresponds to about 1-3 %, 15-30 %, and 30-60 % respectively) and from finite number of atoms in each crystalline core. Surface atoms have reduced coordination to the crystal backbone and more prone to react with the surroundings. Such high surface area and surface reactivity is very important for optimizing drug payloads and functionalization of the drug carrier. In addition, solid surface of the nanomaterials eliminates some of the folding and unfolding molecular arrangement taking place in biological as well as molecular systems thus provides high degree of control while designing physical chemistry to take place in the biological system.

Controlled shape and size

The function of nanoparticles in the biological system directly depends on the shape and size of nanoparticles. Applying different synthesis technique, a variety of nanostructures with numerous shapes and sizes can be prepared. Utilizing suitable growth upon different crystallographic facets and noble templates, a variety of shapes can be generated which include nanorods, nanoshells[9,10], nanoplates[11,12], nanoprisms[13], nanocubes[14-17], nanocages[18-21], and even nanostars.[22,23] Nanoparticles function in vivo, directly depends upon the shape of the particles. Many groups have already explored how cellular uptake is affected by the shape of nanoparticles.[24-26] Again, accumulation of NPs in the body depends upon the size of these nanostructures. Smaller the size of nanoparticles, quickly it can pass through the body's defense system and hence shows higher uptake. It has been already shown that larger size nanoparticles accumulate in areas of leaky vasculature by well-known phenomenon of the enhanced permeability and retention (EPR) effect.[27-29] Bawendi, Jain, and Fukamura has done some influential work and reported that nanoparticles with a hydrodynamic diameter smaller than 5.5 nm can effectively clear the renal system, offering a unique opportunity for balancing efficacy with minimal toxicity.[30] Furthermore, how cellular responses in vivo was affected by shape of nanoparticles was reported by Chan et.al in 2010.[31] Such investigations provide information regarding function of biological system at the nanoscale using the same material, and thus offering a crucial control for optimizing nonmedical platforms.

Optical properties

The optical properties of nanoparticles also play a vital role to optimize NP based technologies such as solar cells,[32-36] sensors,[37-42] catalysts,[43-49] and imaging agents.[50-54] For in vivo applications, the window in which light can penetrate tissue is relatively narrow. Optical inorganic nanomaterials can be mainly divided into two classes; semiconductor and metallic nanostructures. In both cases, the physical

confinement of the material in quantum-regime induces specific optical properties. For semiconductor materials, this ‘‘quantum effect’’ can be described by treating electronic excitation as a particle in a three dimensional box.[55] Thus a physical change in NP characteristics directly changes its electronic structure, enable in highly selective rational designs. The resulting change in absorption also corresponds to a shift in its photoluminescence (PL), allowing for effective ‘‘tuning’’ for a desired application. The strong absorption of light observed in case of metallic nanostructures due to an entirely different phenomenon known as the surface plasmon resonance (SPR).[56] For metal nanoparticle conduction electrons at the surface collectively oscillate with a corresponding excitation of a resonant wavelength of light. According to Mie theory, with an increase in NP size, the amount of light scattering due to the NP increases and variations in shape (nanorods, nanocubes, nanocages, nanoplates, etc.) lead to unique scattering properties.[57] The scattering is coupled to the unique SPR phenomenon of metallic nanostructures, resulting in a dramatic enhancement that can be used for biomedical imaging applications.

Magnetic Properties

When the size of a ferromagnetic particle is reduced below a threshold value, magneto-crystalline anisotropy (E_A) becomes comparable with thermal activation energy k_BT, where k_B is the Boltzmann constant. The anisotropy energy barrier is so small that thermal activation energy and/or an external magnetic field can easily move the magnetic moments from easy axis. Consequently the collective behaviour of the magnetic nanoparticle is same as that of paramagnetic atoms. Although the magnetic order still exists in the nanoparticles each particle behaves like a paramagnetic atom but with giant magnetic moment. Such behavior is known as superparamagnetism. This unique property of super paramagnetism makes magnetic nanoparticle a suitable material in several *in vivo* and in vitro applications such as drug delivery, hyperthermia, magnetic resonance imaging etc.[58,59]

Ease of surface functionalization

Nanomaterials show various interesting and unexpected properties due to the surface of the materials dominating the properties of the bulk materials. The percentage of atoms at the surface of a material becomes significant as the size of that material approaches to nanoregime. Due to high surface to volume ratio and large fraction of atoms present on the surface, the surface functionalization in case of nanomaterials is easy than their bulk counterparts. The ligand molecules attached to the nanoparticles surface prevent the aggregation of the nanoparticles and also control the growth of the nanoparticles. The surface of the nanoparticles can be functionalized by using some attractive interaction such as chemisorption, electrostatic attraction or hydrophobic interaction.

1.3. Nanomaterials used in medicine

Liposomes

Liposomes are phospholipids within the size range from 50-100 nm. These are amphiphilic in nature having bilayer membrane structure similar to that of biological membranes and an internal aqueous phase. Depending upon their size and number of layers liposomes are classified into three types such as multi-, oligo-, or unilamellar. Their amphiphilic nature enables liposomes to transport hydrophilic drugs entrapped within their aqueous interior and hydrophobic drugs dissolved in the membrane. Liposomes show excellent circulation, penetration and diffusion properties due to their physicochemical characteristics.[60] Moreover to increase the solubility of hydrophobic anticancer drugs, liposomal drug carriers have extensively studied from 1970s.[61,62] In 1995, a liposome-encapsulated doxorubicin formulation was the first liposome system permitted by the US Food and Drug Administration (FDA) for clinical human use and it was fully approved in 2005.[63] Till now the therapy using liposomal drug carriers has revealed potent activity against a broad range of human cancers. Even though liposomes have been succeeded in many clinical applications

but still its applications are limited due to poor storage stability, rapid clearance from the bloodstream, nonspecific uptake by the mononuclear phagocytic system and rapid drug release profiles in vivo.[64] Again the limited volume of the lipid bilayer makes the delivery of hydrophobic drug slightly inefficient.

Polymer micelles and nanoparticles

Polymer based drug delivery system was developed to reduce the inherent instability and degradation limitations related to liposomal drugcarrier[65]. Polymeric systems possess a series of superior activities as compared to liposomes and surfactant micelles. Those are 1) as pharmaceutical carrier shaving high drug loading capability, 2) prolonged circulation time stemming from higher stability in vivo, and 3) slower rates of dissociation that allow retention of loaded materials for a longer period of time[66-68]. In addition to this, polymeric drug carrier has ability to provide either controlled release or triggered release of the therapeuticmolecule.[69, 70] Among all polymers, amphiphilic polymers are of great importance because in selective solvents, amphiphilic diblock and triblock copolymers undergo self-associate to form micelles when the polymer concentration is at/above the critical micelle concentration (CMC). The self-assembly of amphiphiles in aqueous solution offers the formation of nanometer-sized particles with hydrophobic core/hydrophilic shell-type structures. The core regions serve as reservoirs for hydrophobic drugs, whereas the outer hydrophilic shell provides stability to the carrier in the physiological environment.[71-72] Depending upon the different synthetic condition, the drug can be chemically, electrostatically, or physically entrapped in situ during particle formation, or covalently bound to the polymer assemblies.

Dendrimers

Dendrimers are highly branched polymeric architecture shaving a central core, an internal region and numerous terminal groups that determine dendrimer

characteristics. Dendrimer shows versatility in drug delivery and high functionality whose properties resemble with biomolecules. Again these structures have ability to conjugate the high molecular weight hydrophilic/hydrophobic entities either by physical or chemical bonding. Moreover, chemical modifications by large number of surface terminal groups facilitate synthetic vector for drug and imaging diagnosis-agent.[73] The accurate control over the distribution of drugs is highly valuable to eliminate the typical drawbacks of traditional medicine. Hence the dendrimer based drug delivery system should be designed to target the definite site. In recent years, improved pharmacokinetics, biodistribution and controlled release of the drug to the specific targeted site has been achieved with polymer-baseddrugdelivery.[74] Due to their excellent water solubility,[75] biocompatibilty,[76] polyvalency[77] and precise molecular weight, dendrimers have received considerable attention in biological applications.[78] These features make them an ideal carrier for drug delivery and targeting applications.

Carbon nanotubes

Carbon nanotubes belong to the family of fullerenes and are formed of coaxial graphite sheets (<100 nm) rolled up into cylinders. These structures can be obtained either as single- (one graphite sheet) or multiwalled nanotubes (several concentric graphite sheets). Due to their small mass and size, Carbon nanotubes (CNTs) exhibits exciting structural, mechanical and electronic properties. These are mostly thermal stable and acting as good heat and electrical conductor. CNTs have been successfully applied in biomedical field due to their high surface area that is proficient of adsorbing or conjugating with an extensive variety of therapeutic and diagnostic agents (drugs, genes, vaccines, antibodies, biosensors, etc.). They have been first proven to be excellent vehicles for drug delivery directly into cells and keeping the drug intact without metabolism during transport in thebody.[79-82] Furthermore, CNTs have been extensively performed not only for drug and gene therapies but also for

tissue regeneration, biosensor diagnosis, enantiomer separation of chiral drugs, extraction and analysis of drugs and pollutants.

Quantum dots

Quantum dots are colloidal fluorescent semiconductor nanocrystals (2–10 nm). The central core of quantum dots consists of combinations of elements from groups II–VI of the periodic system (CdSe, CdTe, CdS, PbSe, ZnS and ZnSe) or III–V (GaAs, GaN, In Pand InAs), which are 'over coated' with a layer of ZnS. Quantum dots are photostable. They show size- and composition-tuneable emission spectra and high quantum yield. They are resistant to photobleaching and show exceptional resistance to photo and chemical degradation. All these characteristics make quantum dots excellent contrast agents for imaging and labels for bioassays.[83]

Gold nanoparticles

Gold nanoparticles are metallic nanoparticles having size less than 50 nm. They can be prepared with different geometries, such as nanospheres, nanoshells, nanorods or nanocages. They are mostly inert in the biological environment and shows a number of suitable physical properties for several biomedical applications such as hyperthermia for tumor destruction or radiotherapy for cancer, photodynamic therapy, computed tomography imaging and as drug carriers to tumors.[84] Gold nanoparticles are excellent labels for biosensors because they can be detected by numerous techniques, such optic absorption, fluorescence and electric conductivity.[85] Current advances in synthetic chemistry makes accessible for the preparation of gold nanoparticles with excellent physicochemical and optical properties, which are necessary for specific clinical or biological applications. Due to numerous method available for the surface modification of gold nanoparticles for conjugating different ligands, drug molecules and targeting moieties, AuNPs can be used in broad range of applications. AuNPs are biologically inert and shows much less toxicity but it shows

relatively low rate of clearance from circulation and tissues can lead to serious health problems, hence specific targeting of diseased cells and tissues must be achieved before AuNPs use for biological applications.

Magnetic nanoparticles

Recently, the synthesis of superparamagnetic nanoparticles has been intensively developed due to their wide applications in magnetic resonance imaging (MRI),[86] virus detection,[87] magnetic cell separation,[88]enzyme catalysis, targeting chemotherapy,[89] and radiotherapy.[90] More specifically Superparamagnetic iron oxide nanoparticles with appropriate surface chemistry can be used for numerous *in* vivo applications, such as MRI contrast enhancement, tissue repair, immunoassay, detoxification of biological fluids hyperthermia, drug delivery, and cell separation. All of these biomedical applications require that the nanoparticles have high magnetization values, a size smaller than 100 nm, and a narrow particle size distribution. These applications also need appropriate surface coating of the magnetic particles, which has to be nontoxic and biocompatible and must also allow for a targetable delivery with particle localization in a specific area. The surface of magnetic nanoparticles need to be coated to avoid the formation of aggregates and offer different functional groups (amines or carboxylic acid) for bioconjugation to anticancer drugs and/or targeted ligands. Large number of surface coating have been used including lipids,[91-92] liposomes,[93-94] proteins, [95-97] polymers,[98-100] and dextran.[101] Furthermore, magnetic nanoparticles are widely used in hyperthermia treatment to destroy cancer cells. When an external alternating magnetic field (AMF) applied to the magnetic nanoparticles (MNP), it produced energy in the form of heat in radio frequency region. Such an effect can be exploited to use MNPs as mediators in magnetic hyperthermia.

Although nanoparticles have lots of advantages because of the unique properties they have, there are many clinical, toxicological and regulatory aspects

which are the matters of concern too. The comparison of performances of different drug conjugated nanoparticles has been provided in table 1.1. The biocompatibility of nanomaterials is of utmost importance because of the effect of the nanomaterials in the body ranging from cytotoxicity to hypersensitivity. Certain nanomaterials have been associated with oxidative stress,[102,103] undesirable inflammatory responses, and genotoxicity. Critical evaluation is necessary of whether benefit outweighs the adverse effect. It is quite essential to introduce cost effective, better and safer nanobiomaterials.

Table 1.1

Type of NP	Drug	IC_{50} for drug (in µg/mL)	IC_{50} for drug conjugated NP (in µg/mL)	Cancer cell line	Reference
DOX-HA-SPION	Doxorubicin	17.5	4.37	NCI/ADR-RES	104
HA-CNT-DOX	Doxorubicin	2.117	0.868	A549	105
FA-CNT-DOX	Doxorubicin	0.316	0.186	HeLa	106
Pt-DNA-Au	Cisplatin	11	0.9	HeLa	107
Cap-CDDP	Cisplatin	1.7	3.2	HeLa	108
MTX-CS-NPS	Methotrexate	0.0098±0.05	0.0098±0.012	HeLa	109
Platin-Au-Fe_3O_4-Herceptin	Cisplatin	3.5	1.76	HeLa	110
C-dots@GNR@DOX	Doxorubicin	153.3	78.2	HeLa	111

1.4. Multifunctional nanoparticles

The dimension of nanoparticles is in the same range as antibodies, membrane receptors, nucleic acids and proteins. These biomimetic features, together with their high surface to volume ratio and the possibility of modulating their properties, make nanoparticles powerful tools for imaging, diagnosis and therapy.[104-105] Thus, nanoparticles offer significant improvements in performance compared with existing technologies. As we know that nanoparticles used as a powerful tool in

nanomedicine, still some application remain challenging, such as *in vivo* real-time monitoring of cellular events, specific targeting to the action site or efficient drug delivery inside the target cell. In this circumstance, to surmount this difficulty, the design of multifunctional nanoparticles would be essential.

Multifunctional nanoparticles could significantly improve already existing nanoparticle characteristics. It combines different functionalities in a single platform. For example, a core particle could be linked to a specific targeting function that recognizes the unique surfacing natures of their target cells. Simultaneously, the same particle can be modified with an imaging agent to monitor the drug transport process, a function to evaluate the therapeutic efficacy of a drug. Whereas mono functional nanoparticles provide a single function, e.g. a liposome can transport drugs but does not have the inherent property to distinguish between healthy and unhealthy cells or tissues. Combination of diverse range of functionalities into a single core require different steps, such as the deposition of metal layers onto a supporting nanoparticle core, modifying the biocompatible linked to stabilize the nanoparticles etc.[106-108]

Furthermore, these different properties of multifunctional nanoparticles have to be coordinated so that they operate in an organized way and indeed provide the desired functionalities (Fig. 1.1). Early efforts toward multifunctional nanoparticles for integrated drug delivery and imaging focused on combining polymeric drug carriers with organic fluorescent dyes for particle visualization. Fluorescent drug particles were prepared by binding water-soluble fluorophores to the surfaces of preformed polymer nanoparticles or by chemically tethering fluorescent dye to the hydrophobic terminus of an amphiphilic block copolymer and then permitting the polymer to selfassemble.[109-110] Organic dyes and fluorophores, however, require direct visualization and so are generally practical only for *in vitro* applications.[111] Particles having a metallic core that adds contrast to images acquired by MRI or CT, for example, are more suitable for *in vivo* biomedical applications.[112-113] However, as synthesized, inorganic nanoparticles are incompatible with biological environments.

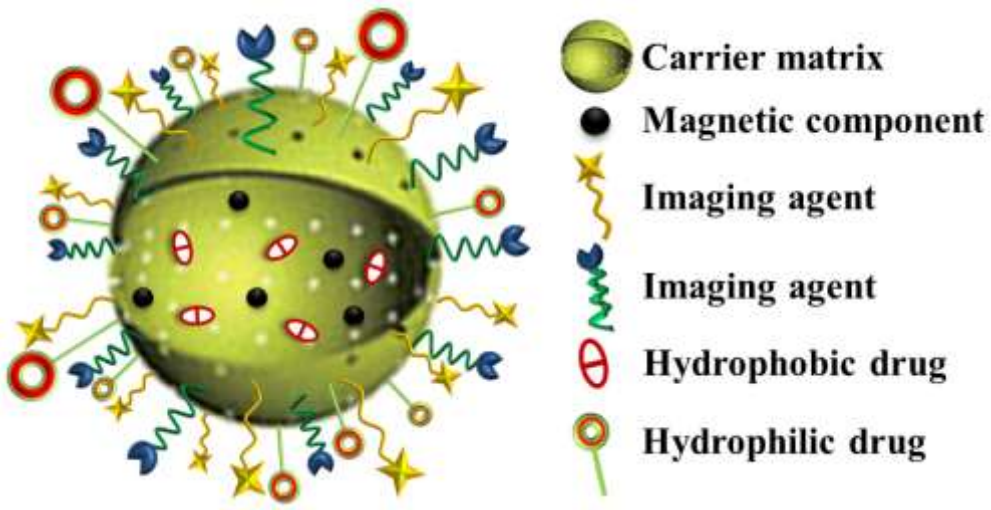

Fig. 1.1 Schematic representation of multifunctional nanoparticle for drug delivery and theranostic application.

Owing to surface hydrophobicity or toxicity limitations. Consequently, several coating strategies have been developed to enhance their biocompatibility, improve their aqueous stability and provide chemical handles for further reactions with biomolecules.[114] Modification methods have included the adsorption of small-molecule ligands or stabilizers on the colloid surfaces,[115] layer-by-layer deposition of polyelectrolyte chains,[116] surface initiated polymerization of high-density polymer brushes,[117] or block copolymer deposition on colloid surfaces.[118] By extension, ligands (optionally together with drugs) can be covalently attached to the coating material.[119-120] For example, multifunctional super paramagnetic nanoparticles bearing covalently-bound drugs and targeting ligands have been reported for selective drug delivery to regional lymph nodes and for imaging of prostate cancers .[121]

The major applications of multifunctional nanoparticles in the biomedical field can mainly divided into imaging and therapy.

Multimodal imaging

Nowadays, Most of the imaging techniques such as MRI, PET and CT are vital in the diagnosis of various diseases. Each modality has its own merits and disadvantages, and also a single imaging technique does not possess all the required capabilities for complete imaging. Thus, multimodal imaging methods are quickly becoming important tools in the field of biomedical research. Multimodal contrast agents could help in improving the diagnosis and treatment of diseases in their earliest stages by providing far more inclusive data to clinicians.

Most commonly, magnetic nanoparticles act as a core platform for the addition of other functional imaging moieties. For example, MRI-optical dual-mode probes composed of a fluorescent dye-doped silica core surrounded by magnetic nanoparticles can macroscopically detect neuroblastoma cancer cells using MRI along with subcellular information through fluorescence imaging.[122] Magnetic nanoparticles can also be coupled with radionuclides to construct MRI-PET dual modal probes.[123] Such probes can accurately detect cancerous cells in lymph nodes, which are critical for assessing cancer metastasis. Systems using magnetic nanoparticles modified with fluorescent probes and biomolecules can also monitor gene expression and other markers in therapeutic cell studies. Each component of such multimodal probes complements the other modalities, and their synergistic materials properties can ultimately provide more accurate information both *in vitro* and *in vivo*.[124]

Magnetic Resonance Imaging (MRI)

Magnetic resonance imaging is a powerful tool for the diagnosis of disease and the study of biological processes such as cancer metastasis and inflammation. Super paramagnetic iron oxide nanoparticles, in particular, are effective contrast agents that provide high sensitivity in MRI.[125-126] First introduced in the mid-1980s,

they are typically composed of iron oxide based cores (magnetite, maghemite, or other insoluble ferrites) in the size range 5 – 10 nm coated with water-soluble stabilizing layers. In the presence of a magnetic field, these magnetic domains possess large magnetic moments that produce localized disturbances in magnetic field homogeneity. Owing to these magnetic disturbances, there exists a large susceptibility difference between the iron oxide crystals and nearby protons, which causes rapid dephasing of spins and a resultant decrease in transverse and translational relaxation times. The shortening of the transverse relaxation time, specifically, results in a darkening of the image relative to unaffected areas, corresponding to a 'negative' contrast enhancement. Compared with micrometer-sized magnetic particles and chelates of paramagnetic ions such as gadolinium diethylenetriaminopentaacetic acid (Gd-DTPA), super paramagnetic iron oxide nanoparticles are much more efficient as relaxation promoters, and their effect on the relativities of water is measurable even at nanomolar concentrations.[127] Commercial examples of super paramagnetic MRI contrast agents include Lumiren, silicon-coated iron oxide particles with a diameter of ~300 nm, Endorem and Ferixex I.V, liver-specific, dextran coated iron oxide particles of ~ 150 nm diameter, and Sinerm, a blood pool contrast agent.

Targeted drug delivery

Targeted drug delivery is a method of delivering medication at the desired target in therapeutic concentration at the same time restricting its access to normal cellular lining. Insufficient target selectivity of drugs can cause unwanted side effects and reduce therapeutic efficacy. Thus the targeted or site-specific delivery of drugs is very attractive goal because this provides one of the most potential ways to improve the therapeutic index of the drugs with minimal peripheral toxicity. Passive targeting through the well-studied enhanced permeability and retention (EPR) effect is not universal for all types of tumor cells, and a lack of cell specific interactions might decrease therapeutic efficacy and induce multiple drug resistance.[128] In contrast,

active targeting through covalent attachment of targeting molecules such as folic acid,[129] hyaluronic acid,[130] aptamer,[131] antibody,[132] etc. to the nanoparticle surface could promote the site-specific delivery of therapeutics. Yang and coworkers studied the use of multifunctional nanoparticles for simultaneous in vivo imaging and delivery of therapeutic products for cancer treatment.[133] These authors developed a multifunctional nanosystem combining magnetic nanocrystals (for MRI), with therapeutic antibodies (for specific delivery) and the chemotherapeutic drug doxorubicin (for synergistic therapy). In a similar approach, Farokhzad and coworkers developed biocompatible nanoparticles for the specific delivery of docetaxel to localised tumors. Targeted delivery was achieved on this occasion using aptamers that recognized a prostate specific membrane antigen.[134] The chemotherapeutic drug is stored and protected in the nanocarrier until it reaches the tumor site. The drug is thus harmless to healthy tissues during its circulation in the body and provided in high concentrations at the desired location.

Hyperthermia

Hyperthermia is a type of medical treatment in which the body tissue is exposed to slightly higher temperature to damage cancer to damage and kill cancer cells or to make cancer cell more sensitive to the effect of radiation and certain anticancer drugs. This technique can be controlled carefully because at high temperature they can also injure or kill normal cells and tissues. Hence the use of hyperthermia treatment for cancer is a real challenge, as it was hard to maintain the right temperature in the right area while limiting the effects on other parts of the body. A wide range of heat sources and treatments for hyperthermia are being developed for clinical applications. There are three main types of hyperthermia: local hyperthermia, regional hyperthermia and whole-body hyperthermia. The hyperthermia technique is chosen depending on the location, the depth and the stage of malignancy. In whole-body hyperthermia, the entire body is heated up. This

method is preferred in the case deep-seated and propagated metastases. The heating can be achieved through hot water baths, thermal chambers or infrared radiators. Local hyperthermia is selected used to treat localized tumors either superficially or inaccessible body cavities. It is the less invasive technique. Local hyperthermia systems are based on applicators or antennas emitting mostly microwaves, ultrasounds or radio waves. Recently, a new technology has been developed for local hyperthermia using MNPs as mediators of heat. This technique is called Magnetic Fluid Hyperthermia (MFH). MFH consists of a colloidal suspension of MNPs that is injected into the tumor where the MNPs will be internalized by the cancer cells.[135] Applying an external alternative magnetic field (AMF) will cause the NPs to heat and kill the cancer cells because when a magnetic nanoparticle is placed inside an alternating magnetic field, it will spin back and forth generating significant heat in the radio frequency region.

The first clinical trial was conducted in 2003 on 14 patients' suffering from glioblastoma multiform.[136] The promising results lead to a phase II study involving 66 patients with glioblastoma multiform. Results showed that hyperthermia therapy using MNPs can be applied safely and is effective for the treatment of cancer, but also that the overall survival following diagnosis of first tumor recurrence is longer compared to conventional therapies.[137] MFH possesses numerous advantages over traditional techniques. First of all, the injection of MNPs is less invasive and can be potentially injected and concentrated anywhere in the body, allowing the treatment of all kinds of tumors with limited side effects. Moreover, once the MNPs have been internalized by the cancer cells, they can remain inside the cells even after creation of daughter cells.[138] In fact, 50% of the amount of MNPs present in parent cells end up in the daughter cells, meaning that a subsequent hyper thermic treatment can be applied without large reinjection of MNPs. Magnetic targeting can be used to drive the MNPs toward the targeted cancer regions. The MNPs can also be functionalized with a recognition moiety (i.e. antibodies, proteins) to increase the selectivity to

malignant cells, therefore increasing the internalization of the MNPs in the cancer cells.[139] The potential of MFH as a treatment for cancer is clear, but can even be improved by designing MNPs with multiple therapeutic functions, i.e. hyperthermia and drug delivery. Indeed, drug delivery utilizing NPs also has numerous advantages over traditional chemotherapy. The major drawback of chemotherapy being the non-specificity of the drugs, healthy organs and cells may also be strongly damaged during the therapy. With NPs, the possibility of targeting specific locations in the body allows the reduction of the chemotherapeutic dose to reach the concentrations needed in the tumors for an effective therapy. Besides, the concentration of drugs at non-targeted sites is reduced therefore minimizing undesirable side effects.[140] Taking advantage of the synergistic effect of the combined thermo-chemotherapy, MNP-based therapeutic agents for hyperthermia and controlled drug delivery are promising candidates in the treatment of cancer.

1.5. Major challenges in designing multifunctional nanoparticles

Control design of multifunctional nanodevice is an active area of research. Due to their enormous application in various disciplines such as potential applications in responsive sensors and acting as nanovehicles with targeting capabilities carrying drugs, DNA, imaging agents, etc.[141-147] Now accumulating multiple functionalities onto the surface of pre-existing nanoparticles is a challenging task because this process involves chronological chemical processing of nanoparticles. At first drug encapsulated nanoparticles are formed, followed by surface modification with different ligands to provide other functionalities such as targeting, responsiveness to stimuli, etc.[148] Due to this sequential conjugation/modification, there is a chance of the potential loss of one or more existing functionality (imparted in previous steps) due to the chemical processing steps involved in adding a new functionality. Hence it is a real challenge, to choose such a core nanoparticles that can be easily scale-up and reproduce their surface properties with well-defined characteristics.

Choosing an appropriate magnetic component

For pharmaceutical and biomedical purposes (Fig. 1.2), magnetic platforms should possess very small size and narrow size distribution together with high magnetization

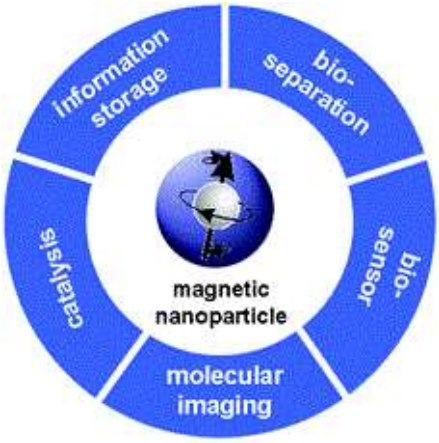

Fig. 1.2 Various applications of magnetic nanoparticles in designing multifunctional nanoparticles.

values. Additionally, these nanoparticles (NPs) must combine high magnetic susceptibility for an optimum magnetic enrichment and loss of magnetization. Size and shape are the key features that govern the physical properties. For instance, magnetization measurements have demonstrated that the saturation magnetization of iron oxide particles decreased with a decrease in size.[149] The importance of choosing an appropriate magnetic component in designing multifunctional NPs as it serves as a targeting agent under external magnetic field, hyperthermia therapy and magnetic resonance imaging. The size strongly influences the magnetic moment of the particles and their subsequent response to the magnetic fields. However, MNPs at the very low size range can exhibit superparamagnetism, which determines greater magnetization capabilities compared to paramagnetic materials. Interestingly, particle size has also been described to control the signal (i.e., transverse relaxation T2/T1) in MRI of iron oxides which can have consequences concerning the quality of the diagnosis.[150,151]

Choosing an appropriate ligand

An appropriate ligand contributes selectivity to the multifunctional NPs for targeting various cancer cell lines. Active targeting is one of great benefit for the application of magnetic nanoparticles in the diagnosis and treatment of cancer, in which magnetic nanoparticles are further functionalized with a suitable targeting ligand that possess a high affinity towards the receptor present on the surface of cancer cell. The key factor here is that expression levels of receptors in the cancer cell is 100–300 times higher than those observed in healthy tissues. Recently broad range of ligands has been used for targeted nanocarrier and belongs to the families of small molecules, carbohydrates, peptides, proteins or antibodies. Monoclonal antibodies (mAbs) were first used targeting agent for the accurate delivery of magnetic nanoparticles. [152-153] Up to the present day, It was recognized as one of the most very well-liked targeting molecules, due to their exceptionally high affinity towards tumor

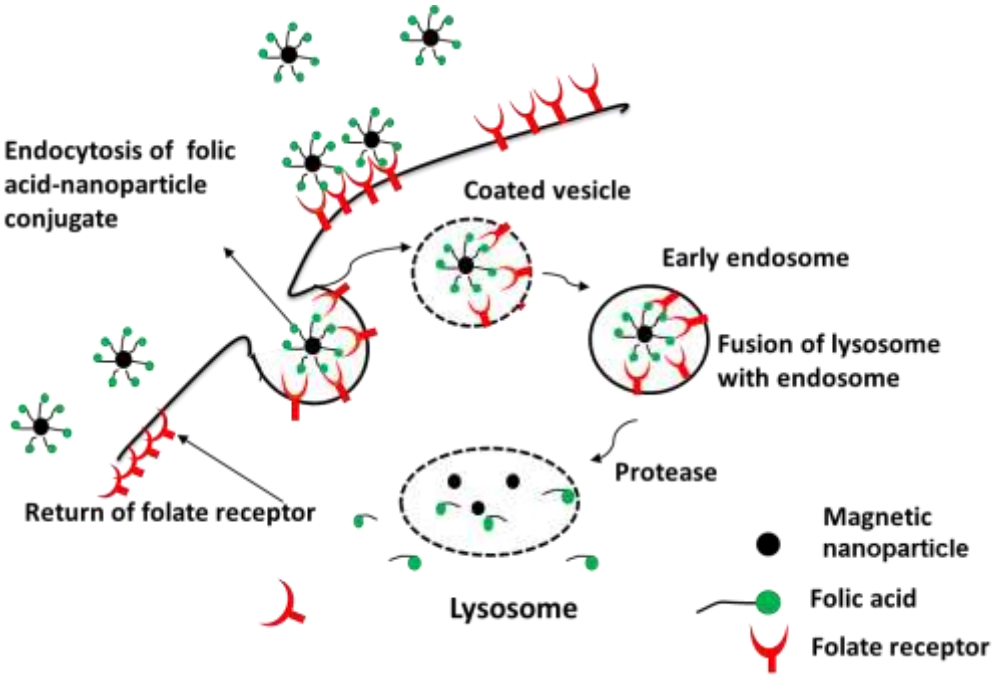

Fig. 1.3 Mechanism for folate receptor mediated endocytosis pathway.

cell. However, major drawbacks of this ligand are their comparatively large size and inherent immunogenicity, which hinders a sufficient circulation and diffusion through biologicalbarriers.[154] Thus, most encouraging ligand molecule that is used for targeted therapy should be small in size, readily available, inexpensive, easy to handle, to be chemically modified and to be characterized. Another popular technique developed to conjugate small molecule for the targeted specific delivery. Folic acid is the most investigated targeting ligand in this respect because this vitamin can be found on the surface of various human cancer cell, such as breast, ovarian, lung, renal, and colon cancer.[155] Beside this, folic acid conjugated magnetic nanoparticles have been used not only to improve the MRI detectability of various tumors in vivo but also this conjugated system helps to destroy cancer cells via hyperthermia treatment (Fig. 1.3).[156-158] Advantages of conjugating small targeting molecule on the surface of nanoparticle are to diminish the risk of bond breaking and loss of functionality inside the body.

Theranostic magnetic nanoparticles

Magnetic nanoparticles (MNPs) possess unique magnetic properties and the ability to function at the cellular and molecular level of biological interactions making them an attractive platform as contrast agents for magnetic resonance imaging (MRI) and as carriers for drug delivery.[159] Recent advances in nanotechnology have improved the specific delivery of therapeutic agents by attaching a targeting agent and fluorophores to MNPs. These multifunctional magnetic nanoparticles are called "theranostic agents". The term "theranostic" signifies the development of specific therapies for various diseases with simultaneous diagnostic capabilities. Such particles have higher magnetic moments, high surface area-to-volume ratios allowing for a large number of therapeutic molecules can be attached to individual nanoparticles. Additionally, while utilizing an active targeting strategy for specific delivery, the magnetic properties of the nanoparticle may be used to provide imaging

modality for monitoring drug delivery through MRI,[160] or an alternative source of treatment through magnetic fluid hyperthermia (MFH) therapy.[161] Also multifunctional MNPs functionalized with different biomolecules have loaded with a various anticancer agent such as carboplatin, doxorubicin, paclitaxel,[162] 5-fluorouracil,[163]epirubicin,[164]etc directed towards tumor sites by applying an external magnetic field. For these applications, the size, surface chemistry, and charge are particularly important to ensure that the nanoparticles can stay for a long time in circulation. However it was reported that MNPs having size between 50-100 nm are smaller than the spleen cut off (200 nm) can easily penetrate into large tumors following systemic administration.[165] Gong et al. have designed multifunctional MNPs nanocarriers for both tumors targeted drug delivery and PET/MR imaging of tumors. The anticancer drug DOX conjugated to the PEGylated MNPs nanocarriers through pH sensitive bonds.[166] Chitosan-DOPA-stabilized-ferrimagnetic iron oxide nanocubes have developed by Hyeon et al. to provide an effective heat nanomediator for cancer hyperthermia. They facilitate successful suppression of cancer cells through caspase-mediated apoptosis These nanocomposites also show excellent antitumor efficacy in an animal tumor model without showing severe toxicity.[167] Chen et al. developed a magnetic drug delivery system in which doxorubicin (DOX) was chemically bonded to Fe_3O_4 nanoparticles and successfully deliver to the cancer cell.[168]

Although magnetic nanoparticle-based drug delivery system is very much popular strategy for chemotherapy, hyperthermia and imaging applications, still it has some demerits such as less stable in physiological environment and nonspecific interaction with blood components that bring the side effects of opsonization, aggregation of red blood cells and platelet activation.[169] Therefore more and more studies focused on the surface modification of MNPs with different inorganic coatings to prepare a stable inorganic magnetic composite nanoparticles, such as silica, gold, hydroxyapatite, and graphene, which can not only deliver drugs through

the adsorption of drugs on the surface of the nanoparticles, but also make the nanoparticles stable and biocompatible and thereby useful for hyperthermia.[170-173] The recent progress on the development of such inorganic coating materials concerning their medical application has been briefly reviewed in the following few points.

Mesoporous nanoparticles (MSN) have been considered as promising candidate carriers for drug/gene delivery due to their high surface area, large pore volume and ease of surface functionalization. Furthermore, encapsulation of MNPs in a mesoporous silica matrix enhances the chemical stability of MNPs and avoids the potential toxic effects of MNPs on cells. Qiao and coworkers synthesized monodisperse yolk–shell magnetic nanoparticles with a porous hierarchical structure, and these magnetic nanoparticles exhibited enhanced drug loading capacity and drug release behavior.[174] Sanchez and coworkers reported the fabrication of mesoporous maghemite-organosilica microspheres by the spray-drying process, and for the first time proposed mesoporous magnetic microspheres as multifunctional platforms for MR imaging and hyperthermia therapy.[175] Vallet-Regí and coworkers reported the aerosol assisted synthesis of magnetic microspheres composed of γ-Fe_2O_3 nanoparticles embedded in a mesoporous silica matrix, and these magnetic microspheres showed the abilities to load and release therapeutic drugs and to conduct magnetic hyperthermia upon exposure to a low frequency alternating magnetic field.[176] Lu et al. synthesized magnetic iron oxide loaded hollow mesoporous silica nanocapsules using polymer nanospheres as sacrificial templates, and found that these magnetic nanocapsules with a particle size of 100 nm showed magnetic field induced heating and remotely triggered drug release capabilities, and thereby provide a platform for the combination of hyperthermia and chemotherapy.[177]

Amorphous calcium phosphate or hydroxyapatite widely used in biomedical applications since it has excellent biocompatibility due to its chemical similarity to human hard tissue (bone and teeth). In recent years, calcium phosphate/hydrophilic block copolymer based drug delivery systems have attracted considerable attention

because they not only possess the properties of inorganic-organic ingredients but also the porous structure facilitates the incorporation of a high dosage of drug, which significantly enhances bio-performance.[178] Fabrication of MNPs with calcium phosphate can be developed as a suitable multifunctional nanodevice for nanotherapeutics approaches, and used for magnetic targeting drug delivery and Magnetic resonance imaging. Zhou et al. fabricated a magnetic calcium phosphate nanoformulation by the bio mineralization of calcium phosphate on the surface of magnetic nanoparticles with abundant amino groups, and thus the inorganic layer of calcium phosphate can improve the biocompatibility and simultaneously the magnetic iron oxide can maintain the magnetic targeting function for the delivery of anticancer drug doxorubicin hydrochloride and DNA.[179] Liu et al. developed a novel remotely triggered drug vehicle i.e. HAP-coated liposome decorated with super paramagnetic iron oxide nanoparticles that exhibit ultrasound triggered drug release behaviour, magnetic resonance imaging contrast and ultrasound-induced MRI contrast change.[180]

Very recently carbon coating on the surface of MNPs has been used as the biocompatible material. One of the advantages of using carbon is its high capacity of adsorption and their chemical as well as mechanical stability. The incorporation of materials into their inner hollow space is convenient, whereas the outside wall can be chemically modified according to the desired purpose. In 2010, Oh et al. have explored magnetic carbon nanoparticles with a mesoporous structure, monodispersity, magnetism, and biocompatibility as a drug carrier.[181] Schreiber et al. have reported that carbon magnetic nanoparticles may support efficient immunization protocols or diagnostic assays to target, track, and manipulate dendritic cells.[182]

1.6. Cobalt ferrite nanoparticles used as suitable magnetic component

Super paramagnetic Iron oxide nanoparticles (SPION) have been a subject of interest in recent years due to their promising technological applications, especially in

biomedicine. However, cobalt ferrite nanoparticles can also be explored as a suitable candidate in the world of nanomedicine due to its extraordinary physical and mechanical properties. One of the most important reasons for using cobalt ferrite nanoparticles in the biomedical application is its high magneto crystalline anisotropy that originates from the spin–orbit (L–S) coupling at crystal lattices. In addition to this, the surface of this material is hard with a high Curie temperature T_C (520 °C), high coercivity of about 4.3 kOe at room temperature for the 40 nm size single domain, moderate saturation magnetization of about 80 emu/g for bulk at room temperature, high anisotropy constant ($2.65\times106 - 5.1\times106$ erg cm^{-3}) and high magnetostrictive (-225×10^{-6}).[183] Moreover, the cobalt ferrite nanoparticles show excellent chemical stability, mechanical hardness, wear resistance, ease of synthesis, and electrical insulation. Hence, due to the above-mentioned properties cobalt ferrite nanoparticles would be one of the most promising candidates for medical applications including magnetic drug delivery, radio-frequency hyperthermia, magnetic resonance imaging (MRI) and medical diagnostics.[184-187] Rittich et al.[188]used cobalt ferrite for the isolation of deoxyribonucleic acid (DNA). Lee *et al* reported the use of cobalt ferrite nanoparticles as contrast enhancing agent in magnetic resonance imaging (MRI). They investigated the use of cobalt ferrite nanoparticles for hyperthermia treatment due to the self-heating characteristics of cobalt ferrite nanoparticles.[189] Christopher *et al* observed that the heat is generating from aqueous dispersed $CoFe_2O_4$ nanoparticles and hence they used cobalt ferrite nanoparticles as a heat generating agent for magnetically activated drug delivery and hyperthermia.[190]

Superparamagnetic nature of magnetic nanoparticles has been determined from magnetocrystalline anisotropy. This magnetocrystalline anisotropy nature of magnetic particles is originating from the spin- orbital (L-S) coupling at crystal lattices. For a cubic spinel structure of a crystal, the relative magnitude of magnetic anisotropy can be determined from the significant difference in L-S coupling strength between the cations. Among different spinel ferrites, Co-ferrite has the highest value

of the S–L coupling and anisotropy constant [K_1 ($\times 10^5$) ($MnFe_2O_4$) = − 0.25 (erg cm^{-3}), K_1 ($\times 10^5$) (Fe_3O_4) = −1.2 (erg cm^{-3}), and K_1($\times 10^5$) ($CoFe_2O_4$) = +19, +30 (erg cm^{-3})].[191] Co^{2+} cation with $3d^7$ electronic configuration at a B site in $CoFe_2O_4$ has a triplet $^4T_{1g}$ ground state. Even though the trigonal field is introduced with the T_{1g} ground state further splitting into A_2 and E states, the Co^{2+} cation with a degenerated ground state of E is still considered to have a strong L–S coupling and consequently contributes greatly to the magnetic anisotropy of $CoFe_2O_4$.[192]

Highly dispersed cobalt ferrite nanoparticles generate efficient and controlled heat for hyperthermia application. Furthermore the small size, high magnetic crystalline anisotropy and moderate saturation magnetization are also suitable for hyperthermia treatment. The amount of heat generating from magnetic nanoparticles depends upon the magnetic moment, field, frequency, and particle volume because power loss describes the heat generation due to Brownian and Neel relaxation mechanisms. The power loss equation can be expressed as [P = μ0 πf x″H2] where P is the heat generation of nanoparticles, x″ is the susceptibility, H is the amplitude of the magnetic field intensity, and $\mu 0 = 4\pi \times 10^{-7}$ $(T\ mA)^{-1}$.[193,194]

It is obvious that the desired heat to achieve the magneto thermally triggered drug delivery and hyperthermia can be reached using cobalt ferrite nanoparticles by adjusting the magnetic field and frequency.[195] Magnetic cobalt ferrite nanoparticles were found to resonantly respond to a time-varying magnetic field with advantageous results related to the transfer of energy from the exciting field to nanoparticles. Besides to this hyperthermia treatment varies with an important parameter i.e., the specific absorption rate (SAR).

$$SAR = C\frac{\Delta T}{\Delta t}\frac{1}{m_{ferrite}}$$

Where, C is the specific heat of the ferrofluid and sample holder taken together, $\Delta T/\Delta t$ is the initial slope of the time-dependent temperature curve; m ferrite is the total ferrite content in the fluid.[196] It is experimentally found that SAR value is at the highest level for cobalt ferrite (~396 W/gFe) than $MnFe_2O_4$ (136 W/gFe), and Fe_3O_4 (168 W/gFe), making cobalt ferrite more appropriate for hyperthermia. In addition to this, cobalt ferrite offers excellent r_2 relaxivity (transverse) in MRI. Higher the value of saturation magnetization higher r_2 relaxivity is observed. The r_2/r_1 values for $MnFe_2O_4$, Fe_3O_4 and $CoFe_2O_4$ are 12.2, 23.1 and 62.3 respectively.

1.7. Current state-of-the-art

The major design concept of current theranostic nanomaterials takes into account all three components, i.e., imaging agent, therapeutic agent, and targeting moiety. All three components have been under extensive investigation for development of tailored theranostic applications. It is now common practice to combine two imaging modalities for multimodal imaging. Nanoparticles have been particularly developed for optical imaging and MRI. In the field of MRI, several superparamagnetic iron oxide based nanoparticles such as Feridex, Resovist, Lumiren have been clinically approved. However, there remains ample scope to explore other ferrites (MFe_2O_4) where M = Ni, Zn or Mn for their potential applications in MRI. It would be advantageous to explore the contrast enhancing properties of other ferrite nanoparticle for magnetic resonance imaging and therapy. Great innovations can be introduced in terms therapy and imaging by making hybrid carrier matrices such as core-shell, hollow structures with ample guest loading capacity, mesoporous hollow structures to integrate more than one probe for imaging. The conjugation of the payloads to the nanocarrier requires suitable intermolecular interaction such as π-π stacking interaction, hydrogen bonding, and covalent bond formation between the carrier and the payload molecules. In particular, the release kinetics of the drug either conjugated to the carrier or entrapped in the carrier would be significantly different

from those of conventionally administered systemic drugs which might lead to significant difference in therapeutic efficacy. In addition to this, protection of therapeutic drugs and imaging agents is of paramount importance in order to minimise the side effects of premature drug release. Among the nanotheranostics developed for various cancer chemotherapeutic drugs, doxorubicin (DOX) is the most explored. Research efforts are desirable to accommodate some challenging therapeutic moieties in the theranostic nanogent for which there is no other suitable delivery system available till now. Another important requirement is that targeting theranostic agent to specific site. Robust chemical conjugation strategies must be adopted to attach cancer directing agents such as folic acid. Judicious control on number of marker molecules and therapeutic as well diagnostic moieties would be advantageous to obtain optimum efficacy of the theranostic multifunctional nanoparticle.

The overall goal of this research work is to develop fluorescent magnetic nanoparticle for target specific delivery of some potential anticancer drugs, like cisplatin, methotrexate, pemetrexed etc., monitoring drug activity *in vitro* by fluorescence imaging and exploring the possibilities of our material in MRI. To realize our goal we focus on four important issues. 1) Overall structure, morphology and stability of the carrier matrix; 2) Adopting low cost materials to design the carrier; 3) Suitable conjugation strategy to attach therapeutic agent and marker molecule which ensures long term stability and stimuli responsive controlled release of the therapeutic agent; 4) Overall integrity of the theranostic agent with reasonable hydrodynamic size and all functional properties intact till it reaches the target site. We hypothesize that because of the merits of cobalt ferrite nanoparticle as discussed in section 1.6, if it is used instead of iron oxide the transverse relaxivity (r_2) of the theranostic agent would be improved and hence more negative contrast would be generated in MRI. Hollow spheres may be employed as a single carrier to encapsulate sparingly water soluble anticancer drugs, hydrophilic anticancer drugs and imaging

agents to achieve combinational therapy and imaging simultaneously. A fluorescent inorganic matrix can be used as a carrier in the theranostic system to avoid additional fluorophore conjugation. In this connection fluorescent carbon may be explored due to its inertness, high fluorescence quantum yield and excitation dependent luminescence.

1.8. Objectives

Our current research is focused on the development of suitable synthetic methodology or improvement of existing technologies for large scale production of multifunctional magnetic nanoparticles based formulations for some widely acceptable anticancer drugs. Our research objective is set as follows:

- To develop an easy, eco-friendly and cost-effective synthetic technique for large scale production of functionalized porous metal ferrites
- To explore the suitability of cobalt ferrite nanoparticles as a magnetic component in multifunctional theranostic nanoparticle
- To design a robust matrix to carry cargoes such as ferrite nanoparticle and cancer drugs and to regulate their stimuli responsive release mechanism while keeping their therapeutic activity intact.
- To explore the luminescence properties of carbon nanostructures in theranostic application
- To investigate the suitability of the developed theranostic nanoparticles as a T_2 contrast agent in MRI
- To evaluate the performances of the synthesized drug loaded particles *in vitro* in some model cancer cells

In line with this approach a mesoporous cobalt ferrite based drug carrier has been designed for the targeted delivery of leading anticancer drugs doxorubicin as well as methotrexate. Magnetic hydroxyl apatite nanoparticles have been developed

for the delivery of cisplatin. Mesoporous hollow silica and carbon based theranostic agents have been developed for anticancer drugs pemetrexed, cisplatin and doxorubicin. The therapeutic and diagnostic performances have been evaluated *in vitro*. The detail of the material design and added advantages of each system have been discussed in subsequent chapters.

1.9. References

1. J. E. Lee, N. Lee, T. Kim, J. Kim, T. Hyeon, Acc. Chem. Res., 2011, 44, 893.
2. G. Chen, H. Qiu, P.N. Prasad and X. Chen, *Chem. Rev.*, 2014, **114**, 5161.
3. E. K. Lim, T. Kim, S. Parik, S. Hamm, Y. M. Hab and K. Lee *Chem. Rev.*, 2015, **115**, 327.
4. E. Peng, F. wang and J. M. Xue, *J. Mater. Chem. B.*, 2015, 3, 22412276.
5. G. Visani and F. Loscocco, *Nanomedicine.*, 2014, **15**, 2415.
6. Y. Cheng, R. A. Morshed, B. Auffinger, A. L. Tobias, M. S. Lesniak, *Adv. Drug Deliver. Rev.*, 2014, **66**, 42.
7. J. Lu, W. Zhao, Y. Huang, H. Liu, R. Marquez, R. B. Gibbs, J. Li, R. Venkataramanan, L. Xu, S. Li, S. Li, *Mol. Pharmaceutics*, 2014, 11, 4164.
8. H. wang, A. Mararenko, G. Gao, Z. Gai, K. Hang, P. Banerjee and S. Zhou, *ACS Appl. Mater.*, Interfaces 2014, **6,** 15309.
9. C. Loo, A. Lowery, N. Halas, J. West and R. Drezek, *Nano Lett.*, 2005, **5,** 709.
10. S. Lal, S. E. Clare and N. J. Halas, *Acc. Chem. Res.*, 2008, **41**, 1842.
11. S. Chen, Z. Fan and D. L. Carroll, *J. Phys. Chem. B.*, 2002, **106,** 10777.
12. S. Chen and D. L. Carroll, *Nano Lett.*, 2002, **2,** 1003.
13. M. R. Jones, K. D. Osberg, R. J. MacFarlane, M. R. Langille and C. A. Mirkin, *Chem. Rev.*, 2011, **111,** 3736.
14. Y. Sun and Y. Xia, *Science.*, 2002, **298**, 2176.
15. L. Gou and C. J. Murphy, *Nano Lett.*, 2003, **3,** 231.
16. D. Yu and V. W. Yam, *J. Am. Chem. Soc.*, 2004, **126,** 13200.
17. S. H. Im, Y. T. Lee, B. Wiley and Y. Xia, *Angew. Chem., Int. Ed.*, 2005, **44,** 2154.

18. Y. Xiong, B. Wiley, J. Chen, Z. Y. Li, Y. Yin and Y. Xia, *Angew. Chem., Int. Ed.*, 2005, **44,** 7913.
19. J. Chen, F. Saeki, B. J. Wiley, H. Cang, M. J. Cobb, Z. Y. Li, L. Au, H. Zhang, M. B. Kimmey, X. Li and Y. Xia, *Nano Lett.*, 2005, **5**, 473.
20. S. E. Skrabalak, J. Chen, Y. Sun, X. Lu, L. Au, C. M. Cobley and Y. Xia, *Acc. Chem. Res.*, 2008, **41**, 1587.
21. J. Chen, M. Yang, Q. Zhang, E. C. Cho, C. M. Cobley, C. Kim, C. Glaus, L. V. Wang, M. J. Welch and Y. Xia, *Adv. Funct.Mater.*, 2010, **20**, 3684.
22. P. S. Kumar, I. P. Santos, B. R. Gonzalez, F. J. G. deAbajo and L. M. L. Marzan, *Nanotechnology.*, 2008, **19**, 015606.
23. C. G. Khoury and T. Vo-Dinh, *J. Phys. Chem. C*, 2008, **112,** 18849.
24. B. D. Chithrani, A. A. Ghazani and W. C. W. Chan, *Nano Lett.*, 2006, **6**, 662.
25. B. D. Chithrani and W. C. W. Chan, *Nano Lett*., 2007, **7**, 1542.
26. S. E. A. Gratton, P. A. Ropp, P. D. Pohlhaus, J. C. Luft, V. J. Madden, M. E. Napier and J. M. De Simone, *Proc. Natl. Acad. Sci. U. S. A.*, 2008, **105**, 11613.
27. E. Blanco, H. Shen and M. Ferrari, *Nature Biotechnology*, 2015, **33**, 941.
28. R. K. Jain and T. Stylianopoulos, *Nat. Rev. Clin.Oncol.*, 2010, **7**,653.
29. Y. Cheng, J. D. Meyers, A. M. Broome, M. E. Kenney, J. P. Basilion and C. Burda, *J. Am. Chem. Soc*., 2011, **133**, 2583.
30. H. S. Choi, W. Liu, P. Misra, E. Tanaka, J. P. Zimmer, B. I. Ipe, M. G. Bawendi and J. V. Frangioni, *Nat. Biotechnol*., 2007, **25**,1165.
31. A. Albanese, E. A. Sykes and W. C. M. Chan, *ACS Nano.*, 2010, **4**, 2490.
32. P. V. Kamat, *J. Phys. Chem. C*., 2007, **111**, 2834.

33. C. Y. Huang, D. Y. Wang, C. H. Wang, Y. T. Chen, Y. T. Wang, Y. T. Jiang, Y. J. Yang, C. C. Chen and Y. F. Chen, *ACS Nano*., 2010, **4**, 5849.
34. K. Tvrdy, P. A. Frantsuzov and P. V. Kamat, *Proc. Natl. Acad. Sci. U. S. A.*, 2011, **108**, 29.
35. J. S. Lee, M. V. Kovalenko, J. Huang, D. S. Chung and D. V. Talapin, *Nat. Nanotechnol*., 2011, **6**, 348.
36. C. J. Murphy, *Anal. Chem*., 2002, **74**, 520A.
37. P. W. Barone, S. Baik, D. A. Heller and M. S. Strano, *Nat. Mater*., 2005, **4**, 86.
38. P. K. Jain, X. Huang, I. H. El-Sayed and M. A. El-Sayed, *Acc. Chem. Res*., 2008, **41**, 1578.
39. P. Buecker, E. Trileva, M. Himmelhaus and R. Dahint, *Langmuir*., 2008, **24**, 8229.
40. W. S. Chang, J. W. Ha, L. S. Slaughter and S. Link, *Proc. Natl. Acad. Sci. U. S. A*., 2010, **107**, 2781.
41. S. Bai, J. Hu, D. Li, R. Luo, A. Chen and C. C. Liu, *J. Mater. Chem*., 2011, **21**, 12288.
42. X. Chen, S. Shen, L. Guo and S. S. Mao, *Chem. Rev*., 2010, **110**, 6503.
43. C. Burda, Y. Lou, X. Chen, A. C. S. Samia, J. Stout and J. L. Gole, *Nano Lett*., 2003, **3**, 1049.
44. X. Chen and C. Burda, *J. Am. Chem. Soc*., 2008, **130**, 5018.
45. Y. Zhao, X. Qiu and C. Burda, *Chem. Mater*., 2008, **20**, 2629.
46. S. I. Naya, A. Inoue and H. Tada, *J. Am. Chem. Soc*., 2010, **132**, 6292.
47. J. Wang, B. Mao, J. L. Gole and C. Burda, *Nanoscale*., 2010, **2**, 2257.
48. J. L. Gole, S. M. Prokes, O. J. Glembocki, J. Wang, X. Qiu and C. Burda, *Nanoscale*., 2010, **2**, 1134.

49. N. R. Jana, *Phys. Chem. Chem. Phys*., 2011, **13**, 385.

50. X. Huang, I. H. El-Sayed and M. A. El-Sayed, *Methods Mol. Biol*., 2010, **624**, 343.

51. M. Howarth, W. Liu, S. Puthenveetil, Y. Zheng, L. F. Marshall, M. M. Schmidt, K. D. Wittrup, M. G. Bawendi and A. Y. Ting, *Nat. Methods*., 2008, **5**, 397.

52. W. Liu, M. Howarth, A. B. Greytak, Y. Zheng, D. G. Nocera, A. Y. Ting and M. G. Bawendi, *J. Am. Chem. Soc*., 2008, **130**, 1274.

53. P. M. Allen, W. Liu, V. P. Chauhan, J. Lee, A. Y. Ting, D. Fukumura, R. K. Jain and M. G. Bawendi, *J. Am. Chem.Soc*., 2010, **132,** 470.

54. A. Vogel and V. Venugopalan, *Chem. Rev.*, 2003, **103,** 577.

55. A. P. Alivisatos, *Science.*, 1996, **271**, 933.

56. X. Huang, S. Neretina and M. A. El-Sayed, *Adv. Mater*., 2009, **21**, 4880.

57. M. C. Daniel and D. Astruc, *Chem. Rev*., 2004, **104**, 293.

58. P. K. Jain, K. S. Lee, I. H. El-Sayed and M. A. El-Sayed, *J. Phys. Chem. B*., 2006, **110**, 7238.

59. A. J. Murphy, T. K. Sau, A. M. Gole, C. J. Orendorff, J. Gao, L. Gou, S. E. Hunyadi and T. Li, *J. Phys. Chem. B.*, 2005, **109**,13857.

60. V. P. Torchilin, *Nat. Rev. Drug Discov.*, 2005, **4**, 145.

61. M. C. Woodle, *Adv Drug Deliv Rev*., 1995, **16,** 249.

62. G. Gregoriadis and A. T. Florence, *Drugs.*, 1993, **45**, 15.

63. D. A. LaVan, D. M. Lynn and R. Langer, *Nat. Rev. Drug Discov.*, 2002, **1**, 77.

64. F. Alexis, E. Pridgen, L. K. Molnar and O. C. Farokhzad, *Mol Pharm.* 2008, **5**, 505.

65. K. J. Cho, X. Wang and S. M. Nie, *Clin Cancer Res.,* 2008, **14,** 1310.
66. M. L. Adams, A. Lavasanifar and G. S. Kwon, *J Pharm Sci.,* 2003, **92**, 1343.
67. K. Kataoka, A. Harada and Y. Nagasaki, *Adv Drug Deliv Rev*. 2001, **47**, 113.
68. X. T. Shuai, H. Ai, N. Nasongkla, S. Kim and J. Gao, *J. Control Release.,* 2004, **98**, 415.
69. S. M. Moghimi, *Anti Cancer Agents Med Chem.,* 2006, **6**, 553.
70. P. Couvreur, C. Dubernet and F. Puisieux, *Eur J Pharm Biopharm.,* 1995, **41,** 2.
71. G. S. Kwon, *Crit Rev Ther Drug Carrier Syst.,* 1998, **15**, 481.
72. D. W. Kim, S. Y. Kim and H. K. Kim, *Ann Oncol.,* 2007, **18**, 2009.
73. C. C. Lee, *Nat. Biotechnol*., 2005, **23**, 1517.
74. T. M. Allen and P. R. Cullis, *Science*., 2004, **303**, 1818.
75. D. S. Castro, J. A. C. Morales, M. T. R. Apan and P. Guadarrama , *Bioorg Chem*., 2012, **41**, 13.
76. R. Duncan and L. Izzo, *Adv Drug Deliv Rev.,* 2005, **57**, 2215.
77. D. L. Patton, Y. T. Cosgrove Sweeney, T. D. McCarthy and S. L. Hillier, *Antimicrob Agents Chemother.,* 2006, **50**, 1696.
78. D. A. Tomalia, *Prog Polym Sci.,* 2005, **30**, 294.
79. R. Hirlekar, M. Yamagar, H. Garse, M. Vij, and V. Kadam, *Asian Journal of Pharmaceutical and Clinical Research.,* 2009, **2**, 17.
80. B. G. P. Singh, C. Baburao, V. Pispatietal, H. Pathipati, N. Muthy, SRV. Prassana and B. G. Rathode, *International Journal of Research in Pharmacy and chemistry*, 2012, **2**, 523.
81. Y. Usui, H. Haniu, S. Tsuruoka, and N. Saito, *Med. Chemistry.,* 2012, **2**, 1.

82. Y. Zhang,Y. Bai and B.Yan, *Drug Discovery Today.*, 2010, **15**, 428.
83. I. L. Medintz, *Nat. Mater.*, 2005, **4**, 435.
84. J. Lee, D. K. Chatterjee, M. H. Lee and S. Krishnan, *Cancer Letters*., 2014, **347**, 46.
85. X. Huang, *Nanomed.*, 2007, **2**, 681.
86. F. A. Jaffer and R. Weissleder, *JAMA*., 2005, **293**, 855.
87. J. M. Perez, F. J. Simeone, Y. Saeki, L. Josephson and R. Weissleder, *Jam Chem Soc*. 2003, **125**, 10192.
88. M. Lewin, N. Carlesso, C. H. Tung, X. W. Tang, D. Cory, D. T. Scadden and R. Weissleder, *Nat Biotechnol*. 2000, **18**, 410.
89. M. Y. Hua, H. W. Yang and H. L. Liu, *Biomaterials*. 2011, **32**, 8999.
90. U. O. Hafeli, S. M. Sweeney, B. A. Beresford, J. L. Humm and R. M. Macklis, *Nucl Med Biol*., 1995, **22**, 147.
91. X. Y. Ying, Y. Z. Du, L. H. Hong, H. Yuan and F. Q. Hu, *J Magn Magn Mater*., 2011, **323**, 1088.
92. N. Nitin, L. E. LaConte, O. Zurkiya, X. Hu and G. Bao, *J Biol Inorg Chem*., 2004, **9**, 706.
93. A. A. Jr. Bogdanov, C. Martin, R. Weissleder and T. J. Brady, *Biochim Biophys Acta.*, 1994, **1193**, 212.
94. J. W. Bulte and M. DeCuyper, *Methods Enzymol*., 2003, **373**, 175.
95. J. W. Douglas and T. S. Mann, *J Magn Reson Imaging*., 1994, **4**, 497.
96. C. Wilhelm, C. Billotey, J. Roger, J. N. Pons, J. C. Bacri and F. Gazeau, *Biomaterials*., 2003, **24**, 1001.
97. W. Jiang, Z. Sun, F. Li, K. chen, T. Liu, J. Liu, T.Zhou and R. Guo., *J Magn Magn Mater*., 2011, **323**, 435.
98. J. J. Lin, J. S. Chen and S. J. Huang, *Biomaterials*., 2009, **30**, 5114.

99. O. Veiseh, F. M. Kievit and C. Fang, *Biomaterials*., 2010, **31**, 8032. P. Y. Chen, H. L. Liu and M. Y. Hua, *Neuro Oncol*., 2010,**12**, 1050.

100. A. J. Cole, A. E. David, J. Wang, C.J. Galban, H.L. Hill and V.C. Yang, *Biomaterials.,* 2011, 32, 2183.

101. W. J. Rogers and P. Basu, *Atherosclerosis*., 2005, **178**, 67.

102. Y. Liu, Y. Zhao, B. Sun and C. Chen, Acc. Chem. Res., 2012, 46, 702.

103. A. A. Shvedova, V.E. Kagan and B. Fadeel, Annu. Rev. Pharmacol. Toxicol., 2010, 50, 63.

104. M.V. Yezhelyev, X. Gao, Y. Xing, A. Al-Hajj, S. Nie and R. M. O'Regan, *Lancet Oncol*., 2006, **7**, 657.

105. U. Pison, T. Welte, M. Giersig and D. A. Groneberg, *Eur. J. Pharmacol.*, 2006, **533**, 341.

106. R. M. Sawant , J. P. Hurley , S. Salmaso , A. Kale , E. Tolcheva , T. S. Levchenko and V. P. Torchilin , *Bioconjug.Chem*., 2006, **17**, 943.

107. Z. Medarova, W. Pham, C. Farrar, V. Petkova and A. Moore, *Nat.Med*., 2007, **13**, 372.

108. A. M. Derfus, A. A. Chen, D.H. Min, E. Ruoslahti and S. N. Bhatia, *Bioconjug. Chem.* 2007, **18**, 1391.

109. R. K. O'Reilly, M. J. Joralemon, C. J. Hawker and K. L. Wooley, *J Polymer Sci A Polym Chem.,* 2006, **44**, 5203.

110. L. B. Luo , J. Tam, D. Maysinger and A. Eisenberg . *Bioconjug Chem*., 2002, **13**,1259.

111. R. Savić, L. Luo, A. Eisenberg and D. Maysinger, *Science*., 2003, **300,** 615.

112. J. F. Hainfeld, D. N. Slatkin, T. M. Focella and H. M. Smilowitz, *Br J Radiol*., 2006, **79**, 248.

113. J. W. M. Bulte and D. L. Kraitchman, *Nmr Biomed*., 2004, **17**, 484.
114. H, Otsuka, Y, Nagasaki and K. Kataoka, *Adv Drug Deliv Rev*., 2003, **55**, 403.
115. S. Desset, O. Spalla, P. Lixon and B. cabane, *Langmuir*., 2001, **17**, 6408.
116. F. Caruso, R. A. Caruso and H. Mohwald, *Science.*, 1998, 282, 1111.
117. M. Filali, M. A. R. Meier, U. S. Schubert and J. F. Gohy, *Langmuir.*, 2005, **21**,7995.
118. B. S. Kim, J.M. Qiu, J..P Wang and T. A. Taton, *Nano Lett.*, 2005, **5**, 1987.
119. A. K. Gupta and A. S. G. Curtis, *Biomaterials*., 2004, **25**, 3029. 119. G. F. Paciotti, L. Myer, D. Weinreich, D. Goia , N. Pavel, R. E. McLaughlin and L. Tamarkin, *Drug Deliv*., 2004, **11**, 169.
120. C. Alexiou, R. Jurgons, G. Seliger, C. Seliger and H. Iro, *J Nanosci Nanotechnol*., 2006, **6**, 2762.
121. J. H. Lee, Y. W. Jun, S. I. Yeon, J. S. Shin and J. Cheon, *Angew Chem Int Ed*., 2006, **45**, 8160.
122. H. Y. Lee , Z. Li, K. Chen, A. R. Hsu, C. Xu, J. Xie, S. Sun and X. Chen, *J Nucl Med*., 2008, **49**, 1371.
123. J . Cheon and J. H. Lee, *Acc Chem Res.*, 2008, **141**, 1630.
124. S. Mornet, S. Vasseur, F. Grasset and E. Duguet , *J Mater Chem.*, 2004, **14**, 2161.
125. J. W. M. Bulte and D. L. Kraitchman, *Nmr Biomed*., 2004, **17**, 484.
126. C. Sun, J. S. H. Lee and M. Zhang, *Adv Drug Deliv Rev.*, 2008, **60**, 1252.
127. T. M. Allen and P. R. Cullis, *Science.*, 2004, **303**, 1818.
128. J. E. Lee, N. Lee, H. Kim, J. Kim, S. H. Choi, J. H. Kim, T. Kim, I. C. Song, S. P. Park, W. K. Moon, T. Hyeon, *J. Am. Chem. Soc.*, 2010, 132, 552-557.
129. L. Ao, B. Wang, P. Liu, L. Huang, C. Yue, D. Gao, C. Wu, W. Su, *Nanoscale*, 2014, **6**, 10710-10716.

130. E. J. Goh, K. S. Kim, Y. R. Kim, H. S. Jung, S. Beack, W. H. Kong, G. Scarcelli, S. H. Yun, S. K. Hahn, *Biomacromolecules*, 2012, **13**, 2554-2561.

131. M. P. Melancon, M. Zhou, R. Zhang, C. Xiong, P. Allen, X. Wen, Q. Huang, M. Wallace, J. N. Myers, R. J. Stafford, D. Liang, A. D. Ellington, C. Li, *ACS Nano*,2014, **8**, 4530-4538.

132. F. Fay, C. Scott, *J. Immunother.*, 2011, **3**, 381-94.

133. J. Yang, C. H. Lee, H. J. Ko, J. S. Suh, H. G. Yoon, K. Lee, Y. M. Huh and S. Haam., *Angew. Chem. Int. Ed. Engl*., 2007, **46**, 8836.

134. O. C. Farokhzad, J. Cheng, B. A. Teply, I. Sherifi,S. Jon, P. W. Kantoff, J. P. Richie, and R Langer, Proc. *Natl. Acad. Sci. U. S. A.*, 2006, **103**, 6315.

135. M. A. Ward and T. K. Georgiou, *Polymers.*, 2011, **3**, 1215.

136. B. Thiesen and A. Jordan, *Int. J. Hyperthermia*., 2008, **24**, 467.

137. K. M. Hauff, F. Ulrich, D. Nestler, H. Niehoff , P. Wust, B. Thiesen, H. Orawa, V. Budach and A. Jordan, *J. Neurooncol*., 2011, **103**, 317.

138. A. Jordan, R. Scholz, P. Wust, H. F ahling and R. Felix, *J. Magn. Magn. Mater*., 1999, **201**, 413.

139. P. Cherukuri, E. S. Glazer and S. A. Curley, *Adv. Drug Delivery Rev*., 2010, **62**, 339.

140. M. Arruebo, R. F. Pacheco, M. R. Ibarra and J. Santamaría, *Nano Today*., 2007, 2, 22.

141. G. R. Sun, M. Y. Berezin, J. D. Fan, H. Lee, J. Ma, K. Zhang, K. L. Wooley and S. Achilefu, *Nanoscale.*, 2010, **2**, 548.

142. M. De, S. Rana, H. Akpinar, O. R. Miranda, R. R. Arvizo, U. H. F. Bunz and V. M. Rotello, Nat. Chem., 2009, **1**, 461.

143. C. C. You, O. R. Miranda, B. Gider, P. S. Ghosh, I. B. Kim, B. Erdogan, S. A. Krovi, U. H. F. Bunz and V. M. Rotello, *Nat. Nanotechnol*., 2007, **2**, 318.

144. R. Minchin, *Nat. Nanotechnol*., 2008, **3**, 12.

145. N. Suthiwangcharoen, T. Li, K. Li, P. Thompson, S. J. You and Q. Wang, *Nano Res.*, 2011, **4**, 483.

146. M. Elsabahy and K. L. Wooley, *Chem. Soc. Rev*., 2012, **41**, 2545.

147. R. Nagarajan, *Amecrican Chemical Society*, 2012, **1119**.

148. N. Suthiwangcharoen and R. Nagarajan, *RSC Adv*., 2014, **4**,10076.

149. S. Laurent, D. Forge, M. Port, A. Roch, C. Robic, L. V. Elst and R. N. Muller, *Chem. Rev*. 2008, **108**, 2064.

150. A. K. Gupta, M. Gupta, Biomaterials 2005, 26, 3995.

151. M. Di Marco, M. Port, P. Couvreur, C. Dubernet, P. Ballirano, C. Sadun, *J. Am. Chem. Soc*. 2006, **128**, 10054.

152. L. X. Tiefenauer, G. Kuehne and R. Y. Andres, *Bioconjugate Chem.*, 1993, **4**, 347.

153. S. Nie, Y. Xing, G. J. Kim and J. W. Simons, *Annu. Rev. Biomed. Eng.*, 2007, **9**, 257.

154. J. Ross, P. Chaudhuri and M. Ratnam, *Cancer.*, 1994, **73**, 2432.

155. Y. Zhang, N. Kohler and M. Zhang, *Biomaterials.*, 2002, **23**, 1553.

156. N. Kohler, G. E. Fryxell and M. Zhang, *J. Am. Chem. Soc.*, 2004, **126**, 7206.

157. S. Wang, X. Shi, M. Van Antwerp, Z. Cao, S. Swanson, X. Bi and J. Baker, *Adv. Funct. Mater*., 2007, **17**, 3043.

158. C. Sun, J. S. H. Lee and M. Zhang, *Adv Drug Deliv Rev.,* 2008, **60,** 1252.

159. N. Kohler, C. Sun, A. Fichtenholtz, J. Gunn, C. Fang and M. Q. Zhang, *Small*., 2006, **2**, 785.

160. S. Mornet, S. Vasseur, F. Grasset and E. Duguet, *Journal Of Materials Chemistry.*, 2004, **14**, 2161.

161. C. Fonseca, S. Simoes and R. Gaspar, *J. Controlled Release.*, 2002, **83**, 273.

162. D. Bhadra, S. Bhadra, S. Jain and N. Jain, *Int. J. Pharm.,* 2003, **257**, 111.

163. A. S. L Lubbe, C. Bergemann, H. Riess, F. Schriever, P. Reichardt, K. Possinger, M. Matthias, B. Dorken, F. Herrmann, R. Gurtler, S. Hu-Lieskovan, J. D. Heidel, D. W. Bartlett, M. E. Davis and T. J. Triche, *Cancer Res.*, 2005, **65**, 8984.

164. X. Yang, H. Hong, J. J. Grailer, I. J. Rowland, A. Javadi, S. A. Hurley, Y. Xiao, Y. Yang, Y. Zhang, R. J. Nickles, W. Cai, D. A. Steeber and S. Gong, *Biomaterials.*, 2011, **32**, 4151.

165. K. H. Bae, M. Park, M. J. Do, N. Lee, J. H. Ryu, G. W. Kim, C. Kim, T. G. Park and T. Hyeon, *ACS Nano*, 2012, **6**, 5266.

166. F. H. Chen, L. M. Zhang, Q. T. Chen, Y. Zhang and Z. J. Zhang, *Chem Commun*., 2010, **46**, 8633.

167. C. E. Nelson, J. R. Kintzing, A. Hanna, J. M. Shannon, M. K. Gupta and C. L. Duvall, *ACS Nano.*, 2013, **7**, 8870.

168. A. Villanueva, P. D. L. Presa, J. M. Alonso, T. Rueda, A. Martinez, P. Crespo, M. P. Morales, M. A. G. Fernandez, J. Valdes and G. Rivero, *J. Phys. Chem.,* 2010, **114**, 1976.

169. S. H. Hu, T. Y. Liu, H. Y. Huang, D. M. Liu and S. Y. Chen, *Langmuir.*, *2008*, **24**, 239.

170. L. H. Reddy, J. L. Arias, J. Nicolas and P. Couvreur, *Chem. Rev*., 2012, **112**, 5818.

171. S. Murakami, T. Hosono, B. Jeyadevan, M. Kamitakahara and K. Ioku, *J. Ceram. Soc. Jpn.*, 2008, **116**, 950.

172. K. Ariga, A. Vinu, Y. Yamauchi, Q. Ji and J. P. Hill, *Bull. Chem. Soc. Jpn.*, 2012, **85**, 1.

173. D. Tarn, C. E. Ashley, M. He, E. C. Cames, J. I. Zink and C. J. Brinker, *Acc. Chem. Res.*, 2013, **46,** 792.

174. B. S. Lee, L. C. Huang, C. Y. Hong, S. G. Wang, W. H. Hsu, Y. Yamauchi, C. J. Hsieh, J. Y. Lai and K. C. W. Wu, *Acta Biomater.*, 2011, **7**, 2276.

175. B. J. Lopez, C. Boissiere, C. Chaneac, D. Groso, S. Vasseur, S. Miraux, E. Duguet and C. Sanchez, *J. Mater.Chem.*, 2007, **17**, 1563.

176. E. R. Hernandez, A. L. Noriega, D. Arcos, I. I. Barba, O. Terasaki and M. V. Regí, *Chem. Mater.*, 2007, **19**, 3455.

177. F. Lu, A. Popa, S. Zhou, J. J. Zhu and A. C. S. Samia, *Chem.Commun.*, 2013, **49**, 11436.

178. M. C. Chang, C. C. Ko and W. H. Douglas, *Biomaterials*, 2003, **24,** 2853.

179. T. Zhaomin, Z. Yangbo, S. Huili, L. Dan and Z. Shaobing, *European Journal of Pharmaceutics and Biopharmaceutics.*, 2014, **87**, 90.

180. T. Y. Liu and T. C. Huang, *Acta Biomater.*, 2011, ***7,*** 3927.

181. W. K. Oh, H. Yoon and J. Jang, *Biomaterials.*, 2010, **31**, 1342.

182. H. A. Schreiber, J. Prechl, H. Jiang, A. Zozulya, Z. Fabry, F. Denes and M. Sandor, *J. Immunol. Methods*, 2010, **356,** 47.

183. I. Sharifi, H. Shokrollahi and S. Amiri, *J. Magn. Magn. Mater.*, 2012, **324**, 903.

184. R. M. Mohamed, M. M. Rashad, F. A. Haraz and W. Sigmund, *J. Magn. Magn. Mater.*, 2010, **322**, 2058.

185. B. E. Kashevsky, V. E. Agabekov, S. B. Kashevsky, K. A. Kekalo, E. Yu. Manina, I. V. Prokhorov and V. S. Ulashchik, *J. Partic.*, 2006, **6**, 322.

186. S. Ayyappan, J. Philip and B. Raj, *J. Mate. Chem. Phys.*, 2009, **115**, 712.

187. O. Caltun, I. Dumitru, M. Feder, N. Lupu and H. Chiriac, *J. Magn. Magn. Mater.* 2008, **320**, 869.

188. A. Španová, B. Rittich, M. Beneš and D. Horák, *J. Chroma.*, 2005, 1080, 93.
189. S. W. Lee, S. Bae, Y. Takemura, I. Shim, T. M. Kim, J. Kim, H. J. Lee, S. Zurn and C. S. Kim, *J. Magn. Magn. Mater.*, 2007, **310**, 2868.
190. D. Kim, D. E. Nikles, D. T. Johnson and C. S. Brazel, *J. Magn. Magn. Mater*. 2008, **320**, 2390.
191. Sharifi, H. Shokrollahi and S. Amiri, *J. Magn. Magn. Mater*. 2012, **324**, 903.
192. Q. Song and Z. J. Zhang, *J. Phys. Chem.*, 2006, **110**, 11205.
193. Q. A. Pankhurst, J. Connolly, S. K. Jones and J. Dobson, *J. Appl. Phys D.* 2003, **36**, 167
194. R. E. Rosensweig, *J. Magn. Magn. Mater*., 2002, **252**, 370.
195. D. Kim, D. E. Nikles, D. T. Johnson and C. S. Brazel, *J. Magn. Magn. Mater*., 2008, **320**, 2390.
196. C. S. Brazel, *J. Pharm. Res.*, 2009, **26**, 644.
197. H. M. Joshi, Y. P. Lin, M. Aslam, P. V. Prasad, E. A. S. Sikma, R. Edelman, T. Mead and V. P. Dravid, *J. Phys. Chem.*, 2009, **113**, 17761.
198. R. H. Kodama, *Journal of Magnetism and Magnetic Materials*. 1999, **200**, 359.
199. C. R. Vestal, and Z. J. Zhang, *Journal of American Chemical Society*, 2003, **125**, 9828.
200. A. Ditsch, P. E. Laibinis, I. C. Wang and T. A. Hatton, *Langmuir*, 2005, **21**, 6006.

Chapter-2

One pot synthesis of uniform and spherically assembled functionalized MFe_2O_4 (M= Co, Mn, Ni) nanoparticles

2.1. Introduction

Monodisperse magnetic nanoparticles and nanoassemblies are currently of emerging interest because of their unique physico-chemical properties and wide applications in memory storage devices, catalysis, sensors, MRI, magnetically controlled drug delivery and hyperthermia treatment of tumour cells.[1-3] Nano sized magnetic particles have physical and chemical properties that are characteristics of neither the atom nor the bulk counterparts. The large surface area and quantum size effect of magnetic nanoparticles dramatically change some magnetic properties and exhibit superparamagnetic phenomena and quantum tunnelling of magnetization. Among the materials explored so far, spinel ferrites MFe_2O_4 (M = Co, Mn, Ni) are emerging as promising materials especially for biomedical applications.

Compared to iron oxide nanoparticles, spinel ferrites provide flexibility to control both crystal structures and magnetic properties by choosing different non-iron metals in spinel ferrite backbone and controlling their molar concentrations.[4] Hence the surface of these magnetic nanoparticles could be modified through the creation of few atomic layers of organic polymer or inorganic metals (e.g. gold) or oxide surfaces (e.g. silica or alumina), suitable for further functionalization by the attachment with various bioactive molecules. They are either dispersed through a large volume of a polymeric bead or occur as core in colloidal reagent with a biodegradable shell. As the magnetic particles accumulates in tumour tissue, they can play an important role in detection through MRI or electron microscopic imaging to locate and measure the therapeutic effect of anticancer drugs. Therefore, research on development of fabrication methods for ferrite nanoparticles with desirable magnetic property, acceptable chemical stability and surface chemistry that allow straight forward functionalization with different surface active moieties has continued to attract interest of several research groups.

A number of chemical routes have been utilized for the controlled synthesis of

monodispersed ferrite particles and to establish the correlation between magnetic properties and synthetic conditions. Techniques such as coprecipitation,[5] sol-gel,[6] microemulsion[7] and microwave,[8] ultrasound irradiation,[9] have been employed to prepare ferrite nanoparticles. But synthesis of strictly monodisperse particles, precise control of their size, shape and surface was still a challenge. Recently thermal decomposition technique offered an opportunity to prepare monodispersed magnetic nanoparticles. Sun and Zeng[10] have succeeded in synthesizing metal ferrites using $Fe(acac)_3$ as the precursor. Yànez-Vilar et al. adapted the same method to synthesize single phase nanosized MFe_2O_4 (M = Co, Mn and Ni) nanoparticles.[11]

On the other hand, self-assembly of magnetic nanoparticles based on selective control of non-covalent interactions[12-15] not only acts as a powerful tool for the creation of structured systems at a molecular level, but also provides a direct bridge between nanoscale objects and the macroscale devices.[16] Monolayer-functionalized nanoparticles can be made with a wide variety of metallic and non-metallic cores, providing a versatile building block for such approaches. The integrity of the building blocks based on selfassembly might provide a fascinating strategy for designing frameworks with for desirable shapes and sizes. To date, a number of methods have been developed to fabricate magnetic nanoparticle clusters with uniform size.[17,18] An efficient approach that has gained popularity for well defined clusters is the use of self-assembled structures such as polymers or surfactants. Yin et al. reported the synthesis of monodisperse magnetite colloidal clusters composed of small primary nanocrystals by high temperature solution phase process using poly(acrylic acid).[19] Amine functionalized Fe_3O_4 with high T_2 effect have recently reported by Barik et al. which ideally suited their use as contrast agent in MRI.[20] Cheng et al. have developed a facile polyol process to synthesize carboxyl-functionalized magnetite nanoclusters using urea as homogeneous precipitator and sodium acetate as stabilizer.[21] Self-assembly of magnetite and maghemite nanoparticles into necklace like nanorings is reported by Hui et al.[22] Although momentous progress has been made in studies on

iron oxide nanoparticle assemblies, other ferrites are less explored in this direction.In the present work we have employed a cost-effective, eco-friendly, one-pot solution Phase method to synthesize highly hydrophilic uniform spherical nanoassemblies of ultra-small amine-functionalized MFe_2O_4 (M=Co, Ni, Mn) nanoparticles. Our synthesis method mainly involves heating low cost metal chloride precursors in ethylene glycol in presence of weak base sodium acetate and ethanolamine. Ethanolamine meets both the purpose of stabilizer as well as surface functionalization with $–NH_2$ groups. The effects of the nature of the base, reaction temperature and ethanolamine concentration on aggregate size have been thoroughly investigated through DLS measurements.

2.1. Experimental

Materials

All chemicals were of analytical grade and used without further purification. All metal chlorides were taken from Merck, India. Ethylene glycol and ethanolamine have been procured from Sigma–Aldrich.

Synthesis of amine functionalized MFe_2O_4 (M= Co, Mn, Ni) nanoparticles

Amine functionalized superparamagnetic MFe_2O_4 nanoparticles were prepared by thermal decomposition of MCl_2 and $FeCl_3$ in ethylene glycol in the presence of sodium acetate and ethanolamine (Fig. 2.1). Briefly, anhydrous $FeCl_3$ (4.2 mmol) and $MCl_2{\cdot}7H_2O$ (2.1mmol) were taken in 30 ml ethylene glycol and 0.5 g of sodium acetate was added to it. The above solution was stirred for 30 minutes followed by the addition of 15 ml of ethanolamine. Now the entire solution was heated at 150 °C for 6 h during which fine black colloidal particles appeared in the reaction mixture.

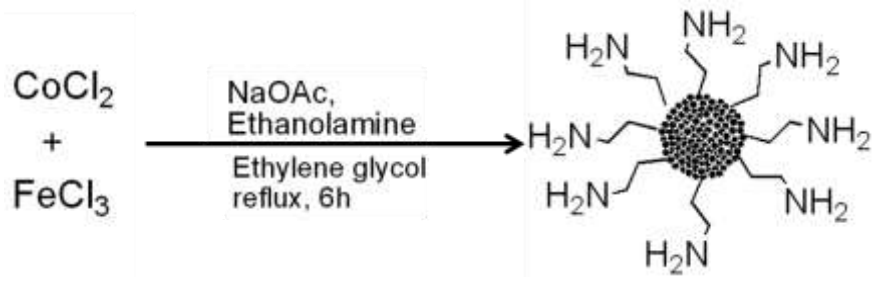

Fig. 2.1 Schematic representation for synthesis of amine functionalized MFe_2O_4 nanoparticles.

After that it was cooled down to room temperature. The particles were recovered using a magnetic separator (DynaMag2, Invitrogen) washed with Millipore water (5 × 5 ml) and dried in hot air oven at 80 °C for 2 h.

2.3. Characterization

The identification of the crystalline phase of the synthesized ferrite particles was performed by an Expert Pro Phillips X-ray diffractometer. The morphology and microstructure were analysed using scanning electron microscope (HITACHI COM-S-4200) and high resolution transmission electron microscopy (JEOL 3010, Japan) operated at 300 KV. The particle sizes from TEM micrographs were calculated using image J software. The hydrodynamic size and dispersion stability of particle aggregates were investigated through dynamic light scattering using a Malvern ZS90 zetasizer. Hydrodynamic size was measured by dispersing 0.1 mg of sample in 1 ml phosphate buffered saline. The surface charge was determined through zeta potential measurements. The pH was adjusted between 4 and 9 using dilute NaOH/HCl solutions for both HD size and zeta potential measurements. The surface chemistry of the nanoparticles was studied using FTIR spectroscopy (Perkin Elmer (BX 12)). The surface composition of different nanoparticles was investigated through X-ray

photoelectron spectroscopy in an ESCA-2000 (VG microtech) apparatus. Magnetic measurements were performed in a SQUID magnetometer.

2.4. Results and discussion

XRD analysis

X-ray diffraction analysis (Fig. 2.2) shows that in all metal cases the diffraction pattern perfectly matches with the expected cubic spinel structure of Co, Mn and Ni ferrites and has been identified as $CoFe_2O_4$ (JCPDS no. 03-0864), $MnFe_2O_4$ (JCPDS no. 10-0319) and $NiFe_2O_4$ (JCPDS no. 03-0875) respectively. The crystallite sizes were calculated using Scherer's equation taking into account broadening of each diffraction peak and are summarized in Table 1.

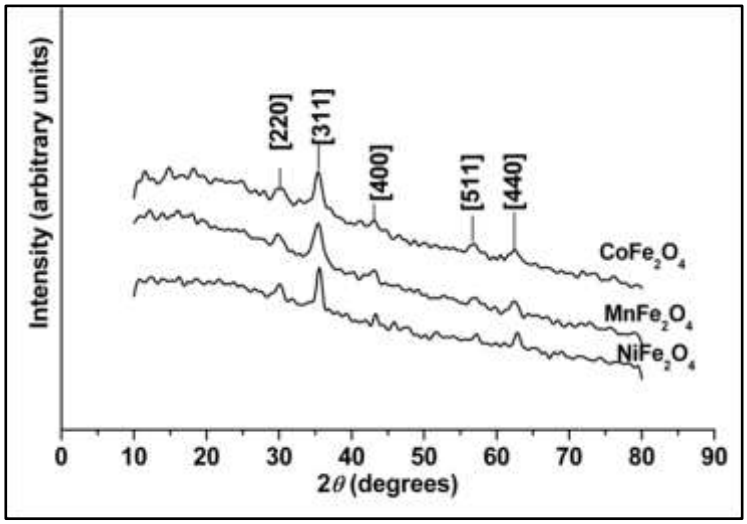

Fig. 2.2 XRD patterns of MFe_2O_4 (M = Co, Mn, Ni) nanoparticles. The planes corresponding to each peak have been indicated at the top of the graphs.

The lattice parameters calculated from reflections of [400] plane is 8.36 Å, 8.4 Å and 8.32 Å for $CoFe_2O_4$, $MnFe_2O_4$ and $NiFe_2O_4$ respectively. The most important and interesting observation is that effective broad peaks in case of all ferrites indicate fine nanocrystalline nature of samples.

TEM

Fig. 2.3(a)-(h) shows representative TEM micrographs of synthesized ferrite nanoparticles. In all cases spherical particles of size 35–50 nm were produced (Table 2.1). These spherical nanoassemblies are discrete, well defined and porous in nature. In case of $MnFe_2O_4$, these spherical particles further assemble to produce necklace like structures unlike $CoFe_2O_4$. This is possibly due to higher magnetization of $MnFe_2O_4$ which promotes further aggregation. Fig. 2.3(b) and (g), showing images at higher magnification indicate that each spherical particle is an assembly of primary cubic nanocrystals of about 4–5 nm and worm-like pores of about 2–3 nm. These ultrafine nanocrystals spatially assembled spontaneously to give porous spherical superstructures in order to minimize their surface energy. The high resolution TEM image of $CoFe_2O_4$ (Fig. 2.3c) shows a single aggregate, where the parallel lattice fringe is uniformly extended over the primary building blocks, grain boundaries and pores. Similar result was also obtained by Cannas et al.[18] in case of spherical nano-aggregates of $CoFe_2O_4$ nanoparticles synthesized by surfactant assisted route. Thus it can be concluded that the nanoparticles are organized into an oriented attached structure by sharing identical lattice planes. The lattice plane distance was calculated to be 1.69 Å from the image which corresponds to the reflection of [211] plane in the cubic $CoFe_2O_4$. Similar observations were found in case of $MnFe_2O_4$ and $NiFe_2O_4$ particles. From the selected area electron diffraction pattern the corresponding planes were calculated using the relation:

$$d = \frac{\lambda L}{R}$$

Where = wave length of electron wave; L = camera length; R = radius of diffraction ring.

d = Interplannar distance between two lattice planes.

The d values indexed in SAED pattern for each ferrite samples correlate with XRD pattern d_{XRD} is the crystallite size of the grain calculated using Scherrer's

equation; a is the lattice parameter obtained from XRD experiments; d_{DLS} is the hydrodynamic size of ferrite nanoparticles observed in PBS (pH 7.4).

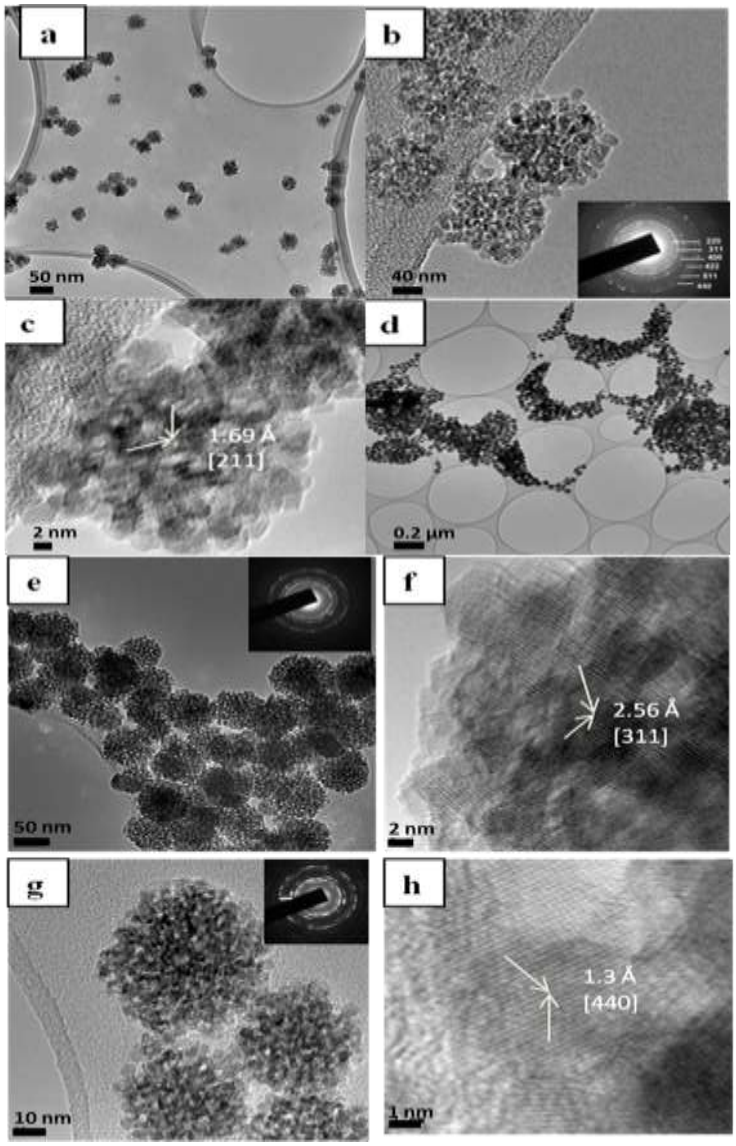

Fig. 2.3 TEM images of (a and b) $CoFe_2O_4$, (d and e) $MnFe_2O_4$, (g) $NiFe_2O_4$ at different magnifications; (c, f and h) HRTEM images of $CoFe_2O_4$, $MnFe_2O_4$, and $NiFe_2O_4$ respectively. The insets are the corresponding SAED patterns.

Table 2.1

Physical characteristics of different ferrite nanoparticles

Sample	d_{XRD} (nm)	a(Å)	d_{DLS} (nm)	d_{TEM} (nm)	d_{BET} (nm)	M_s(e.m.u/g)	S_{BET} (m^2/g)	n(NH_2) (mmol/g)
$CoFe_2O_4$	9.5	8.36	52.85	35	5	59.4	214	$4.8x10^{-5}$
$MnFe_2O_4$	8.8	8.4	70.89	3.8	56	56	279	$4.2x10^{-5}$
$NiFe_2O_4$	10.2	8.32	53.39	3.7	40.88	40.88	285	$3.9x10^{-5}$

d_{XRD} is the crystallite size of the grain calculated using Scherrer's equation; a is the lattice parameter obtained from XRD experiments; d_{DLS} is the hydrodynamic size of ferrite nanoparticles observed in PBS (pH 7.4) using dynamic light scattering; d_{TEM} is the diameter of spherical assemblies observed by TEM; M_s is the saturation magnetization at room temperature; d_{BET} is the particle size calculated from specific surface area; S_{BET} specific surface area and n is the density of $–NH_2$ groups present on the surface.

Plausible mechanism for the formation of MFe_2O_4 nanoparticles

Formation of magnetic particles can be explained according to the well-known polyol method of synthesis.[25, 27-28] In our system ethanolamine acts as a strong complexing agent for cobalt and iron ions as observed by instantaneous colour change upon addition of ethanolamine to the solution of M(II) and Fe(III) in ethylene glycol. With increase in temperature metal ions are slowly released into the solution and combined with $[OH^-]$ to give MFe_2O_4. The effect of base on aggregate size has been investigated (Table 2.2) and it is found that in presence of stronger bases larger aggregates are formed. It is possibly due to rapid formation of ferrite mass in presence of high concentration of $[OH^-]$. The same trend was observed even when volume of ethanolamine increases in the reaction medium. At higher concentration of ethanolamine size of the ferrite particles was drastically increased (Table 2.3) due to higher pH. Using a weak base such as NaOAC at optimum concentration of

ethanolamine the mass formation takes place slowly in a controlled manner. In addition to this at high temperature ethylene glycol is oxidized to glycolic acid aerially and creates an oxygen deficient atmosphere which further protects the ferrite nanoparticles from being oxidized to hydroxides as shown in equation 2.1.[28]

$$CoFe_2O_4 + 0.25\ O_2 + 4.5\ H_2O \longrightarrow Co(OH)_2 + Fe(OH)_3 \quad \text{---------} \quad 2.1$$

The ferrite particle formation proceeds in a controlled manner due to synergic effect of ethylene glycol and ethanolamine. In addition to this, ethanolamine acts as a nucleation and growth controlling as well as amine functionalizing agent for ferrite nanoparticles. From the TEM image it was observed that nanoparticles are organized into an isooriented attached structure by sharing identical lattice planes. From this observation oriented attachment growth mechanism can be proposed for the formation of clusters.[29–31] The clusters are formed from self-assembly of ultrafine particles by sharing common crystallographic orientation. The driving force for such spontaneous arrangement is that the elimination of pairs of high energy surfaces which will lead to reduction of surface free energy from thermodynamic view point. The formation of such nanoassemblies may be dependent on the collective behaviour of nanoparticles and intermolecular forces existing between them.[32] The no. of $–NH_2$ groups present on each spherical assembly was determined using UV–visible spectroscopy according to the previously reported procedure,[33] and it was found that each porous particle of 40 nm size contains approximately 490 amine groups. The aqueous dispersion stability of magnetic nanoparticles is an important factor for their utilization in drug delivery as well as tumor diagnosis through MRI.

Table 2.2

Effect of base on aggregate size

Precursors	Base	Ethanolamine (ml)	Particle size (nm)
$CoCl_2.6H_2O+FeCl_3$	CH_3COONa	15	35
$CoCl_2.6H_2O+FeCl_3$	$Na_3C_6H_5O_7$	15	68
$CoCl_2.6H_2O+FeCl_3$	NaOH	15	40
$CoCl_2.6H_2O+FeCl_3$	NH_4OH	15	40
$CoCl_2.6H_2O+FeCl_3$	KOH	15	54

Table 2.3

Variation of particle size with different amount of ethanolamine

Precursors	Base	Ethanolamine (ml)	Particle size (nm)
$CoCl_2.6H_2O+FeCl_3$	CH_3COONa	5	56
$CoCl_2.6H_2O+FeCl_3$	CH_3COONa	15	35
$CoCl_2.6H_2O+FeCl_3$	CH_3COONa	25	86
$CoCl_2.6H_2O+FeCl_3$	CH_3COONa	35	90

Hydrodynamic size and zeta potential measurement

The hydrodynamic size, calculated from the diffusional properties of the particle is an indicative of the apparent size of the dynamic hydrated/solvated particle. It was observed that the hydrodynamic (HD) size of $CoFe_2O_4$ by DLS shows a narrow distribution of size from 50 to 60 nm with mean HD size 50.8 nm with polydispersity 0.2 (Fig. 2.4). When HD size was measured against time, it was found that there was absolutely no change in mean HD size up to 3 days. After that it was slightly increased to 70.8 nm and was consistent at 70.8 nm even after one week of incubation. This exceptional stability in aqueous medium may be attributed to the excellent hydrophilicity of the surface, contributed by surface $–NH_2$ groups. Measurement of size over pH (4–7.6) shows almost no change in mean HD size. The presence of free surface amine groups was further investigated by examining the surface charge properties over pH 3–7.4 by zeta potential measurement. It was found that at neutral pH the ZP is−5.65 mV i.e. slightly negative which agrees with

observations reported by Bae et.al.[30] With slight increase in pH there is substantial increase in ZP value which may be due to protonation of surface amine groups. The isoelectric point of synthesized $CoFe_2O_4$ was found to be 6.8 which is slightly greater than that of co-precipitated ferrite particle. This shifting in isoelectric point may be due to surface modification with $–NH_2$ groups.

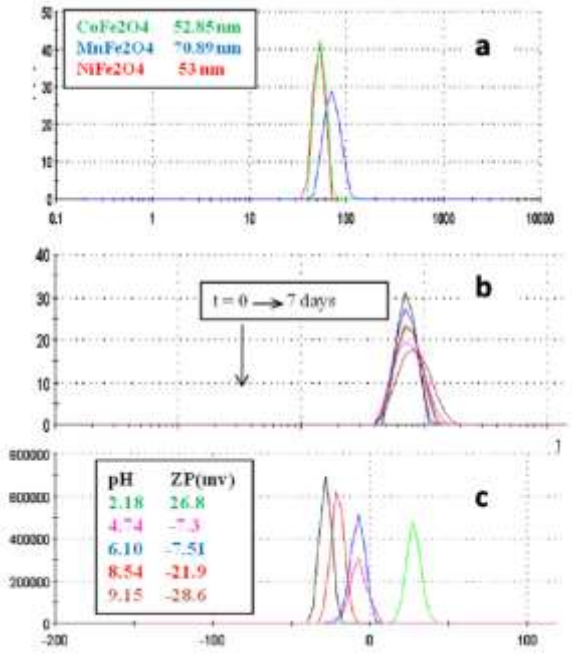

Fig. 2.4(a) Particle size distributions of ferrite nanoparticles. (b) Change in hydrodynamic size with time. (c) Variation of zeta potential with pH in case of $CoFe_2O_4$ nanoparticles.

FTIR Analysis

The IR spectra for all synthesized metal ferrites are shown in Fig. 2.5. The strong band at low frequency region (500–800 cm^{-1}) in each sample is ascribed to the M–O stretching in the oxide nanoparticles. The appearances of peaks at 890 and 1324 cm^{-1} correspond to the out of plane bending vibration of –N–H bond in primary amine and C–N stretching. This observation indicates the existence of ethanolamine molecules on nanoparticle surfaces. Therefore it can be concluded that nanoparticles are stabilized by ethanolamine through –OH group-metal complexation, which is further supported by ESCA (Electron spectroscopy for chemical analysis) analysis.

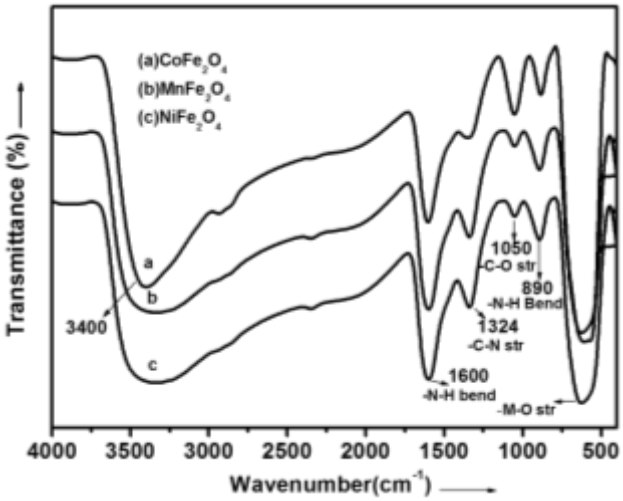

Fig. 2.5 FTIR spectra of $–NH_2$ spectra of $–NH_2$ functionalized $CoFe_2O_4$, $MnFe_2O_4$ and $NiFe_2O_4$ nanoparticles.

XPS Analysis

Fig. 2.6 shows representative XPS spectra of $CoFe_2O_4$. A careful observation of the peak corresponding to C1s region shows that the curve is well-fitted if it is considered as contributions from three peaks centered at 286.8, 289.07 and 290.8 eV. The C1s spectra corresponding to reference shows a shift of 2 eV to higher binding energy and hence taking the reference shift into consideration all other binding energies are to be evaluated. The Fe2p shows two peaks at 710.17 and 723.7 eV which is in consistency with Fe2p binding energy for cobalt ferrite nanoparticles.[31] Co2p spectrum shows peaks at 779 and 784 eV corresponding to $Co2p_{3/2}$ and $Co\ 2p_{1/2}$ electrons associated with corresponding shake ups at 785 and 801 eV. In addition to this the asymmetric nature of the peak is ascribed to Co^{2+} present in octahedral/tetrahedral sites.[32] The broad shoulder of O1s electron at 531.7 eV can be deconvoluted into two peaks centred at 531.5 and 533.2 eV corresponding to oxygen present in Fe–O and C–O bonds. In N1s region, a symmetric peak centred at 398.7 appears indicates the presence of only free $–NH_2$ groups on the surface of the

nanoparticles. The position of the peak well matches with that of N bonded to sp3 carbon as reported by Gammon et al.[37] So from XPS it is concluded that the ethanolamine has been chemically bonded on the surface of uniform sized spherical aggregates of ferrite nanoparticles through –OH site leaving $–NH_2$ as the pendant group which lead to the excellent stability of ferrite particles in aqueous medium (Fig. 2.1).

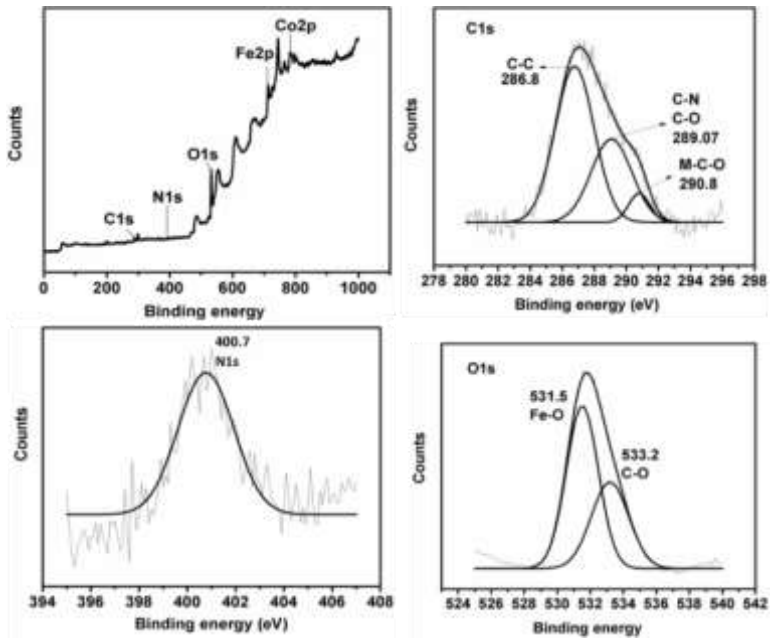

Fig. 2.6. XPS survey spectrum of $CoFe_2O_4$. High resolution scans corresponding to C1s, O1s, Fe 2p, N1s and Co2p binding energy.

Thermal analysis

The chemical bonding of ethanolamine on ferrite nanoparticles is further supported by thermal analysis. It was found that the density of amine groups is significantly high as compared to other previously reported methods by different research groups.[28,34] There are three weight loss steps in TG curves of ferrite nanoparticles (Fig. 2.7). The first mass loss of 1% (between 34 and 130°C) is due to removal of moisture from ferrite surface. The second weight loss above 150°C and

below 280°C is due to adsorbed water, ethylene glycol and ethanolamine. The loss of weight at temperatures higher than 410°C may be ascribed to the decomposition of surface bonded ethanolamine molecules which are mainly responsible for the excellent stability of the nanoparticles in the aqueous medium.

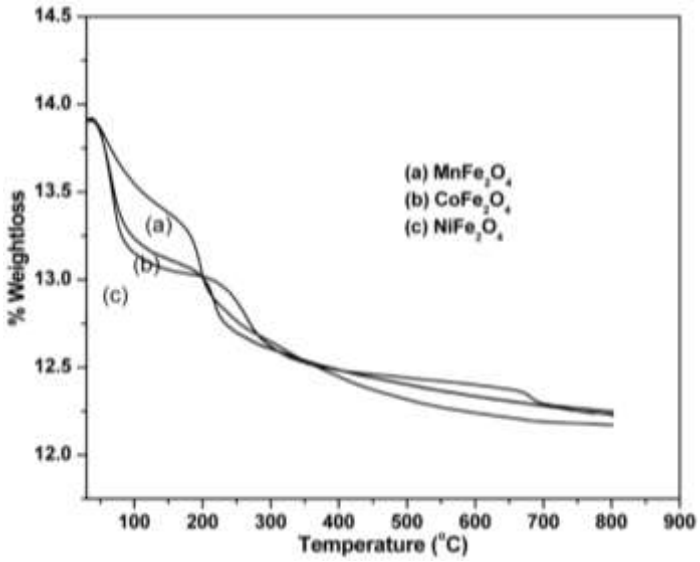

Fig. 2.7 Thermogravimetry curves of ferrite nanoparticles.

Nitrogen adsorption–desorption study

Nitrogen sorption experiment was conducted to further investigate the porous nature of ferrite nanoparticles. Fig. 2.8 represents the nitrogen adsorption–desorption isotherms and BJH pore size distribution curves of $CoFe_2O_4$ and $MnFe_2O_4$ nanoparticles. The isotherms are identified as type IV, which is characteristic of mesopores. It is notable that besides mesopores formed by aggregation of spherical particles; the BJH pore size distribution clearly indicates mesopores centred at 3–4 nm formed among the ultrafine nanoparticles within the aggregate which is in accordance with the TEM result. BET surface area of $CoFe_2O_4$ and $MnFe_2O_4$ powder were calculated to be 210 m^2/g and 209 m^2/g. To our knowledge surface area values for porous magnetic oxides synthesized by various other synthetic methods have not

exceeded 150 m^2/g.[18,28,35] Hence in the present synthetic route the surface area of magnetic oxides can be significantly increased and it would be particularly beneficial in bioseparation and drug delivery.

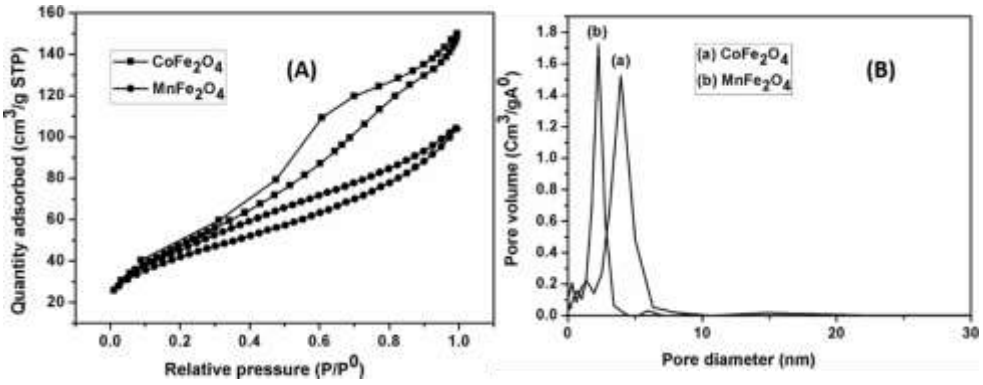

Fig. 2.8(A) Nitrogen adsorption–desorption isotherm and **(B)** Pore size distribution of $CoFe_2O_4$ and $MnFe_2O_4$.

Squid analysis

Fig. 2.9(a)–(c) shows the temperature dependent zero-field cooling and field-cooling curves of $CoFe_2O_4$, $MnFe_2O_4$ and $NiFe_2O_4$ nanoparticles. The magnetic behaviour shown by each ferrite sample can be interpreted according to TEM results. The curves are not superposing even at 300 K indicating the nanoparticles are more likely to be present in a ferrimagnetic state.[36] In case of FC (5 mT), there is slight increase in magnetization with decrease in temperature up to 160°C, and a constant trend is observed below 160°C. The magnetization measured under zero-field cooling condition continuously increases till 300 K with a broad hump around 150–160°C. This particular behaviour can be ascribed to the strong nanoparticle interactions forming an assembly which can lead to a collective magnetic order state with high anisotropy,[37] and this is also expected in case of iso-oriented ferrite nanoparticles. Field dependent magnetization curves of all three ferrite nanoparticles at room temperature are illustrated in Fig. 2.9d. The magnetization rose rapidly as the applied

field increased up to 1T and reached at a saturation point at 2 T. In all cases the saturation magnetizations (Ms) display higher values for synthesized nanoparticle assemblies than the corresponding nanodots. Ms values for synthesized $CoFe_2O_4$, $MnFe_2O_4$ and $NiFe_2O_4$ particles are found to be 59.4, 56 and 40.88 e.m.u./g, which are higher than Ms for corresponding nanodots 35 e.m.u./g, 27 e.m.u./g and 25 e.m.u./g,[38-40] but lower than their bulk counter parts 71.2, 80, 51 e.m.u./g respectively.[41–43] This decrease in Ms value could be mainly attributed to small particle surface effect (i.e. spin canting) that becomes more dominant as the particles are smaller.[44] The curves show almost no hysteresis opening and are completely reversible at room temperature. As observed by XRD and TEM the size of primary nanocrystals is 4–5 nm, which is smaller than superparamagnetic critical size of MFe_2O_4. Thus it is logical that synthesized clusters show superparamagnetic behaviour even though their size exceeds critical size and at the same time the improved coalescence of crystallites in the nanostructures results in increased magnetic coupling and higher magnetization. The magnetic on–off switching behaviour owing to superparamagnetism is particularly advantageous in bioseparation, magnetic resonance imaging as well as magnetically controlled drug delivery.

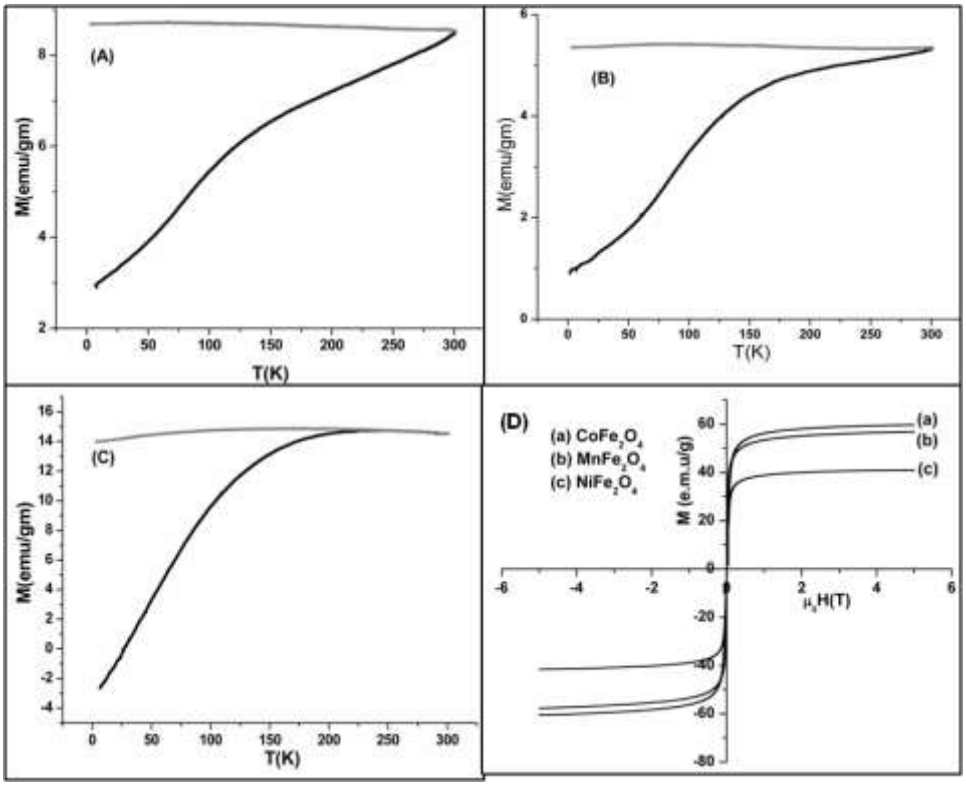

Fig. 2.9 Zero-field-cooling (black) and field-cooling (grey) curves of (a) $CoFe_2O_4$, (b) $MnFe_2O_4$, and (c) $NiFe_2O_4$nanoassemblies under 5 mT applied field and (d) their corresponding field-dependent magnetization at 300 K. Each sample shows almost no hysteresis and zero coercivity at room temperature.

2.5. Conclusion

The synthesis technique described in this chapter is a versatile process to develop mesoporous amine functionalized magnetic ferrite MFe_2O_4 (M = Co, Mn, Ni). The uniform and monodisperse structures are formed due to careful control of the reaction parameters. The nanospheres simultaneously show superparamagnetism and high saturation magnetisation because of iso-oriented attachment of small particles to give an assembled structure. Further, due to high surface area, presence of nanochannels and high density of surface amine groups routine bioconjugation as well as incorporation of drugs can be facilitated.

2.6. References

1. R. Hao, R. Xing, Z. Xu, Y. Hou, S. Gao and S. Sun, *Adv. Mater.*, 2010, **22**, 2729.
2. I. Brigger, C. Dubernet and P. Couvreur, *Adv.Drug Deliv. Rev.*, 2002, **54**, 631.
3. A. K. Gupta and M. Gupta, *Biomaterials.*, 2005, **26** 3995.
4. V. K. Varadan, L. F. Chen and J. Xie, *Nanosensors and Nanosystems., John Wiley & Sons Ltd.*, New York, 2008, 105.
5. A. K. Maaz, S. K. Hasanian and A. Celyan, *J. Magn. Magn. Mater.*, 2007, **308**, 289.
6. J. G. Lee, H. M. Lee, C. S. Kim and O. Young-Jei, *J. Magn. Magn. Mater.*, 1998, **177**, 900.
7. Y. Lee, J. Lee, C. J. Bae, J. G. Park, H. J. Noh, T. Hyeon, *Adv. Funct. Mater.*, 2005, **15**, 503.
8. R.V. Kumar, Y. Koltypin, X.N. Xu, Y. Yeshurun, A. Gedanken and I. Felner, *J. Appl. Phys.*, 2001, **89** 6324.
9. I. Bilecka, I. Djerdj and M. Neiderberger, *Chem. Commun.*, 2008, **7**, 886.
10. S. Sun and H. Zeng, *J. Am. Chem. Soc.*, 2002, **124**, 8204.
11. M. Yanez-Vilar, C. Sanchez-Andujar, J. Gomez-Aguirre, M. Mira and S. Senaris- Rodriguez Castro-Garcia, *J. Solid State Chem.*, 2009, **182**, 2685.
12. F. Caruso, R. Caruso and H. Mohwald, *Science.*,1998, **282**, 1111.
13. A. K. Boal, F. Ilhan and J. E. DeRouchy, *Nature*., 2000, **404**, 746.
14. S. M. Scholz, R. Vacassy and L. Lemaire, *Appl. Organomet. Chem*., 1998, **12**, 327.
15. A. Sukhanova, A.V. Baranov, D. Klinov, V. Oleinikov, K. Berwick, J.H.M. Cohen, M. Pluot and I. Nabiev, *Nanotechnology*., 2006, **17**, 4223.
16. Y. Chu, J. Hu, W. Yang, C. Wang and Z. Jin., *J. Phys. Chem.*, 2006, **110** 3135.
17. A. Ditsch, P. E. Laibinis, I. C. Wang and T. A. Hatton, *Langmuir.*, 2005, **21**, 6006.

18. C. Cannas, A. Ardu, A. Musinu, D. Peddis and G. Piccaluga, *Chem. Mater.*, 2008, **20**, 6364.
19. J. Ge, Y. Hu, M. Biasini, W.P. Beyermann and Y. Yin, *Angew. Chem. Int. Ed.*, 2007, **46**, 4342.
20. K. C. Barik, M. Aslam, P.V. Prasad, V. P. Dravid and D. Bahadur, *Magn. Mater.*, 2009, 321, 1529.
21. C. Cheng, Y. Wen, X. Xub and H. Gu, *J. Mater. Chem.*, 2009, **19**, 8782.
22. W. Hui, Q. W. Chen, Y. B. Sun, M. S. Wang, L. X. Sun and W. S. Yan, *Langmuir.*, 2010, **26**, 5957.
23. S. E. Skrabalak, B. J. Wiley, M. Kim, E.V. Formo and Y. Xia, *Nano Lett.*, 2008, **8**, 2077.
24. Y. Liu, W. Jiang, L. Xu, X. Yang and F. Li, *Mater. Lett.*, 2009, **63**, 2526.
25. R. L. Penn and J. F. Banfield, *Science*., 1998, **281**, 969.
26. J. F. Banfield, S. A. Welch, H. Zhang, T. T. Ebert and R. L. Penn, *Science*., 2000, **289**, 751.
27. R. L. Penn, G. O. Timothy, J. Strathmann, P. C. Searson, A. T. Stone, D. R. Veblen, *J. Phys. Chem.*, 2001, **105**, 2177.
28. S. Guo, D. Li, L. Zhang, J. Li and E. Wang, *Biomaterials.*, 2009, **30**, 1881.
29. S. Mohapatra, N. K. Pramanik, S. Mukherjee, S. K. Ghosh, P. Pramanik, *J. Mater. Sci.*, 2007, **42**, 7566.
30. K. H. Bae, Y. B. Kim, Y. Lee, J. Y. Hwang, H. W. Park and T. G. Park, *Bioconjugate Chem.*, 2010, **21**, 505.
31. Y. Liua, Y. Zhanga, J. D. Fenga, C. F. Lia, J. Shiab and R. Xiong, *J. Exp. Nanosci.*, 2009, **4**, 159.
32. Z. Zhou, Y. Zhang, Z. Wang, W. Wei, W. Tang, J. Shi and R. Xiong, *Appl. Surf. Sci.*, 2008, **254**, 6972.
33. W. J. Gammon, O. Kraftb, A.C. Reillya and B. C. Hollowayc, *Carbon*., 2003, **41**, 1917.

34. M. Das, D. Mishra, T. K. Maiti, A. Basak and P. Pramanik, *Nanotechnology.*, 2008, **19**, 415101.
35. X. Liu, Q. Hu, Z. Fang, Q. Wu and Q. Xie, *Langmuir*., 2009, **25**, 7244.
36. C.V. Mohan, M. Seeger, H. Kronmuller, P. Murugaraj, and J. Maier, *J. Magn. Magn. Mater.*, 1998, **183**, 348.
37. E. VeenaGopalan, K. A. Malini, S. Saravanan, D. Sakthi Kumar and M. R. Anantharaman, *J. Phys. D: Appl. Phys.*, 2008, **41**, 185005.
38. K. V. P. M. Shafi, A. Gedanken, R. Prozorov and J. Balogh, *Chem. Mater.*, 1998, **10**, 3445.
39. M. Rashad, *Mater. Sci. Eng.*, 2006, **127**, 123.
40. V. P. M. Kurikka, Y. K. Shafi, A. Gedanken, R. Prozorov, J. Balogh, J. Lendvai and I. Felner, *J. Phys. Chem*., 1999, **101**, 6409.
41. B. D. Cullity, *Addinson Wesley*, *New York*, 1972, 190.
42. L. Wang, J. Ren, Y. Wang, X. Liu and Y. Wang, *J. Alloys Compd.*, 2010, **490**, 656.
43. S. Gyergyek, D. Makovec, A. Kodre, I. Arcon, M. Jagodic and M. Drofenik, *J. Nanopart. Res.*, 2010, **12**, 1263.
44. B. Marrtinz, X. Obradors, L. I. Balcells, A. Rouanet and C. Monty, *Phys. Rev. Lett.*, 1998, **80**, 181.

Chapter-3

Synthesis and surface functionalization of monodisperse mesoporous cobalt ferrite nanoparticles for targeted delivery of antitumor drugs

3.1. Introduction

From last few years, numerous efforts have been devoted to develop a suitable magnetic nanocarriers for tumor diagnostic and therapy.[1,2] Generally, the nanocarrier used for biomedical applications should an inexpensive material, follows very simple methods to fabricate, spherical, narrow size distribution, biocompatible, good dispersion stability in physiological environment and have large surface area for maximal drug loading. Among the different types of functional nanostructures, superparamagnetic iron oxide nanoparticles (SPION) with appropriate surface chemistry have been widely used in several biomedical fields such as contrast enhancing agent in MRI, tissue repair, cell separation, hyperthermia treatment and an active agent in drug delivery.[3-5] Since its first use as a liver contrast agent in 1986,[6,7] many researchers have developed novel nanoparticulate systems with improved surface functionalization with biocompatibility, targeting ability and multifunctionality.[8,9] However, the use of other ferrites such as spinel ferrites or garnets with larger anisotropy may be envisioned for biomedical applications, as it could allow a significant improvement in material efficiency.[10-12] Besides to this, the use of spinel ferrites is more advantageous in therapeutic applications because magnetic property and Curie temperature (Tc) can be tuned by substitution with variable nonmagnetic cations.[13] More importantly, spinel cobalt ferrite forms such a magnetic system in which it is easy to control magnetic properties at the atomic level through chemical manipulation.[14-16] Cobalt ferrite has been proposed for biomedical applications since it is known to have large anisotropy compared to other oxide ferrites.[17] As the magnetic anisotropy is directly connected to hyperthermic efficiency,[18] the use of cobalt ferrite nanoparticles could introduce several benefits in therapeutic applications.[19] Recently Frachini and co-workers have developed bovine-serum albumin-cobalt ferrite based theranostic nanomedicine which would make a negative contrast agent in MRI and can be employed as heat mediators allowing enhanced hyperthermic effects even with the reduced magnetic field.[20]Scaberry and

coworkers have developed biocompatible glucuronic acid coated magnetic spinel cobalt ferrite nanoparticle-peptide conjugate to target and extract malignant ovarian cancer cells.[21] Napini and coworkers have also studied several cobalt ferrite based magneto liposome for controlled drug release in presence of alternate magnetic field.[22-23]

Due to the large anisotropic effect of cobalt ferrite, it can be used instead of iron oxide particles with appropriate physical characteristics and allowing the assembly of smaller biocompatible devices that are known to promote cellular uptake and to better avoid the reticuloendothelial system.[2] one important strategy to improve physicochemical characteristics of nanoparticles is surface coating. Proper surface coating such as organic polymers,[24] small coupling molecules,[25] or inorganic silica materials[26] allows ferrite nanoparticles to disperse homogeneously into the carrier fluid and drugs can be attached through the surface functional groups for therapeutic applications. Furthermore, the nanoparticles designed for controlled drug delivery should have an efficient mechanism for controlled release of the drug within the target cell. An emerging concept to improve the targeting capacity and drug releasing efficiency of nanoparticles is active targeting through folate receptor-mediated endocytosis.[27-28] It has been revealed that aggressive or undifferentiated tumors at an advanced stage such as ovarian, endometrial, colorectal, breast, lung, renal cell carcinomas, brain meta stages derived from epithelial cancers have an increased folate receptor density compared to normal tissues.[29-30] Also it has been reported that folic acid conjugated superparamagnetic iron oxide nanoparticles can efficiently show *in vitro* intracellular uptake by folate receptor overexpressed HeLa and B16 melanoma cells.[31]

Alternatively, Methotrexate (MTX) is an analogue of folic acid and inhibits the target enzyme, dihydrofolate reductase (DHFR). Methotrexate not only display the targeting role of folic acid but also it has the ability to treat many types of cancer cells that overexpress folate receptor on their surfaces.[32] Impairment of drug import

into cells and increase in drug export from cells may render cells resistant to MTX. MTX, when locally administered in a soluble form, is rapidly absorbed through capillaries into the circulatory system, which may also account for therapeutic failure in patients. Serious attempts have been made to propose new nanoparticle based formulations for retention of MTX within tumor cells for longer duration and alter its pharmacokinetic behavior. Methotrexate conjugated iron oxide nanoparticles was developed by Kohler *et al*. which act as contrast enhancing agent in MRI and as a drug carrier in controlled drug delivery, targeted at cancer diagnostics and therapeutics.[33] Recently Das *et al.* have successfully synthesized multifunctional nanoplatform, which serve as MRI contrast as well as the delivery of methotrexate.[34] They have also shown the controlled release of MTX through pH sensitive cleavage of the ester bond. However, a serious disadvantage of such methods is the multistep reaction for surface modification leading to the possibility of loss of magnetic property and other physical properties of nanoparticles due to the repeated exposure to the reaction conditions.

Keeping in mind the advantages of cobalt ferrite as the magnetic component and methotrexate as the therapeutic component we deem to develop a theranostic nanoparticle which can deliver methotrexate in its acid form. In additions to this a robust stimuli responsive attachment between the drug and the carrier would prevent the premature release of the drug before it reaches the target site. For this we hypothesize that amide bond would be an appropriate choice to bind MTX on cobalt ferrite. In addition to this extreme care must be taken to control the proportion of drug, maker molecule and fluorophore.

In this study, we have developed a facile synthetic route to prepare water soluble $–NH_2$ functionalized superparamagnetic $CoFe_2O_4$ nanoparticles with high surface area in one-pot by taking the advantages of thermal decomposition method. The solvents ethylene glycol and ethanolamine served as stabilizer and surface functionalizing agent, thus avoiding multistep synthesis for surface functionalization. We have loaded these $–NH_2$ functionalized particles with

anticancer drug methotrexate and a fluorescent marker RITC. The entire MTX conjugated $CoFe_2O_4$ nanoparticles have been characterized in terms of their structure, morphology, size, and magnetic property. The *in vitro* biocompatibility of $CoFe_2O_4$-MTX was investigated through MTT assay. The intracellular uptake efficiency was thoroughly investigated through fluorescent microscopy and flow cytommetry (FACS). The MTX release profile was investigated by mimicking the lysosomal conditions in presence of bovine protease. In addition to this, the effective loading and pH sensitive release behavior of another anticancer drug doxorubicin have also been demonstrated using synthesized $CoFe_2O_4$ nanospheres.

3.2. Experimental

Materials

Ethylene glycol, ethanolamine, sodium acetate, ferric chloride, cobalt chloride were procured from Merck, Germany. RITC, folic acid, bovine serum albumin, methotrexate (MTX) and doxorubicin (DOX) were purchased from Sigma-Aldrich. N-hydroxysuccinamide (NHS), ethyl-(N',N'-dimethylaminopropyl) carbodiimide hydrochloride (EDC), 4-(N, N dimethylamino) pyridine (DMAP) were procured from Spectrochem, India. MTT (3-[4,5-dimethylthiazol-2-yl]-2,5-diphenyltetrazolium bromide), paraformaldehyde, propidium iodide (PI), dimethylsulfoxide (DMSO), 4′,6-diamidino-2-phenylindole dihydrochloride (DAPI), Rodamin B isothiocyanate (RITC) and RNase A were purchased from Sigma Chemical Co. (St. Louis, MO, USA). Millipore water was used throughout the experiment.

Preparation of $CoFe_2O_4$-NH_2 nanoparticles

Amine functionalized superparamagnetic $CoFe_2O_4$ nanoparticles were prepared by thermal decomposition of $CoCl_2.6H_2O$ and $FeCl_3$ in ethylene glycol in presence of sodium acetate and ethanol amine (Fig.1). Briefly, anhydrous $FeCl_3$

(0.683 g, 4.2 mmol) and $CoCl_2.6H_2O$ (0.576 g, 2.1 mmol) were taken in 30 mL ethylene glycol and 0.5 gm of sodium acetate was added to it. The reddish black color solution thus obtained was stirred for 30 min at 80°C followed by addition of 15 mL of ethanol amine. The entire solution was allowed to reflux for 6h during which fine black colloidal particles appeared in the reaction mixture. Then it was cooled down to room temperature. The $CoFe_2O_4$ were recovered using a magnetic separator (DynaMag2, Invitrogen) washed with millipore water (5x5 mL) and dried in hot air oven at 80 °C for 2h.

Synthesis of folate decorated fluorescent magnetic carriers

The folic acid conjugation with amine functionalized cobalt ferrite NPs is shown in Fig. 3.1. 100 mg of amine functionalized $CoFe_2O_4$ nanoparticles were dispersed in 5mL of water. To a stirred solution of EDC (18 mg, 0.09 mmol) in 5 mL of H_2O, NHS (41 mg, 0.35 mmol) was added. To the resulting solution, alkaline solution of folic acid (13 mg, 0.031 mmol) in 5 mL of H_2O was added followed by addition of 100 mg amine functionalized $CoFe_2O_4$ nanoparticles dispersed in 5 mL H_2O. The entire solution was stirred in dark for 12h and the particles were separated magnetically, washed thoroughly with (3x5mL) millipore H_2O and dispersed in 5 mL H_2O ($CoFe_2O_4$-FA). To this dispersion RITC (100µg in 1mL DMSO/H_2O) was added. The resulting suspension was sonicated for 1h in dark. Particles were recovered by magnetic separation and washed thoroughly with millipore water ($CoFe_2O_4$-FA-RITC).

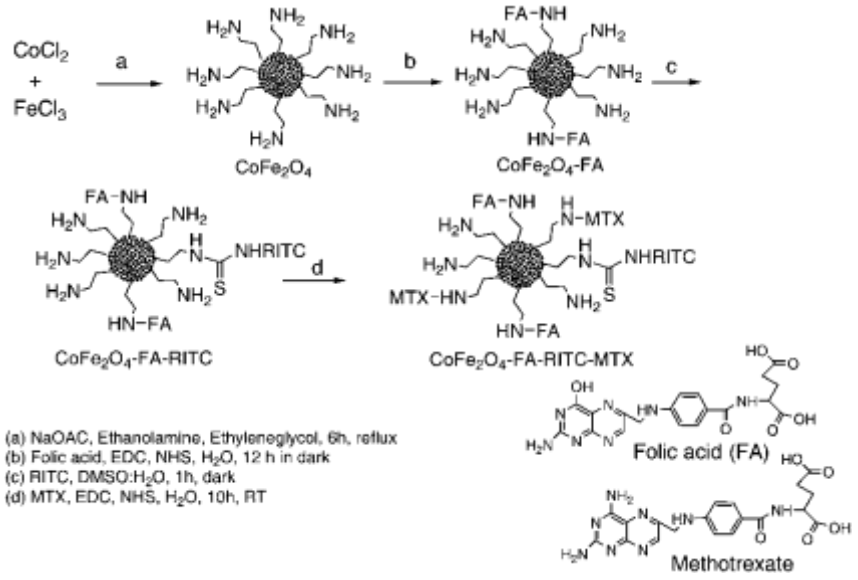

Fig. 3.1 Schematic representation for the synthesis and conjugation of folic acid and methotrexate to mesoporous cobalt ferrite nanoparticles.

Loading and release of MTX

In a 50 ml round bottom flask, EDC (0.018 g, 0.093 mmol) and NHS (41 mg, 0.35 mmol) were taken in 5 mL water. To this solution, slightly alkaline solution (pH 8) of methotrexate (63.6 mg, 0.14 mmol, molar ratio FA:MTX ≈ 1:5) in 5 mL H_2O was added and agitated for 2h in dark. Then 2 mL of aqueous dispersion of particles (0.1 mg/mL) was added and stirred in dark for 10 h at room temperature. Then the particles were recovered using magnetic separator, washed thoroughly with millipore water (5 x 5 mL) and suspended in phosphate buffer (pH 7.4) and used for *in vitro* studies ($CoFe_2O_4$-FA-RITC-MTX). Simultaneously another two sets of samples were also prepared, **1**) without conjugating RITC ($CoFe_2O_4$-FA-MTX), **2**) without conjugating FA and RITC ($CoFe_2O_4$-MTX) using the same procedure. In order to study MTX release behavior, 5 mL suspension of $CoFe_2O_4$-FA-RITC-MTX particles (0.1 mg/mL) was suspended in a solution containing 0.1 mg/ml protease from bovine pancreas (sigma) and 5 ml of PBS. The solution pH was adjusted to 3, 5 and 7.4 using 0.1 M HCl and NaOH. Following incubation for 8, 12, 24, 48 and 72 h the

nanoparticles suspensions were isolated and the MTX cleaved from nanoparticles was then quantified with UV spectroscopy (λ_{max} = 270 nm).

Loading and release of DOX

To load DOX, the amine functionalized magnetic nanoparticles were converted to acid terminated particles through ring opening reaction with succinic anhydride in the presence of DMAP (Fig. 3.2). For this purpose, 10 ml aqueous dispersion (0.1 mg/mL) of nanoparticles were washed thoroughly with millipore water and then dispersed in 5 mL of methanol. In a 100 mL round bottom flask, succinic anhydride (0.05g, 0.5 mmol) and DMAP (0.06g, 0.5 mmol) were taken in 15 mL methanol followed by addition of $CoFe_2O_4$ nanoparticles. The total mixture was refluxed for 24 h at 80ºC ($CoFe_2O_4$-FA-COOH). The particles were recovered, washed thoroughly with methanol (5x5mL), dried at 80ºC (5mL of aqueous solution containing NHS (41mg, 0.358 mmol) and EDC (18 mg, 0.0938 mmol) was taken in a 50 ml of round bottom flask and was kept in dark for 2 h. After that the aqueous solution of DOX (74 mg in 12 mL water, molar ratio FA:DOX≈1:5) was added to the above solution followed by addition of $CoFe_2O_4$-FA-COOH. The resulting suspension was stirred at room temperature for overnight and the particles ($CoFe_2O_4$-FA-DOX) were isolated magnetically. In order to study release behavior 5 ml suspension of $CoFe_2O_4$-FA-DOX particles (0.1 mg/ml) was suspended in a solution containing 0.1 mg/ml protease from bovine pancreas and 5ml of PBS (0.1 mg/ml). The solution pH was adjusted to 3, 5 and 7.4 using 0.1 M HCl and NaOH. Subsequent to incubation for 5, 10, 20, 25h, at 37 °C, the nanoparticles were isolated magnetically and the recovered DOX in the supernatant was quantified spectrophotometrically in UV spectrophotometer (λ_{max}= 255 nm).

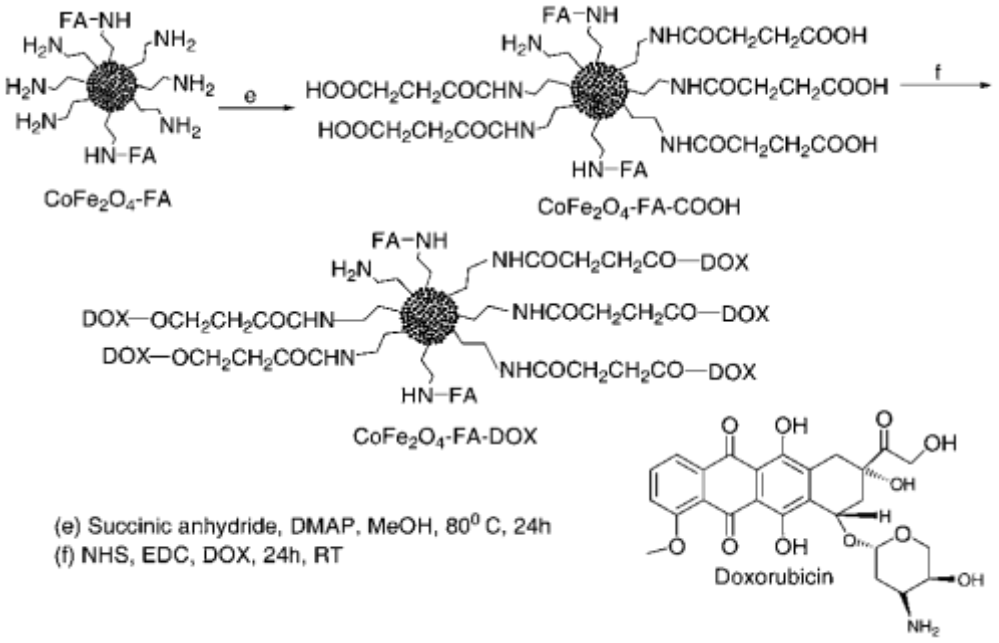

Fig. 3.2 Schematic representation for conjugation of doxorubicin on mesoporous cobalt ferrite nanoparticles.

3.3. Characterization

Phase purity

The identification of crystalline phase of cobalt ferrite particles was performed by an Expert Pro Phillips X-ray diffractometer. The morphology and microstructure were analysed by Scanning electron microscope (HITACHI COM-S-4200) and High resolution transmission electron microscopy (JEOL 3010, Japan) operated at 300 kV. The particles size from TEM micrographs were analysed using image J software.

Measurement of particle size, stability and zeta potential.

Hydrodynamic (HD) size of particle aggregates was measured by laser light scattering using a particle size analyzer (Nano ZS 90, Malvern). Measurement was performed at 90° angle in 0.01 M phosphate buffer varying pH 5 to 9. For all measurements the concentrations of particles were maintained at 66.67µg/ ml. Also the hydrodynamic sizes of particles were measured with respect to time at pH 7.4.

Surface chemistry

FTIR spectra of as prepared, MTX and DOX conjugated nanoparticles were obtained from a Thermo Nicolet Nexus FTIR model 870 spectrometer. Surface composition of MTX conjugated particles was obtained by analyzing XPS data using AlK_α excitation source in ESCA-2000 Multilab apparatus (VG microtech).

Cytotoxicity

Human cervical carcinoma (HeLa), cells were obtained from the National Centre for Cell Sciences (Pune, India), cultivated in minimal essential medium supplemented with 10% fetal calf serum, 100 units/mL penicillin, and 100 μg/mL streptomycin, 4 mM l-glutamine under 5% CO_2 and 95% humidified atmosphere at 37 °C. From 10^5 cells/ml cell suspension, 180 μl cell suspension was seeded at into each well of 96 wells tissue culture plates and incubated for 18 h followed by an addition of $CoFe_2O_4$ nanoparticle, $CoFe_2O_4$-MTX nanoparticle and $CoFe_2O_4$-FA-MTX nanoparticle at concentrations from 1 μg/ml to 20 μg/ml and were incubated for 72 h at 37°C in a humidified incubator (HERA cell) maintained with 5% CO_2. The cell proliferation was estimated by MTT assay.

Intracellular uptake study.

$CoFe_2O_4$-FA-RITC-MTX nanoparticles were incubated for 0, 30, 60, 90 and 120 min with HeLa cells at a concentration of 5mg /ml. Cells were then fixed with 4% paraformaldehyde after the incubation period for 15 min and stained with DAPI (1mg/mL) for 5 min at 37 °C. Then cells were washed with PBS and examined under fluorescence microscopy (Olympus IX 70).

Cell cycle analysis

Cell cycle analysis by flow cytometry with PI staining was performed according to Maiti et al with minor modifications.[35] HeLa cells were incubated for 24h in presence of increasing concentration of $CoFe_2O_4$-FA-MTX nanoparticle (1-

10μg/mL) at 37 °C in CO_2 incubator. The cells were then harvested with trypsinisation and fixed with chilled 70% ethanol and stored at −20 °C. Then, the cells were washed with ice cold PBS (10 mM, pH 7.4) and incubated with 20 μl DNAase-free RNase (10 mg/mL) and 20 μl of DNA intercalating dye PI (1 mg/mL) at 37 °C for 1 h in dark. The distribution of cells in the different cell-cycle phases was analyzed from the DNA histogram using a Becton–Dickinson FACS Calibur flow cytometer and analysed with Flow Jo software.

DAPI Staining for nuclear morphology study

To study the nuclear morphology of HeLa cells DAPI staining was performed according to reported procedure.[35] HeLa cells treated PBS or with $CoFe_2O_4$-FA-MTX nanoparticle *in vitro* for 24 h. The cells were fixed with 3.7% formaldehyde for 15 min, permeabilized with 0.1% Triton X-100 and stained with 1 μg /ml DAPI for 5 min. The cells were then washed with PBS and examined under fluorescence microscopy (Olympus IX 70).

3.4. Results and Discussion

XRD pattern

In the XRD pattern of $CoFe_2O_4$ (Fig. 3.3), all *d* values correspond to that of inverse spinel $CoFe_2O_4$ (03-0864). The broadening of peaks corresponds to nanocrystalline nature of the sample. The crystallite size was calculated using Debye-Scherer's equation taking broadening of each peak into account and was found to be 5.2 nm. The lattice parameter was calculated from reflections of [400] plane as 8.36 Å which is very close to that of inverse spinel $CoFe_2O_4$.

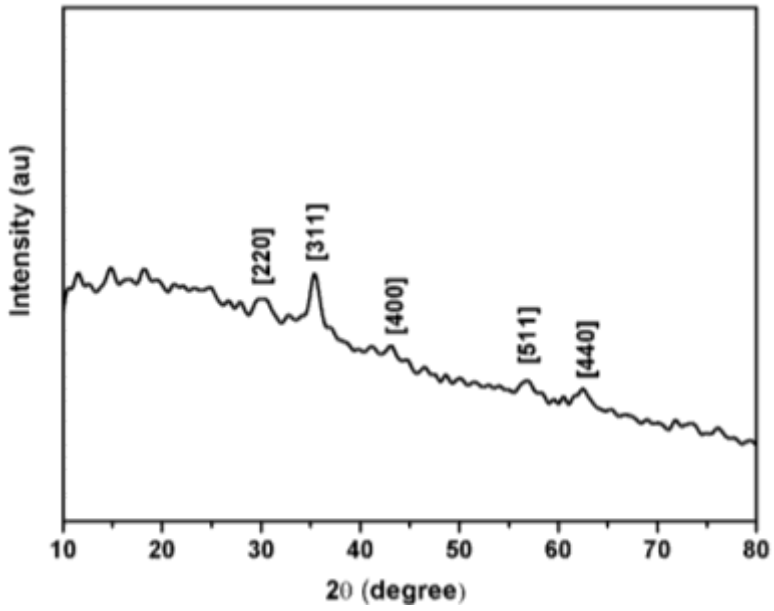

Fig. 3.3 XRD pattern of mesoporous $CoFe_2O_4$ nanoparticles.

Morphology

The SEM image (Fig. 3.4a) of $CoFe_2O_4$-NH_2 indicates that the nanoparticles are spherical in nature and are almost monodisperse. Fig. 3.4(c) is the representive TEM micrograph of $CoFe_2O_4$ in PBS. It is very clear from the image that each particle is a spherical assembly of ultrafine ferrite particles. These spherical nanoassemblies are of size 35-40 nm and are discrete, well defined and porous in nature. Fig. 3.4(c) showing image at higher magnification indicates that each sphere is an assembly of primary nanocrystals of 4-5 nm and worm like pores of diameter 2-3 nm. The high resolution TEM of a single aggregate (Fig. 3.4d) shows lattice planes. The inter planner distance *d* is calculated from the image as 2.97 Å which corresponds to reflection of [220] plane. This result is in line with the observations reported by Cannas et al. for the synthesis of nanoporous $CoFe_2O_4$ by surfactant assisted route.[38] The individual planes identified from the SAED pattern (Fig. 3.4e) correlate with XRD pattern. Most important observation is that each spherical assembly is well separated from the other which was not observed in earlier methods for synthesis of mesoporous magnetic nanoparticles.[39,40] Here it may be noteworthy

that dispersion state of magnetic nanoparticles is the most important factor as far as the magnetic property is concentrated.

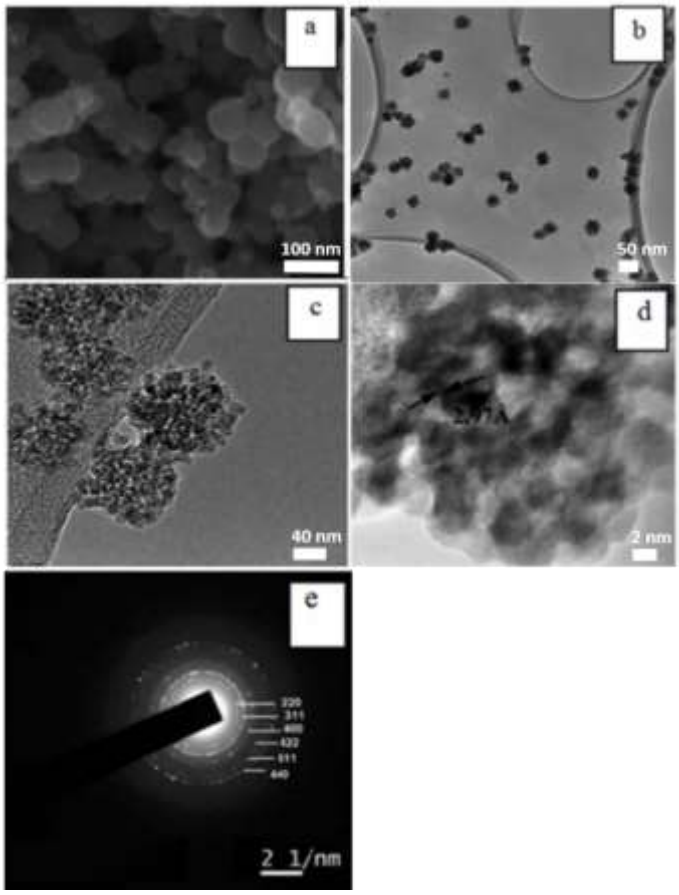

Fig. 3.4 (a) SEM image, (b, c) TEM images, (d) HRTEM (e) SAED pattern of $CoFe_2O_4$ nanoparticles.

Magnetic measurements

Field dependent magnetization at room temperature (300K) was measured and it was found that the magnetization raised rapidly as the applied field increases upto 1T and reached at a saturation point 2T, shows no hysteresis representing superparamagnetic nature of the nanoparticles (Fig. 3.5). The saturation magnetization of cobalt ferrite was found to be 59.4 e.m.u./g corresponding to its bulk

counterpart 71.2 e.m.u/g. This decrease in magnetization (Ms) value corresponds to decrease in particle size[41] due to surface protection by ethanol amine.

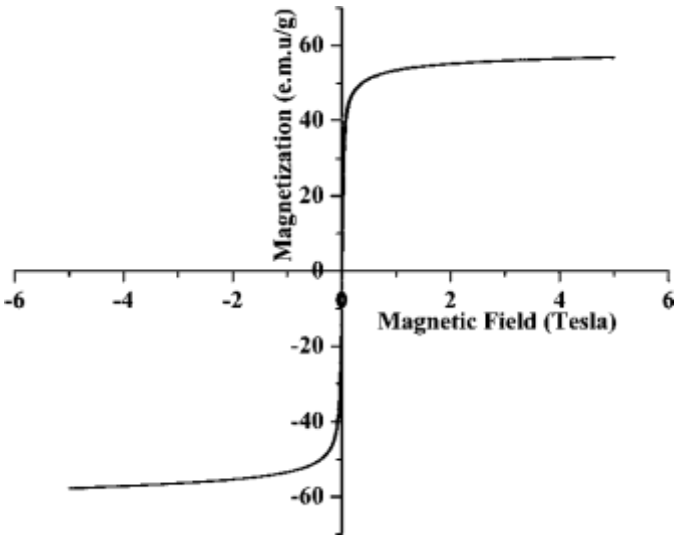

Fig. 3.5 Field dependent magnetization curve of mesoporous $CoFe_2O_4$nanoparticles.

Hydrodynamic and zeta potential measurement

An investigation on hydrodynamic size of fluorescent magnetic carrier $CoFe_2O_4$-FA-RITC and drug conjugates $CoFe_2O_4$-FA-RITC-MTX and $CoFe_2O_4$-FA-DOX was carried out through dynamic light scattering (Fig. 3.6) in PBS. Product $CoFe_2O_4$-FA-RITC-MTX shows presence of stable non aggregated particles with hydrodynamic size 61 nm, PDI< 0.2 and surface charge -27.3 mV. The stability of MTX-conjugated particles investigated by measuring hydrodynamic size against time shows that there is almost no change of hydrodynamic size and zetapotential even after several months. This observation implies that such stable drug conjugates can be circulated in blood stream for a long period minimizing the rapid clearance of particles by macrophages.

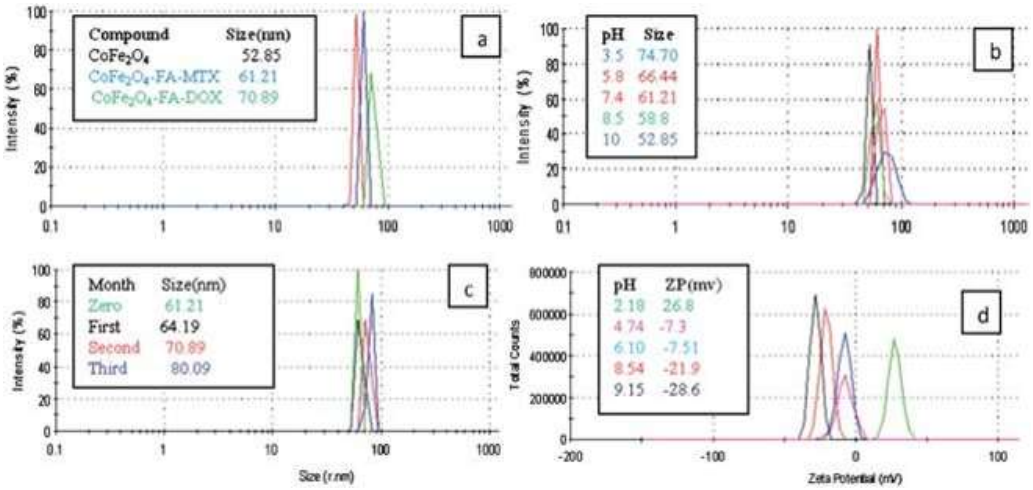

Fig. 3.6 .(a) Change in HD size with drug conjugation, Variation of HD size of $CoFe_2O_4$-FA-MTX conjugate nanoparticles (b) with pH, (c) with time. (d) Change in zeta potential with pH.

Again the Fig. 3.7 shows the surface charge of as synthesized cobalt ferrite nanoparticles and after modification with succinic anhydride. After modification with succinic anhydride the surface charge becomes -35.2 mV at pH 11 due to incorporation of –COOH groups. Similarly the $CoFe_2O_4$-FA-DOX also shows stable particles with hydrodynamic size 72 nm and also these particles are highly stable in aqueous medium, since there is almost all no significant change of hydrodynamic size upto three months (Fig. 3.8).

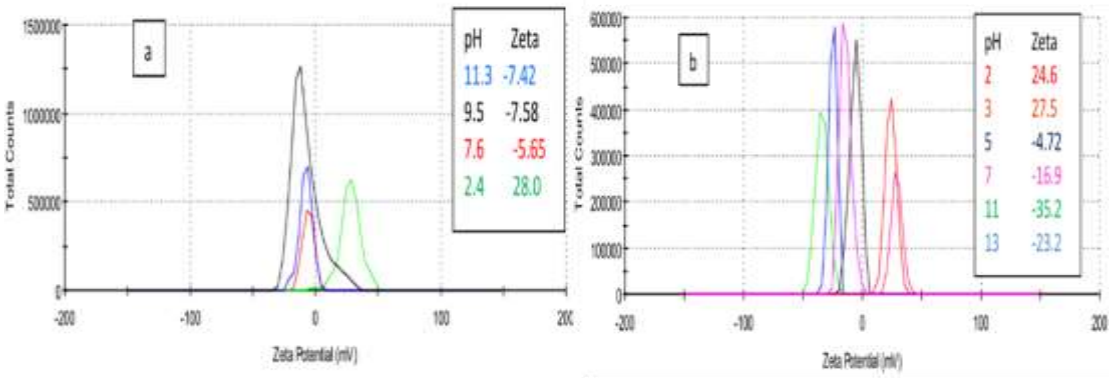

Fig. 3.7 Change in zeta potential with respect to pH (a) as synthesized CoFe2O4 nanoparticles (b) after treated with succinic anhydride.

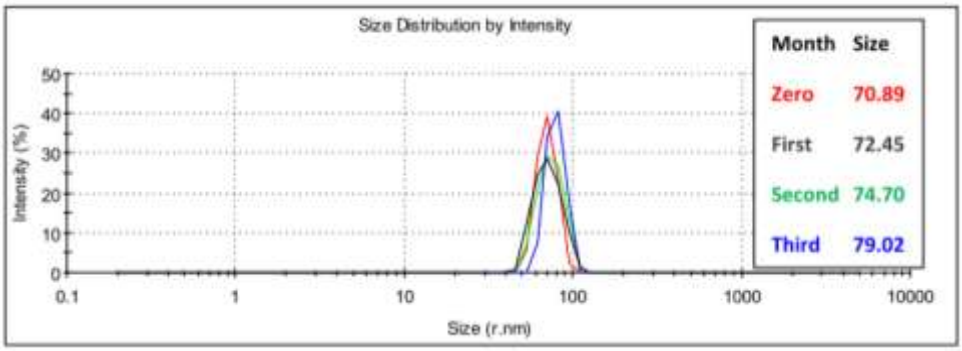

Fig. 3.8 Change in HD size of DOX loaded particles with time.

FTIR spectra

The FTIR spectrum of the MTX conjugated particles ($CoFe_2O_4$-FA-MTX) shows strong absorption at 500-600 cm^{-1} characteristic vibration of M-O in the ferrite lattice (Fig. 3.9). In addition to this, the intensification of methylene signature at 2935 and 2854 cm^{-1} along with C=O stretching at 1630 and 1546 cm^{-1} indicates that MTX has been conjugated to $–NH_2$ terminated particles through –NHCO linkage. Similarly the successful attachment of DOX was also established using FTIR.

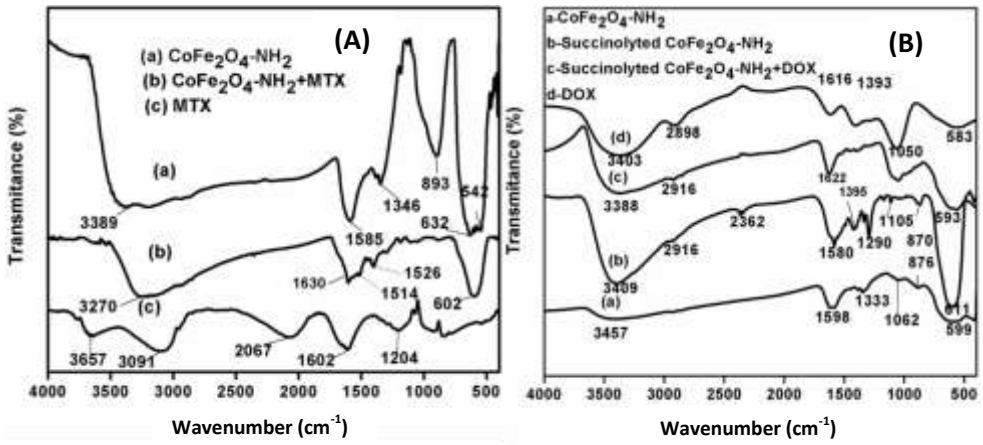

Fig. 3.9 FTIR spectra of (A)$CoFe_2O_4$-NH_2, $CoFe_2O_4$-NH_2-MTX and MTX and (B) $CoFe_2O_4$- NH_2, succinylated $CoFe_2O_4$- NH_2, succinylated $CoFe_2O_4$- NH_2-DOX and DOX.

XPS analysis

X-ray photoelectron spectra were further used to validate the successful conjugation of MTX on amine functionalized mesoporous magnetic nanoparticles. Fig. 3.10 shows high resolution XPS scan of MTX conjugated amine functionalized $CoFe_2O_4$ nanoparticles. The C1s peak corresponding to reference shows a shift 2eV to higher binding energy and hence taking reference shift to consideration all other binding energies are to be evaluated.

In high resolution scan C1s region shows four peaks centred at 286.9, 288.3, 289.6 and 291.99 eV corresponding to C-C, C-O, -NHCO- and COOH carbons. The O1s peak can be deconvoluted into 3 peaks centred at 532.09, 533.7 and 535.25 eV corresponding oxygen atoms present in M-O, C-O, COOH and -NHCO respectively. In as prepared $CoFe_2O_4$ nanoparticles, the N1s binding energy appeared at 398.7 eV which is close to N present in primary amine (Fig. 3.10), whereas in

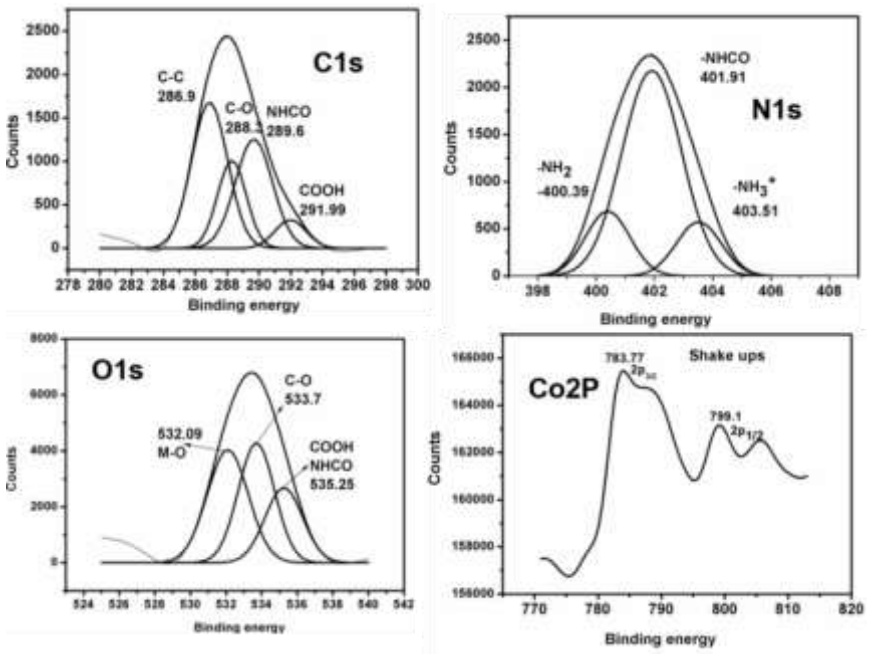

Fig. 3.10 XPS spectrum of product $CoFe_2O_4$-FA-MTX conjugate nanoparticles. High resolution scan of C1s, O1s, N1s and Co2p.

$CoFe_2O_4$-FA-MTX conjugated particles the N1s binding energy shows two additions peaks present at 401.91 and 403.51 eV corresponding to the –NHCO and NH_3^+ groups.[42] Also intensity of N1s peak was significantly increased after conjugation with MTX. $Co2p_{3/2}$ and $Co2p_{1/2}$ electrons show binding energy at 779 and 784 eV associated with corresponding shake ups at 785 and 801 eV.[43] Fe2p region shows two peaks at 711.5 and 725 eV which is consistent with Fe2p binding energy for $CoFe_2O_4$ nanoparticles.

Nitrogen adsorption-desorption study

Nitrogen sorption experiment was conducted to further investigate the porous nature of ferrite nanoparticles. Fig. 3.11 represents the nitrogen adsorption-desorption isotherms and BJH pore size distribution curves (inset) of $CoFe_2O_4$. The isotherms are identified as type IV, which is characteristic of mesopores. It is notable that besides mesopores formed by aggregations spherical particles, the BJH pore size distribution clearly indicates mesopores centred at 4-5 nm formed among the ultrafine nanoparticles within the aggregate which is in accordance with the TEM result.

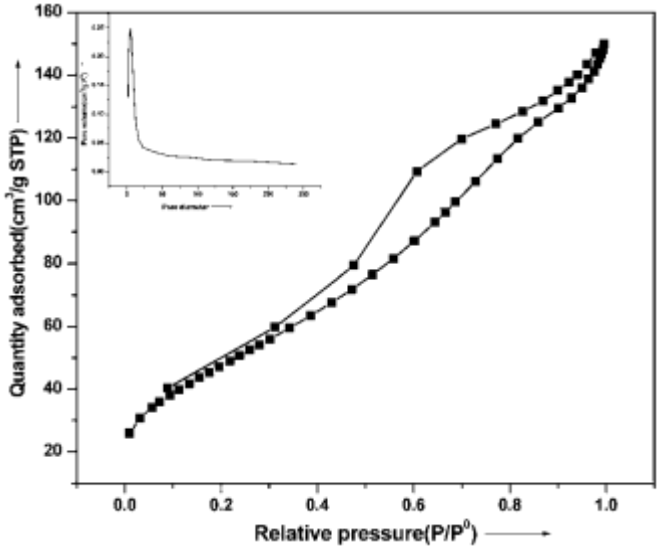

Fig. 3.11 Nitrogen adsorption-desorption isotherm and the corresponding pore size distribution of as synthesized $CoFe_2O_4$nanoparticles.

The BET surface area of the $CoFe_2O_4$ powder was calculated to be 210 m^2/g. To our knowledge, surface area values for porous magnetic oxide synthesized by various other synthetic methods[39,40] have not exceeded 150 m^2/g. Hence in the present solvochemical route the surface of magnetic oxides can be significantly increased and it would be particularly beneficial in magnetic separation and drug delivery.

Formation mechanism and compositions of magnetic nanocarriers

Formation of magnetic particles can be explained according to well-known polyol method of synthesis.[44] The formation of such nanoassemblies may be dependent on the collective behavior of nanoparticles and intermolecular forces existing between them.[40] The number of $–NH_2$, FA, MTX, RITC and DOX present on each spherical assembly was determined using UV-visible spectroscopy following the procedures reported elsewhere,[45,46] and it was found that each porous particle of 40 nm size contains approximately 490 $–NH_2$ groups and particle $CoFe_2O_4$-FA-RITC-MTX contains 280 MTX molecules.

pH dependent drug-release

In vitro drug release experiments were carried out with MTX and DOX conjugated nanoparticles in two separate batches. To simulate lysosomal condition, the nanoparticles were incubated with bovine protease in pH (3, 5, 7.4). It was well established that protease found in the lysosomal compartment is capable of hydrolyzing amide bond releasing drug molecule to the cytoplasm. Both MTX and DOX showed typical release profiles. MTX showed rapid release rates from the beginning followed by a sustained release pattern (Fig. 3.12). This release behavior is consistent with previously reported literature.[33,34,50] But in case of DOX slow release rates were observed from the beginning. The overall release rates were higher in lower pH (3, 5) and very less release was observed in physiological pH. This is because the drugs have been covalently grafted through an amide bonds.

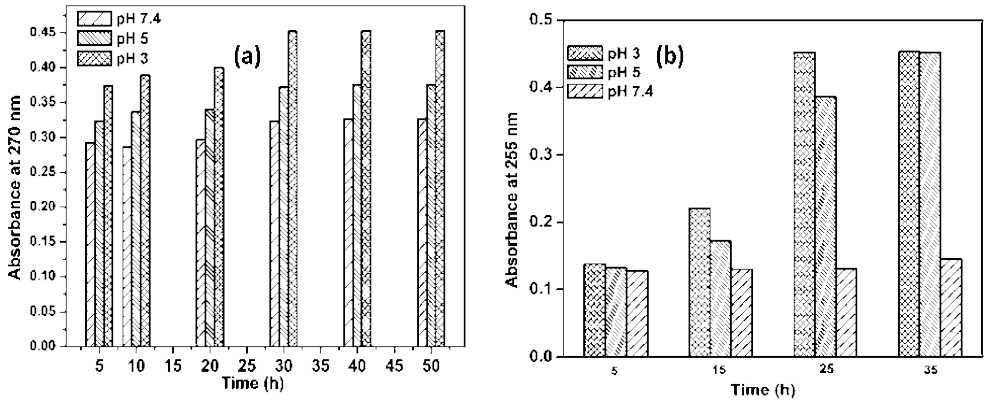

Fig. 3.12 pH dependent drug-release behaviours of (a) $CoFe_2O_4$-FA- MTX and (b) $CoFe_2O_4$-FA-DOX. The highest absorbance was observed at pH 3 in both cases, where almost no release was observed at physiological pH.

The cleavage of amide bond is controlled by pH and the concentration of active protease. This pH sensitive release behavior is attributed to the sensitivity of amide bond cleavage to pH and effect of pH on activity of protease.[50]

This observation suggests that the functionalized magnetic carriers containing substantial amount of antitumor drugs will release more drugs in acidic tumor sites rather than normal tissues. Furthermore, when these particles will be internalized through folate receptor-mediated endocytosis the release behavior will be further accelerated in acidic lysosome of cancer cells.

Calculation of drug loading capacity

The drug loading capacity was calculated as per the following method. First, NH_2/-COOH functionalized particles were conjugated with MTX/DOX as described in the experimental section and then separated from the aqueous suspension medium using magnetic separator (Invitrogen). The obtained drug-loaded $CoFe_2O_4$ nanoparticles were incubated at 60 °C invacuum overnight and were weighted. Drug concentration in supernatant was analyzed by the ultraviolet absorption (λ_{MTX} = 270 nm, λ_{DOX} = 255 nm), with reference to a calibration curve on a UV-Vis-NIR spectrophotometer. The measurements were performed in triplicate. Drug-loading content and encapsulation efficiency were obtained by eqs 1 and 2, respectively.

Doxorubicin

$$\text{Drug loading content (\%)} = \frac{\text{Weight of the drug in nanoparticles}}{\text{Weight of the nanoparticles}} \times 100$$

$$= \frac{0.00944}{0.0697} \times 100$$

$$= 13.54\% \text{ ---------- (1)}$$

$$\text{Encapsulation efficiency (\%)} = \frac{\text{Weight of the drug in nanoparticles}}{\text{Weight of the feeding drug}} \times 100$$

$$= \frac{0.00944}{0.0118} \times 100$$

$$= 80\% \text{ ---------- (2)}$$

Methotrexate

Similarly in case of methotrexate drug loading content (%) = 13.8 %

Encapsulation efficiency = 80 %

Cytotoxicity

HeLa cells are reported to express folate receptor and are studied as model *in vitro* systems for folate mediated targeting.[47] Here we investigated the effect of $CoFe_2O_4$ nanoparticles, $CoFe_2O_4$-MTX nanoparticles (Particle without FA) and $CoFe_2O_4$-MTX-FA nanoparticle on the proliferation of HeLa cells in vitro.

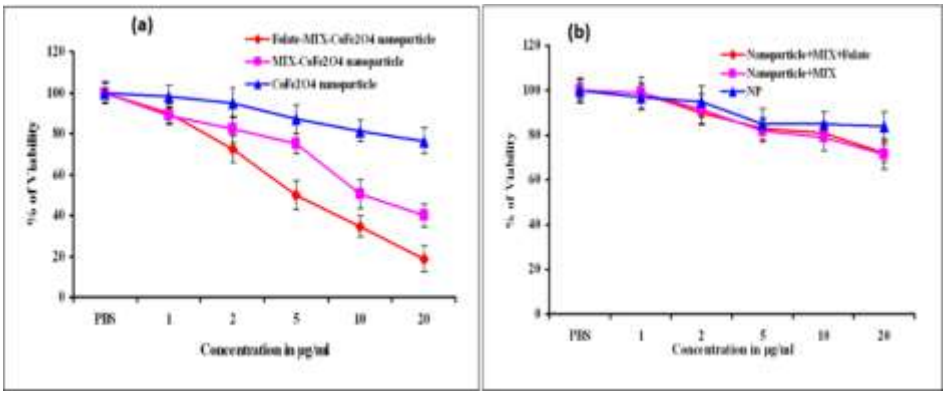

Fig. 3.13 Cytotoxicity assay of nanoparticles on (a) Hela and (b) NIH/3T3 cells. Cells were treated with different concentration of nanoparticles for 72 h and cell viability measured by MTT assay.

It was observed that $CoFe_2O_4$ nanoparticle did not induce any significant change in the proliferation in both HeLa and 3T3 cells with concentration up to 20 ug/mL with respect to the control (Fig. 3.13), suggesting an absence of toxicity of the $CoFe_2O_4$ nanoparticle. Subsequently the proliferation of HeLa cells reduced significantly in presence of $CoFe_2O_4$-MTX nanoparticles and at a dose of 10 μg/ml, the cell proliferation was uninhibited by 50% (IC_{50} value). This is possibly attributable to the affinity of MTX towards folate receptor owing to its structural similarity with folic acid, which results in higher intake of $CoFe_2O_4$-MTX particles as compared to $CoFe_2O_4$ nanoparticle. Whereas in case of 3T3 cells, there was only 20% reduction in cell proliferation which may be due to less availability of folate receptors on cell surface. However, the proliferation of HeLa cells reduced drastically in a dose dependent manner in presence of 5 ug/ml $CoFe_2O_4$-MTX-FA nanoparticles and its IC_{50} was 5 ug/mL. In contrast, there was no such change between $CoFe_2O_4$-MTX and $CoFe_2O_4$-MTX-FA was observed in 3T3 cells. This observation is attributed to the active uptake of nanoparticles in a folate receptor mediated endocytosis that interfered with the cell proliferation, which ultimately results in the target specific delivery of MTX to HeLa cells (Fig. 3.13).

Uptake study

We further investigated whether the resulting reduction of proliferation is due to the uptake of $CoFe_2O_4$-MTX-FA nanoparticles. In previous study we observed the folate receptor mediated uptake of iron oxide nanoparticles to HeLa cells.[25]Hence we performed fluorescence microscopy with $CoFe_2O_4$-FA-RITC-MTX nanoparticles to study its uptake by HeLa cells in a time dependent manner and DAPI was used as a nuclear contrast dye to appreciate the localization. HeLa cells were incubated with 5μg/ml of $CoFe_2O_4$-FA-RITC-MTX nanoparticles for 0, 30, 60, 90 and 120 min. The

uptake of $CoFe_2O_4$-FA-RITC-MTX nanoparticles was evident by 30 min and the internalization increased with time (Fig. 3.14). The RITC signal from the $CoFe_2O_4$-FA-RITC-MTX nanoparticle progressively increased in the cytoplasm surrounding the nuclear region. It suggests that nanoparticles are selectively targeted to the cells through the folate receptor mediated endocytosis and localized into the cytoplasm. Here the uniform distribution of the $CoFe_2O_4$-FA-RITC-MTX nanoparticles in the HeLa cells is because of their stable dispersion in the culture media. To confirm the receptor specificity of the $CoFe_2O_4$-FA-RITC-MTX nanoparticles the uptake as well as cell viability data of HeLa cells were also compared with folate receptor-negative NIH/$3T_3$ cells.

In the case of HeLa cells nanoparticles uptake as well anti-proliferation effect was much greater in comparison to NIH/$3T_3$ cells. Here the uniform distribution of $CoFe_2O_4$-FA-RITC-MTX nanoparticle in the HeLa cells is because of its stable dispersion in the culture media.

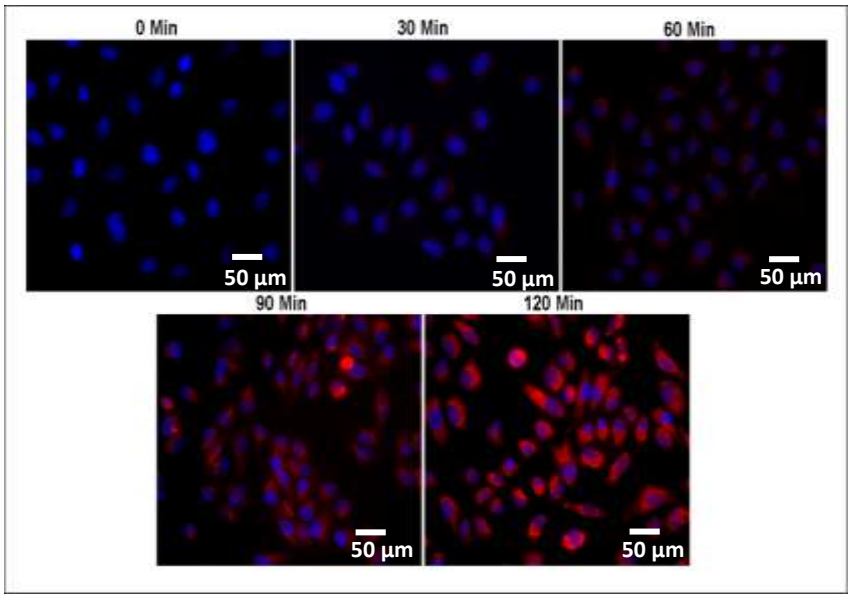

Fig. 3.14 Uptake study of nanoparticle in HeLa cells and using florescence microscopy. Cells were incubated with $CoFe_2O_4$-FA-RITC-MTX nanoparticles for different time intervals and observed under florescence microscope (200X)

Flowcytometric analysis

A quantitative evaluation of $CoFe_2O_4$-MTX-FA nanoparticle-mediated cell death was carried out through cell cycle analysis using the standard propidium iodide (PI) staining flow cytometry. Fig. 3.15 shows decrease in cells in the G0/G1 phase with increase in cell concomitants in the S phase indicating an arrest of the cell cycle in the S phase. The S phase distribution of cells increased up to 56% at 5µg/ml as compared 17% in the control cells whereas the G0/G1 phase decreased from 62% in control to 30% in the 5µg/ml treated cells. This result comes in hand with the known property of MTX to arrest cell cycle in the early S phase.[48] Additionally, MTX is also known to induce apoptosis in cancer cells.[49]

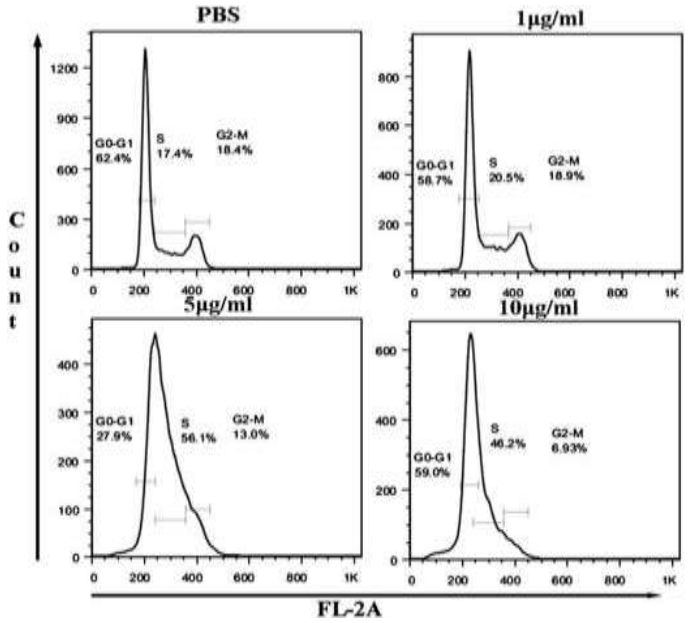

Fig. 3.15 Flowcytometric analysis of cell cycle phase distribution in HeLa cells. HeLa cells treated with (A) PBS, (B) 1 µg ml^{-1}, (C) 5 µg ml^{-1}, and (D) 10 µg ml^{-1} of $CoFe_2O_4$-FA- MTX nanoparticles for 24 h and the percentage of DNA content was determined by FACS calibour (BD) using Flow Jo software after the cells were labeled with PI preceding RNAase treatment.

Therefore we intended to study whether the targeted delivery of MTX in a folate receptor mediated method could result in the similar cell fate. Hence we

investigated the nuclear fragmentation which is a hallmark of apoptosis with the cells treated with MTX loaded particles. With increasing dose of the $CoFe_2O_4$-MTX-FA nanoparticles an increase in the formation of fragmented nuclei containing condensed nuclear material was observed in fluorescence microscopy after nuclear staining with DAPI.

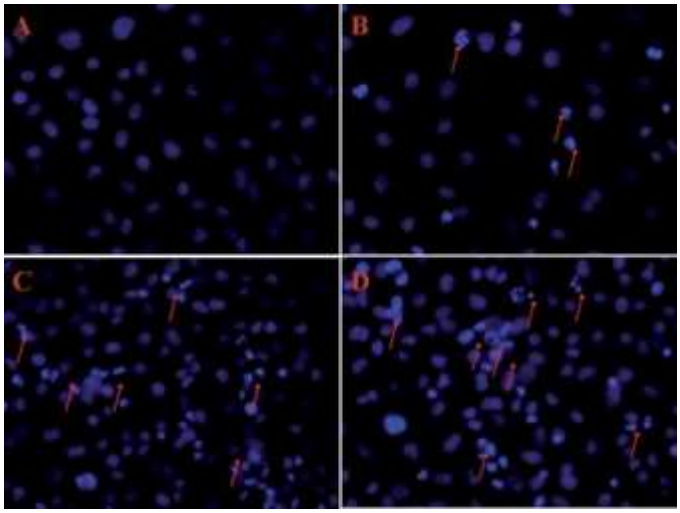

Fig. 3.16 DAPI Fluorescence (200X) images of HeLa cells incubated with(A) PBS, (B) 1, (C) 5, and (D) 10 μg ml^{-1} of $CoFe_2O_4$-FA-MTX for 24 h.The arrows represent nuclei with hallmark apoptotic features such as nuclear condensation, fragmentation, and formation of apoptotic bodies.

3.5. Conclusion

This work demonstrates a simple method to produce bio-functionalized, highly water-soluble, monodisperse, mesoporous, $CoFe_2O_4$ nanoassemblies with diameter 35-40 nm. The synthesis method is cost-effective, easy to scale up and reproducible. The presence of high density of surface amine groups and large surface area of the particles facilitate incorporation of substantial amount of anticancer drugs within its porous network. The nanoparticle modified with folic acid was effectively targeted to cancer cells thereby causing the optimal delivery of methotrexate and resulted in the cell death following the induction of apoptosis. In a nutshell, a nanotheranostic

reagent has been developed which combines superparamagnetic, receptor-targeting capacity, optical imaging and pH sensitive drug release behavior into one system.

3.6. References

1. R. Hao, R. Xing, Z. Xu, Y. Hou, S. Gao and S. Sun, *Adv. Mater*., 2010, **22**, 2729.
2. I. Brigger, C. Dubernet and P. Couvreur, *Adv. Drug Delivery Rev*., 2002, **54**, 631.
3. A. K. Gupta and M. Gupta, *Biomaterials*, 2005, **26**, 3992.
4. A. Y. Louie, M. M. Huber, E. T. Ahrens, U. Rothbacher, R. Moats and R. E. Jacobs, *Nat. Biotechnol*., 2000, **18**, 321.
5. J. M. Perez, F. J. Simone, A. Tsourkas, L. Josephson and R. Weissleder, *Nano Lett*., 2004, **4**, 119.
6. M. H. MendocaDiyas, *Magn. Reson. Med*., 1986, **3**, 328.
7. R. C. Semelka and T. K. G. Helmberger, *Radiology*, 2001, **218**, 27.
8. J. Kim, Y. Piao and T. Heyon, *Chem. Soc. Rev*., 2009, **38**, 372.
9. H. B. Na, I. C. Song and T. Heyon, *Adv. Mater*., 2009, **21**, 2133.
10. Z. Beji, A. Hanini, L. S. Smiri, J. Gavard, K. Kacem, F. Villain, J. M. Gren_eche, F. Chau and S. Ammar, *Chem. Mater*., 2010, **22**, 5420.
11. H. Yang, C. Zhang, X. Shi, H. Hu, X. Du, Y. Fang, Y. Ma, H. Wu and S. Yang, *Biomaterials*, 2010, **31**, 3367.
12. J. Giri, P. Pradhan, V. Somani, H. Chelawat, S. Chhatre, Rinti Banerjee and D. Bahadur, J. Magn. *Magn. Mater*., 2008, **320**, 724.
13. S. Mornet, S. Vasseur, F. Grasset and E. Duguet, *J. Mater. Chem.*, 2004, **14**, 2161.
14. S. Kuckelhaus, S. C. Reis, M. F. Carneiro, A. C. Tedesco, D. M. Oliveira, E. C. D. Lima, P. C. Morais, R. B. Azevedo and Z. G. M. Lacava, *J. Magn. Magn. Mater*., 2004, **272**,2402.
15. C. Cannas, A. Musinu, G. Piccaluga, D. Fiorani and D. Peddis, *Chem. Mater*., 2006, **18**, 3835.
16. K. V. P. M. Shafi, A. Gedanken, R. Prozorov and J. Balogh, *Chem. Mater*., 1998, **10**, 3445.

17. L. D. Tung, V. L. Kolesnichenko, D. Caruntu, N. H. Chou, C. J. O'Connor and L. Spinu, *J. Appl. Phys*., 2003, **93**, 7486.
18. R. E. Rosensweig, J. Magn. *Magn. Mater*., 2002, **252**, 370.
19. J. P. Fortin, C. Wilhelm, J. Servais, C. Menager, J. C. Bacri and F. Gazeau, *J. Am. Chem. Soc*., 2007, **129**, 2628.
20. M. C. Franchini, G. Baldi, D. Bonacchi, D. Gentili, G. Giudetti, A. Lascialfari, M. Corti, P. Marmorato, J. Ponti, E. Micotti, U. Guerrini, L. Sironi, P. Gelosa, C. Ravagli and A. Ricci, *Small*, 2010, **6**, 366.
21. K. E. Scarberry, E. B. Dickerson, J. F. McDonald and Z. J. Zhang, *J. Am. Chem. Soc*., 2008, **130**, 10258.
22. S. Nappini, F. B. Bombelli, M. Bonini, B. Norden and P. Baglioni, *Soft Matter*, 2010, **6**, 154.
23. S. Nappini, M. Bonini, F. B. Bombelli, F. Pineider, C. Sangregorio and B. Norden, *Soft Matter*, 2011, **7**, 1025.
24. J. J. Lin, J. S. Chen, S. J. Huang, J. H. Ko, Y. M. Wang and T. L. Chen, *Biomaterials*, 2009, **30**, 5114.
25. S. Mohapatra, S. Mallick, T. K. Maiti, S. K. Ghosh and P. Pramanik, *Nanotechnology*, 2007, **18**, 385102.
26. Y. H. Lien and T. M. Wu, *J. Colloid Interface Sci*., 2008, **326**, 517.
27. S. A. Kularatne and P. S. Low, *Methods Mol. Biol*., 2010, **624**, 249.
28. A. R. Hilgenbrink and S. Philip, *J. Pharm. Sci*., 2005, **94**, 2135.
29. J. Sudimack and R. J. Lee, *Adv. Drug Delivery Rev*., 2000, **41**, 147. S. J. Duthie, *Nutrition*, 2001, **17**, 736.
30. S. J. Duthie, *Nutrition.*, 2001, **17**, 736.
31. Y. H. Chen, C. Y. Tsai, P. Y. Huang, M. Y. Chang, P. C. Cheng, C. H. Chou, D. H. Chen, C. R. Wang, A. L. Shiau and C. L. Wu, *Mol. Pharmaceutics*, 2007, **4**, 713.
32. N. Kohler, C. Sun, A. Fichtenholtz, J. Gunn, C. Fang and M. Zhang, *Small*, 2006, **2**, 785.

33. N. Kohler, C. Sun, J. Wang and M. Zhang, *Langmuir*, 2005, **21**, 8858.
34. M. Das, D. Mishra, P. Dhak, S. Gupta, T. K. Maiti, A. Basak and P. Pramanik, *Small*, 2009, **5**, 2883.
35. S. Maiti, S. K. Bhutia, S. K. Mallick, A. Kumar, N. Khargi and T. K. Maiti, *Environ. Toxicol. Pharmacol*., 2008, **26**, 187.
36. S. Wang, J. Luo, D. A. Lantrip, D. J. Waters, C. J. Mathias, M. A. Green, P. L. Fuchs and P. S. Low, *Bioconjugate Chem*., 1997, **8**, 673.
37. P. S. Low, W. A. Henne and D. D. Doorneweerd, *Acc. Chem. Res*., 2008, **41**, 120.
38. C. Cannas, A. Ardu, A. Musinu, D. Peddis and G. Piccaluga, *Chem. Mater*., 2008, **20**, 6364.
39. X. Liu, Q. Hu, Z. Fang, Q. Wu and Q. Xie, *Langmuir*, 2009, **25**, 7244.
40. S. Guo, D. Li, L. Zhang, J. Li and E. Wang, *Biomaterials*, 2009, **30**, 1881.
41. B. Marrtinz, X. Obradors, L. I. Balcells, A. Rouanet and C. Monty, *Phys. Rev. Lett*., 1998, **80**, 81.
42. A. V. Polishchuk, _E. T. Karaseva, T. B. Emelina, Y. M. Nikolenko and V. E. Karasev, *J. Struct. Chem*., 2009, **50**, 434.
43. Z. Zhou, Y. Zhang, Z. Wang, w. Wei, W. Tang, J. Shi and R. Xiong, *Appl. Surf. Sci*., 2008, **254**, 6972.
44. S. E. Skrabalak, B. J. Wiley, M. Kim, E. V. Formo and Y. Xia, *Nano Lett.*, 2008, **8**, 2077.
45. A. M. Koch, F. Reynolds, M. F. Kircher, H. P. Merkle, R. Weissleder and L. Josephson, *Bioconjugate Chem*., 2003, **14**, 1115.
46. L. Zhang, S. Hou, S. Mao, D. Wei, X. Song and Y. Lu, *Int. J. Pharm*., 2004, **287**, 155.
47. M. Guo, C. Que, C. Wang, X. Liu, H. Yan and K. Liu, *Biomaterials*., 2011, **32**, 185.
48. M. Tsurusawa, M. Niwa, N. Katano and T. Fujimoto, *Jpn. J Cancer Res*., 1990, **81**, 85.

49. I. Frouin, E. Prosperi, M. Denegri, C. Negri, M. Donzelli, L. Rossi, F. Riva, M. Stefanini and A. I. Scovassi, *Eur. J. Cancer*, 2001, **37**, 1173.
50. F. H. Chen, Q. Gao and J. Z. Ni, *Nanotechnology*, 2008, **19**, 165103.

Chapter-4

Multifunctional magnetic calcium phosphate nanoparticles for targeted platin delivery

4.1. Introduction

Research in nanotechnology has advanced to such an extent that it is possible to develop nanoparticles with specific functional properties that address the shortcomings of traditional disease diagnosis and therapy.[1–3] The imaging and delivery facilities have been significantly combined into unique NP construction through smart combinations of nanoscale materials, enabling simultaneous *in vivo* diagnostic imaging and drug delivery for real-time treatment tracking.[4,5] The successful development of the targeted drug delivery vesicles depend on a number of factors, such as biocompatibility of the material, suitable surface conjugation chemistry, favorable pharmacokinetic properties, possible cell uptake and ease of clinical translation.[6] With respect to this, calcium phosphate is considered as an excellent biocompatible inorganic material and its nanostructure can be hybridized with natural or synthetic polymers to form nanocomposites. Calcium phosphate has excellent biocompatibility due to its chemical similarity to human hard tissue (bone and teeth). In nanoparticulate dispersed form, it can be used as a carrier in biological systems, e.g. to transfer nucleic acids or drugs. Another important properties of calcium phosphate is that it can be easily functionalized with biomolecules and fluorescing dyes which is essential for imaging and photodynamic therapy.[7,8] In recent years, calcium phosphate/hydrophilic block copolymer based drug delivery systems have attracted considerable attention because they not only possess the properties of inorganic, organic ingredients but also the porous structure facilitates the incorporation of a high dosage of drug, which significantly enhances bio-performance.[9]

Magnetic ferrite nanoparticles have been recently exploited as a suitable alternative to superparamagnetic iron oxide nanoparticles (SPION) in biomedical applications including magnetic resonance imaging for clinical diagnosis, magnetic drug targeting and hyperthermia anticancer strategy.[10–12] Especially, spinel cobalt ferrite has been proposed for biomedical applications since it is known to have a large

anisotropy compared to other oxide ferrites, which could introduce several benefits in therapeutic applications for cancer therapy. The biocompatibility of cobalt ferrite nanoparticles has recently been demonstrated with therapeutic application in our previous chapter.[15] However, attempts to design a stealth magnetic calcium phosphate based nanosystem for multifunctional applications has rarely been reported.

On the other hand, platinum complexes such as cisplatin, carboplatin and oxaliplatin are widely used drugs in the treatment of solid tumors such as testicular, ovarian, breast, bladder, lung, head and neck carcinomas.[14] These drugs contain Pt–N/Pt–Cl, Pt–N/Pt–O coordination bonds with two Pt–N bonds in the cis- position. The Pt–Cl and Pt–O bonds in these complexes are chemically much weaker than the Pt–N bonds and are subject to facile hydrolysis under low Cl^- and/or low pH conditions giving charged $[Pt(NH_3)_2(H_2O)_2]^{2+}$ complexes. These are highly reactive for DNA binding, through the N7 atom, of either an adenine or guanine base. This binding interrupts the double helix structure and interrupts the cell's transcription as well as repair mechanism.[15] In spite of such a critical role, platin drugs do not have pervasive applications because of their systemic toxicity owing to their random distribution in the body. Selective inorganic nanoparticles based formulations have been developed for the target specific delivery of platinum drugs.[16–19] Although these nanoparticulate systems can serve as potential carriers for platinum drugs, their large dimension and the costly chemicals involved in the synthesis process may make them inappropriate for practical implementation. Therefore, the specific targeting of platinum drugs, by integrating a targeting functionality to the drug or delivery systems, is a current challenge in this area of research.

In the present work, we have fabricated porous amorphous calcium phosphate/$CoFe_2O_4$ integrated composite nanoparticles with high surface area. The surface of the particles was modified with N-phosphonomethyl iminodiacetic acid (PMIDA) in order to produce an iminodiacetic acid group on the surface. The platinum

pharmacophore cis-monochlorodiammineplatinum(II) (CMDP), folic acid (FA) and rhodamine B isothiocyanate (RITC) were loaded on to the amorphous calcium phosphate particles (ACP) through iminodiacetate groups forming a magnetic nanoparticles conjugate $CoFe_2O_4$/ACP-FA-CMDP-RITC. The intracellular uptake efficiency of the drug conjugated nanoparticles in HeLa cells was thoroughly investigated through fluorescence microscopy and flow cytometry (FACS). The pH sensitive drug release behavior has also been studied.

4.2. Experimental

Materials

Calcium nitrate, ferric nitrate and cobalt nitrate were obtained from Merck, Germany. Silver nitrate and diammonium hydrogen phosphate were procured from Rankem, RFCL limited, India. Poly(ethylene glycol)-block-poly(propylene glycol)-block-poly-(ethylene glycol), cisplatin, rhodamin B isothiocyanate (RITC), 2,2′-(ethylene dioxy)-bis-(ethyl amine) (EDBE), Folic acid (FA), di-tert-butyl-dicarbonate anhydrate (BoC_2O) and N-(phosphonomethyl) imino-diacetic acid were purchased from Sigma Aldrich. Dicyclohexylcarbodimide (DCC), N-hydroxysuccinamide (NHS) and 1-[3(dimethylamino) propyl]-3-ethyl carbodimide hydrochloride (EDC) were obtained from Spectrochem, India. Millipore water was used throughout the experiment.

Preparation of water dispersible $CoFe_2O_4$ nanoparticles

Cobalt ferrite nanoparticles were synthesized via an improved co-precipitation method. A stoichiometric amount of ferric nitrate (2 mmol, 0.808 g) and cobalt nitrate (1 mmol, 0.291 g) were taken in 100 ml of water and 5 ml of ethylene glycol in a 250 ml beaker. The pH was maintained at 10–12 by dropwise adding 1 M NaOH. A brown color precipitate appeared, and the mixture was heated at 80 °C for 2 h. Finally, black colloidal $CoFe_2O_4$ particles were obtained in the solution. The particles were recovered using a magnetic separator (DynaMag-2, Invitrogen), washed with millipore water (5 × 5 ml) and dried in a hot air oven at 80 °C for 2 h.

Synthesis of $CoFe_2O_4$/ACP/P123 composite nanoparticles

Synthesis of $CoFe_2O_4$/ACP/P123 composite nanoparticles is presented in Fig. 4.1. As prepared cobalt ferrite nanoparticles were dispersed in 40 ml of water followed by the addition of 5 ml of 0.5 M $CaCl_2$. Then the total mixture was added to the aqueous solution of block copolymer pluronic i.e.Poly(ethylene glycol)-Poly(propelene glycol)-Poly(ethylene glycol)/ (P-123) for 1 h at room temperature. 5 ml of 0.5 M diammonium hydrogen phosphate was added to the above solution at pH 10.

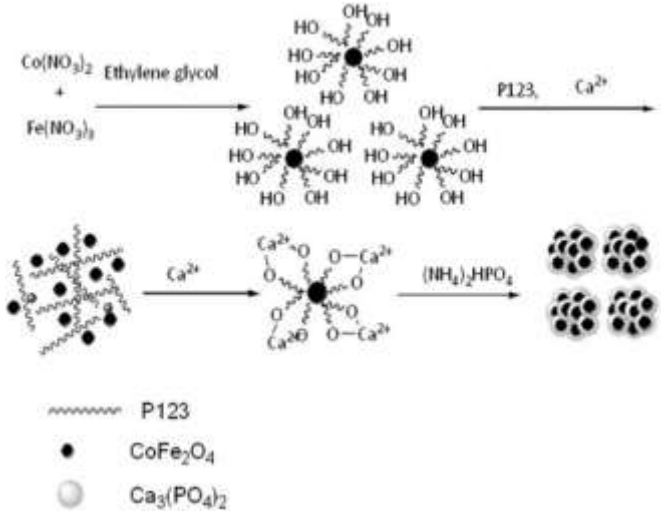

Fig. 4.1 Schematic representation for synthesis of porous $CoFe_2O_4$@ACP composites.

The particles were separated using a magnetic separator (DynaMag-2, Invitrogen).

Preparation of $CoFe_2O_4$-ACP-CDDP-FA

30 mg of CDDP was taken in 10 ml of water and 33 mg of $AgNO_3$ was added to it. The solution was stirred at room temperature for 48 h in the dark. The white precipitate of AgCl was removed by centrifugation and didechlorinated CDDP [cisdiaquadiamino platinum(II)] was obtained in supernatant. To get –COOH functionalized particles, 0.1 g of $CoFe_2O_4$@ACP particles were sonicated in 30 ml of water for 20 min. PMIDA (0.073 g) was added to the above solution and it was sonicated for another 5 min. Then, it was stirred for another 30 min at room temperature and finally particles were magnetically separated. The particles were washed thoroughly with water and methanol to free them from unreacted PMIDA. The acid functionalized $CoFe_2O_4$@ACP (120 mg) was dispersed with [cisdiaquadiamino platinum(II)] and sonicated to give a suspension. This was stirred for another 48 h at 45 °C in the dark and the pH was adjusted to slightly basic (9–10) with 0.1 M NaOH. After the completion of this reaction, particles were washed with PBS and recovered by using a magnetic separator.

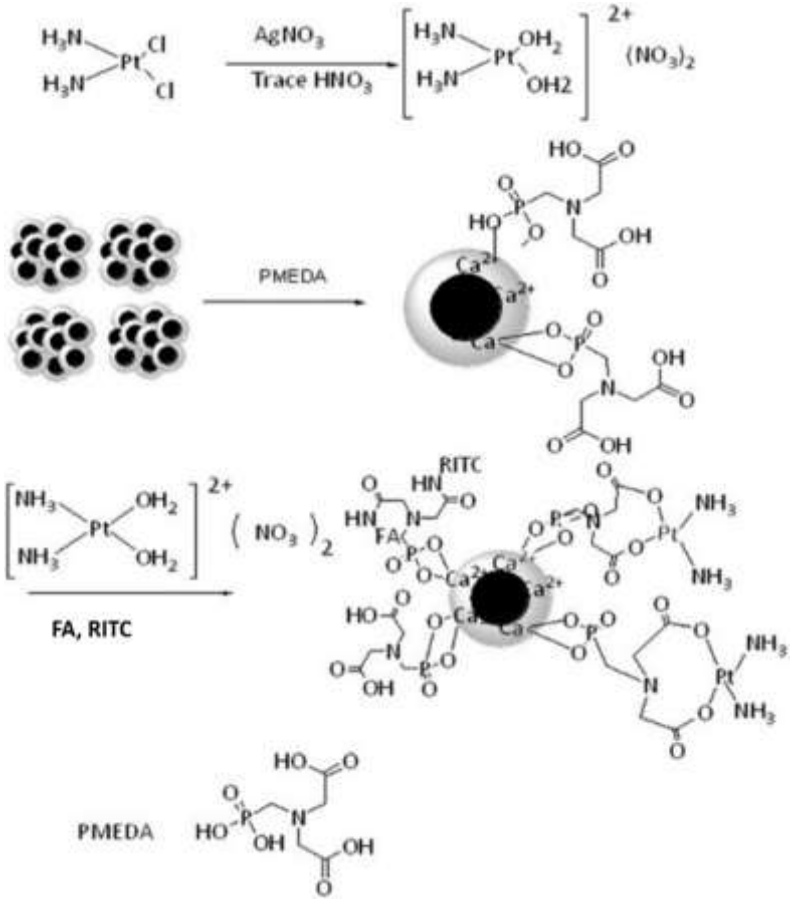

Fig. 4.2 Schematic representation for conjugation of cisplatin, folic acid and RITC onto porous –COOH functionalized $CoFe_2O_4$@ACP.

Folic acid and RITC functionalized with $–NH_2$ groups ($FA–NH_2$ and $RITC–NH_2$) were conjugated in stoichiometric amounts through the remaining –COOH groups on the surface, following our previously reported protocol.[20] So, the $CoFe_2O_4$-ACP-CDDP-FA was prepared using the following scheme (Fig. 4.2).

4.3. Characterization

The synthesized materials were well characterized by using standard techniques as described in chapter-3. Again the cytotoxicity and intracellular uptake experiments were performed following the protocol already described in chapter 3.

4.4. Results and discussion

It has been well demonstrated that magnetic nanoparticles with suitable surface coating show enhanced performance in biomedical applications rather than bare magnetic nanoparticles.[22] One important approach to modify its surface by coating inert inorganic materials like silica and Au.[23-25] We deemed to synthesize amorphous calcium phosphate due to extensive application of $Ca_3(PO_4)_2$ in biology and medicine. We prepared $Ca_3(PO_4)_2$ coated $CoFe_2O_4$ nanoparticles by seed-mediated deposition.[26,27] It is well established by Matsuda et. al. that the negative groups on the substrate could promote the growth of apatite much more strongly than positive groups.[28] The ethylene glycol coated $CoFe_2O_4$ particles (Scheme 4.1) act as a suitable substrate for the growth of amorphous calcium phosphate nanoparticles at alkaline pH. Magnetic nature of these particles makes their separation possible by using external magnet. Pluronic (P123) was used to prepare a highly porous $CoFe_2O_4$/ACP composite. We have prepared acid functionalized surface by reacting phosphonomethyl iminodiacetic acid (PMEDA). Based on the ability of phosphonic acid to exchange with the phosphate ions,[29,30] on HAp crystals, PMEDA has been chosen as a robust anchor to functionalize the porous magnetic substrate with –COOH groups (Fig. 4.2) to link up platinum moiety. In order to load cisplatin, first the platinum pharmacophore *cis*-diaminediaqua platinum(II) dinitrate was prepared by reacting 2 equivalents of $AgNO_3$ with cisplatin and subsequently loaded on porous magnetic support through –COOH groups by ligand exchange reaction.

XRD

Fig. 4.3a and 4.3b shows XRD patterns of $CoFe_2O_4$ and $CoFe_2O_4$@ACP, respectively. In the case of Fig. 4.3a, six diffraction peaks at 2θ = 30.2°, 35.4°, 43.1°, 57.0° and 62.6° assigned to inverse spinel $CoFe_2O_4$ (JCPDS no 22-1086). Fig. 4.3b did not show any characteristic peaks indicating amorphous calcium phosphate (ACP) phase.

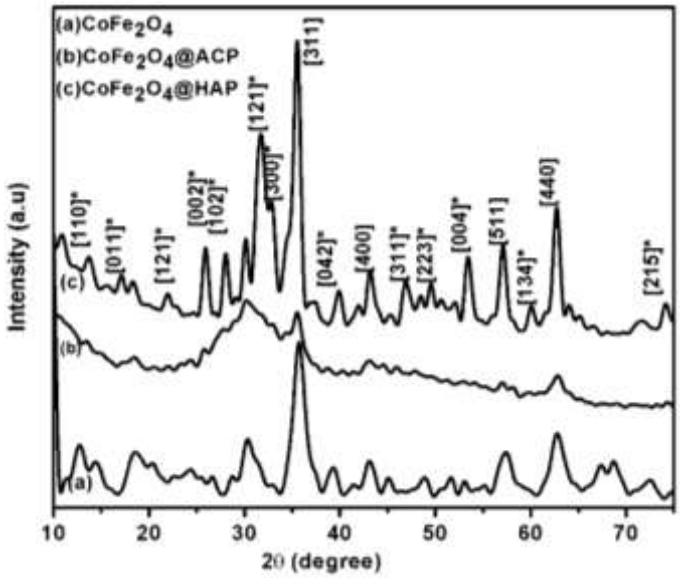

Fig. 4.3 XRD patterns of (a) $CoFe_2O_4$, (b) $CoFe_2O_4$@ACP, and (c)$CoFe_2O_4$@ACP after heating at 600 °C. * indicate peaks due to hydroxyapatite.

When the sample was further heated at 600 °C, peaks at 2θ = 13.7, 16.9, 20.9, 25.8, 27.9, 32.8, 39.9, 46.7, 49.4, 53.4, 60.11 and 74.23 corresponding to hexagonal hydroxyapatite (JCPDS 84-1998) [$Ca_5(PO_4)_3OH$] became more prominent. The XRD pattern indicates the successful deposition of amorphous calcium phosphate (ACP) on crystalline $CoFe_2O_4$ nanoparticles.

SEM-EDX

The SEM image (Fig. 4.4) shows spherical clusters of $CoFe_2O_4$@ACP core-shell nanoparticles with a size of 50 nm and which is in well aggregate with TEM image. Due to spherical structure of nanoparticles it shows high surface area. SEM-

EDX data shows the presence of Co, Fe, Ca and Pt with an atomic ratio of 2.44: 4.79: 6.83: 5.4.

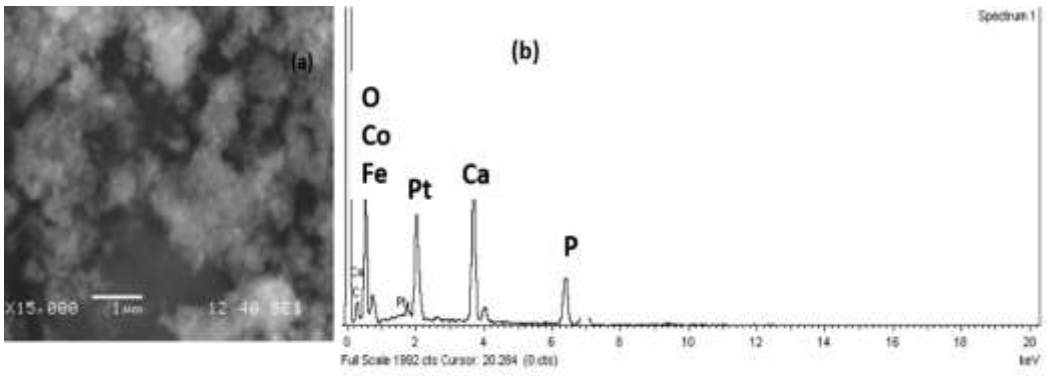

Fig. 4.4 (a) SEM image of $CoFe_2O_4$@ACP-CDDP-FA-RITC nanoparticles and (b) EDX spectrum of CoFe2O4@ACP-CDDP-FA-RITC nanoparticles.

Hydrodynamic size and zeta potential measurement

The measurement of the hydrodynamic size of $CoFe_2O_4$@ACP after each step of conjugation in phosphate buffer saline (PBS) by dynamic light scattering shows stable nanoaggregate particles with PDI < 0.3. The mean HD size of as synthesized $CoFe_2O_4$@ACP particles was found to be 42 nm (Fig. 4.5). However, the mean HD size was further increased to 62 nm after conjugation with folic acid and the platinum complex. The HD size, PDI and intensity of each particle remained unaffected over a long period indicating the colloidal stability of synthesized particles in PBS. The surface charge of drug conjugated particles ($CoFe_2O_4$@ACP-CDDP-FA) measured with different pH and it was found that zeta potential increases in negative direction with increase in pH and the surface charge remain unaltered after a long time, which it indicates the conjugated particles are highly stable in physiological environment.

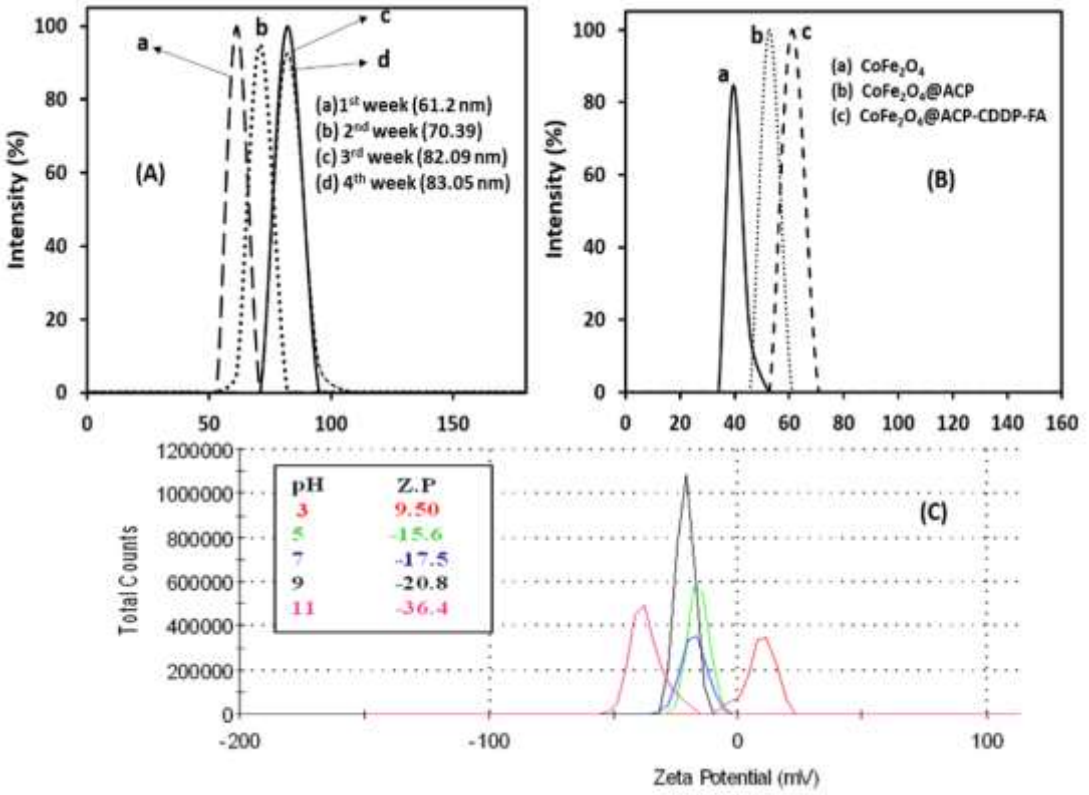

Fig. 4.5 (A) Change in hydrodynamic size of $CoFe_2O_4$@ACP-CDDP-FA with respect to time, (B) Variation of hydrodynamic size after each step of modification, (C) Zeta potential variation of $CoFe_2O_4$@ACP-CDDP-FA with respect to respect to pH.

TEM

The microstructures of particles at various stages of synthesis were examined by transmission electron microscopy. Fig. 4.6a represents the micrograph of $CoFe_2O_4$ nanoparticles precipitated in the presence of ethylene glycol. In spite of magnetic interaction the particles show good dispersion due to surface protection by ethylene glycol. Particles show narrow distribution between 8–12 nm with a mean diameter of 10 ± 0.5 nm. From the high resolution TEM the interplanar distance d is calculated as 4.8 Å, which corresponds to the reflection of the [111] plane. The individual planes identified from the SAED pattern correlate with the XRD pattern. Fig. 4.6b shows micrographs of $CoFe_2O_4$@ACP–P123 composite nanoparticles. It appears that the $CoFe_2O_4$@ACP–P123 composites have irregular shape and porous morphology.

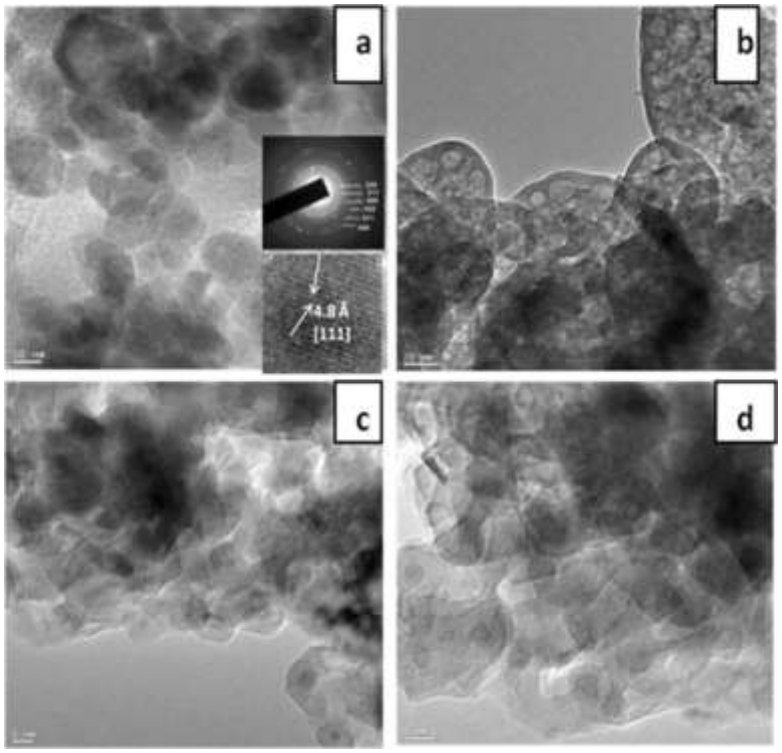

Fig. 4.6 (a) TEM image and SAED pattern (inset) of ethylene glycol coated CoFe2O4, (b) polymer coated $CoFe_2O_4$@ACP, and (c) $CoFe_2O_4$@ACP after washing. (d) $CoFe_2O_4$@ACP at high resolution showing core-shell structures.

However, after removal of the copolymer (Fig. 4.6c) porous spherical structures of $CoFe_2O_4$@ACP were observed, which is in line with the SEM image. The image at high magnification (Fig. 4.6d) shows that each porous sphere consists of $CoFe_2O_4$@ACP core-shell nanoparticles with a spherical cobalt ferrite core and a uniform calcium phosphate shell.

Formation mechanism of $CoFe_2O_4$ @ ACP nanocomposites

The formation mechanism for the core-shell nanoparticles can be proposed according to Fig. 4.2. Ethylene glycol strongly adsorbs on the surface of ferrite nanoparticles and forms a negatively charged attracts positively charged Ca^{2+} ions by coulombic force of attraction and latter attracts PO_4^{3-} which triggers the nucleation of calcium phosphate on the surface of cobalt ferrite. With time these fine core shell particles agglomerate to form clusters, possibly due to the surface energy being minimized. However, the block copolymers impart porous nature to the cluster. The micelle of the P123 can act as a soft template for the formation of a porous hybrid nanocomposite.

FTIR

The FTIR spectrum of as prepared $CoFe_2O_4$ (Fig. 4.7) shows strong absorption at 597 cm^{-1} corresponding to the M–O stretching vibration. Additionally, the faint impression of the methylene signature is also visible at 2906 and 2850 cm which indicates chemical adsorption of ethylene glycol on the $CoFe_2O_4$ surface. In the case of $CoFe_2O_4$@ACP nanoparticles prepared in the presence of block polymer P123, peaks at 1104, 1038, 600 and 558 cm^{-1} represent characteristic stretching and bending modes of PO_4^{3-}. It indicates the deposition of amorphous calcium phosphate on the surface of $CoFe_2O_4$ nanoparticles. More intensification of the methylene signature may be attributed to the presence of the block copolymer on $CoFe_2O_4$ @ACP core-shell nanoparticles even after leaching. It is probably due to inter particle hydrogen bonding after surface modification with PMIDA. In $CoFe_2O_4$@ACP-PMIDA–CDDP particles there is a slight shifting of carboxylate stretching towards lower frequency indicating the coordination of carboxylates to Pt. $CoFe_2O_4$@ACP–PMIDA–CDDP–FA shows bands in the range of 1642 to 1466 cm^{-1}. The appearance of two prominent characteristic bands at 1603 (amide I) and 1510 (amide II) cm^{-1} indicate that folic acid has been conjugated to $CoFe_2O_4$@ACP–PMIDA nanoparticles through amide linkages according to Fig. 4.7c. X-Ray photoelectron spectra and

SEM-EDX were further used to validate the successful complexation of platinum on the synthesized magnetic calcium phosphate matrix.

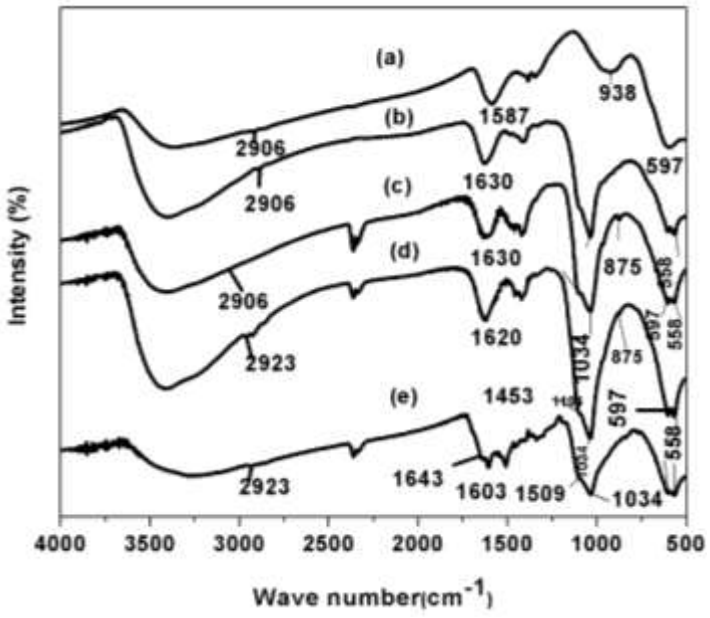

Fig. 4.7 FTIR at various stages of synthesis: (a) $CoFe_2O_4$, (b) $CoFe_2O_4$@ACP, (c) $CoFe_2O_4$@ACP-PMIDA, (d) $CoFe_2O_4$@ACP-PMIDA-CDDP and (e) $CoFe_2O_4$@ACP-PMIDA-CDDP-FA nanoparticles.

XPS

In the XPS spectra of CDDP loaded particles (Fig. 4.8) the C1s peak corresponding to the reference shows a shift of 3 eV towards the higher side and hence, taking the reference shift into consideration, all other binding energies are calculated. The Gaussian fit to the high resolution scan of C1s shows four peaks centred at 288.36, 289.9, 291.3 and 293.8 eV corresponding to C–C/C–H, C–N/C–O, NHCO and -COOH, respectively. The O1s peak is observed at 534 eV and the three peaks a534.1, 534.7, 536.3 eV can be fitted to double bonded oxygen (C=O and/or P=O), single bonded oxygen (C–O–P and/or P–O–P)[31] and chemisorbed oxygen and/or water. The N1s binding energy appears at 402.5, 402.9, 403.6, which may be attributed to NH_3 in cisplatin,[32] NHCO and/or C=N (N bonded to two sp^2 carbons)

and tertiary nitrogen (nitrogen bonded to three sp^3 carbons), respectively. The unidentified peak at higher binding energy with low intensity may be due to presence of traces of protonated amines. The P2p peak in the range of 130.9 to 139.5 corresponds to pentavalent tetra coordinated phosphorus[31] associated with low intensity shake ups. The high resolution scan of the Pt4f region shows two peaks centred at 76.72 and 79.72 eV for $Pt4f_{7/2}$ and $Pt4f_{5/2}$, respectively.

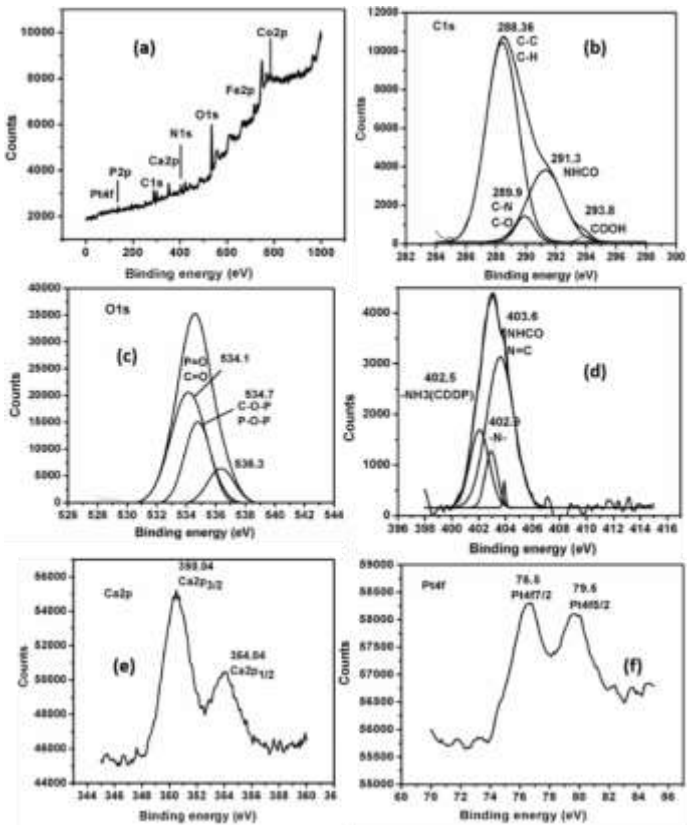

Fig. 4.8 (a) XPS survey spectrum of $CoFe_2O_4$@ACP-CDDP-FA. High resolution scans of (b) C1s, (c) O1s, (d) N1s, (e) Ca2p, (f) Pt4f

Nitrogen adsorption–desorption study

The porous nature of the nanocomposite was further investigated using nitrogen adsorption and desorption experiment (Fig. 4.9). The BET surface area of $CoFe_2O_4$@ACP nanosphere was found to be 296 m^2g^{-1}. The corresponding BJH pore size distribution was significantly narrow and centered at 7 nm. The large surface area with a narrow pore size of 7 nm is favourable for higher adsorption, which would be particularly beneficial in drug delivery applications.

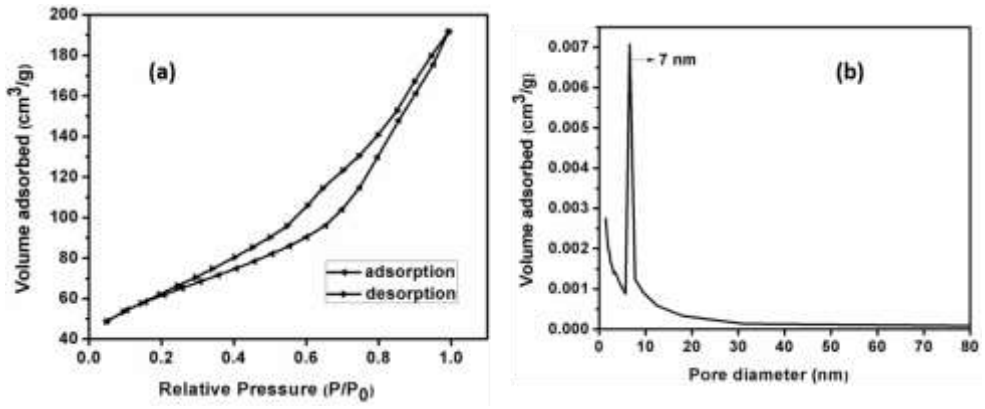

Fig. 4.9 Nitrogen adsorption-desorption isotherm and the corresponding pore size distribution (inset) of as synthesized $CoFe_2O_4$ nanoparticles.

Room temperature magnetic moment study

The magnetic properties of the products, $CoFe_2O_4$ and $CoFe_2O_4$@ACP–PMIDA–CDDP–FA particles, were examined by vibration sample magnetometry. Fig. 4.10 shows the magnetic hysteresis opening with saturation magnetization of 46 e.m.u. g^{-1} and 25 e.m.u. g^{-1}, respectively. The Ms value of $CoFe_2O_4$@ACP–PMIDA–CDDP–FA decreased evidently after coating with ACP, because the diamagnetic contribution of the thick ACP shell resulted in a low mass fraction of magnetic $CoFe_2O_4$. The Ms value of the synthesized $CoFe_2O_4$ is less than that of bulk $CoFe_2O_4$ (71.2 e.m.u. g^{-1}). This decrease in saturation magnetization is due to surface spin canting, owing to small particle sizes.[33] Unlike the superparamagnetic $CoFe_2O_4$

nanoparticles synthesized by thermal decomposition method, as reported in our previous work, here both the samples show coercivity (H_c) and remanent magnetization (Mr). The H_c values for $CoFe_2O_4$ and $CoFe_2O_4$@ACP–PMIDA–CDDP–FA were found to be 0.64 kOe and 0.9 kOe. The coercivity may be attributed to magnetic anisotropy, strain, and disorder of the surface spins of $CoFe_2O_4$ nanoparticles, as reported by Limaye et al. for the case of oleic acid coated $CoFe_2O_4$ nanoparticles.[34] The higher H_c in the case of $CoFe_2O_4$@ACP may be due to the higher amorphicity and smaller magnetic core of ACP coated cobalt ferrite nanoparticles.

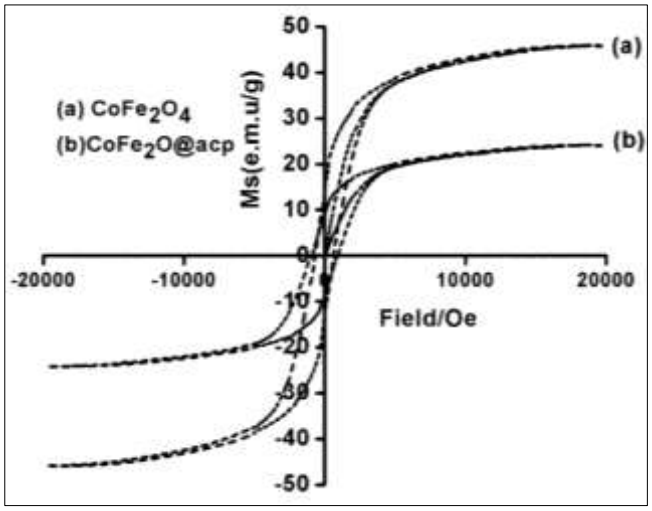

Fig. 4.10 Field-dependent magnetization of as prepared $CoFe_2O_4$ and $CoFe_2O_4$@ACP nanoparticles.

pH dependant drug release

The drug release profiles are plotted as cumulative release against time (Fig. 4.11). It is observed that in all pH conditions the CDDP showed a rapid release pattern from the beginning followed by a sustained release pattern. Additionally, at pH 4.3, ~45% of the drug was released from $CoFe_2O_4$@ACP–PMIDA–CDDP–FA particles after 10 h, while at pH 5.4 the amount of platin released was reduced to

28%. At pH 7.4 the release was further reduced to 10%. Undoubtedly, the lower pH condition accelerates the release of platin drug from the drug conjugated nanoparticles. In lysosome, the pH is ~5, so platin release will be accelerated once the conjugate is taken inside the endosome.

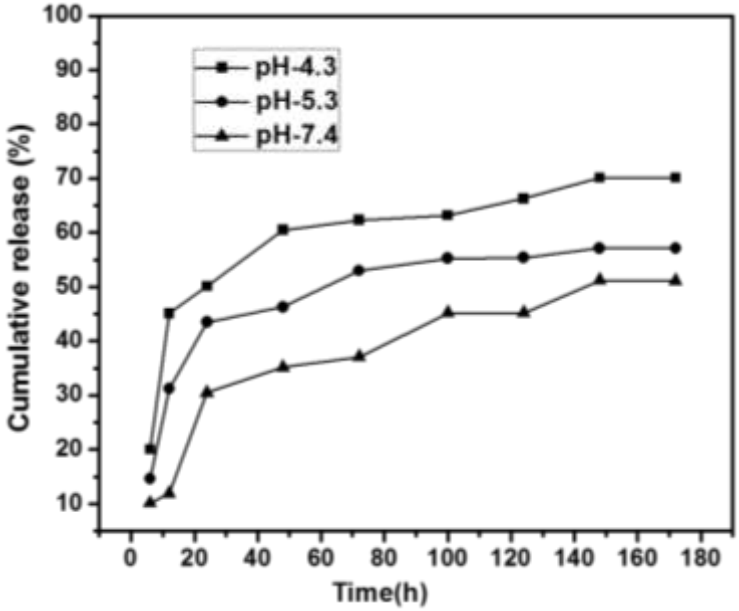

Fig. 4.11 Drug release profile over time at different pH.

MTT assay

The antitumor potential of $CoFe_2O_4$@ACP–PMIDA–CDDP–FA was verified against HeLa cells by MTT assay (Fig. 4.12). It shows that our drug carrier $CoFe_2O_4$@ACP–PMIDA–FA barely exhibits cytotoxicity against HeLa cells. In contrast, the CDDP conjugated carrier demonstrates a remarkable inhibition towards the growth of HeLa cells. The IC_{50} of $CoFe_2O_4$@ACP–PMIDA–CDDP–FA and cisplatin towards HeLa cells in terms of Pt concentration is 0.6 and 2.2 μM; and those towards L929 cells is 3.1 and 4.4 μM (Table 4.1). It indicates that the antitumor activity of cisplatin is enhanced after being adsorbed on functionalized ACP surface. The cytotoxicity of synthesized $CoFe_2O_4$@ACP and $CoFe_2O_4$@ACP–PMEDA was

also verified in normal cell line i.e. L929 cells. The results confirm that these nanoparticles do not have cytotoxicity and hence are safe for biomedical applications.

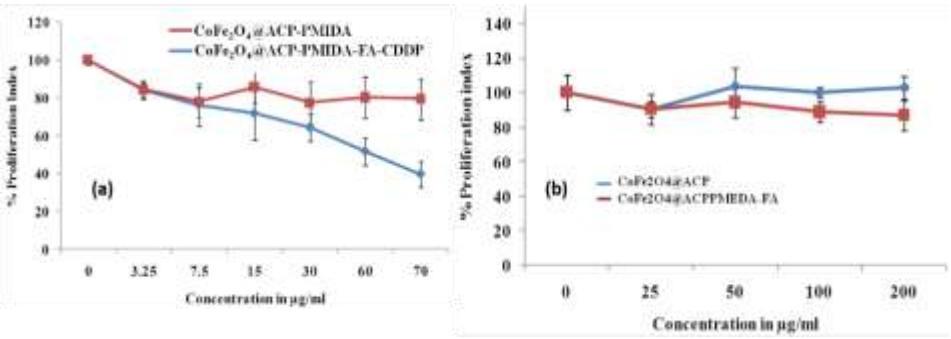

Fig. 4.12 Cytotoxicity assay of nanoparticles on (a) HeLa and (b) L929 cells. Cells were treated with different concentrations of nanoparticles for 72 h and cell viability was measured by MTT assay

Table 4.1 Comparison of IC_{50} values for HeLa and L929 cells as measured by MTT assay.

IC_{50} (μM)	$CoFe_2O_4$@ACP -PMEDA	$CoFe_2O_4$@ACP -PMEDA-CDDP-FA	Cisplatin
Hela	-----	0.6	2.2
L929	-----	3.1	4.2

Uptake with HeLa and L929

In vitro cellular uptake experiments were performed taking human cervical cancer cell (FR +ve) and L929 (FR -ve) as control and DAPI was used as a nuclear contrast dye to appreciate localization. The uptake of $CoFe_2O_4$@ACP–PMIDA–CDDP–FA particles was evident after 30 min (Fig. 4.13). The fluorescence signal from RITC increased in the cytoplasm surrounding the nucleus in HeLa cells. In

contrast, no such increase in RITC signals were seen in the case of L929 cells. This suggested that CDDP-conjugated particles are selectively targeted to HeLa cells through FR mediated endocytosis and localized in the cytoplasm.

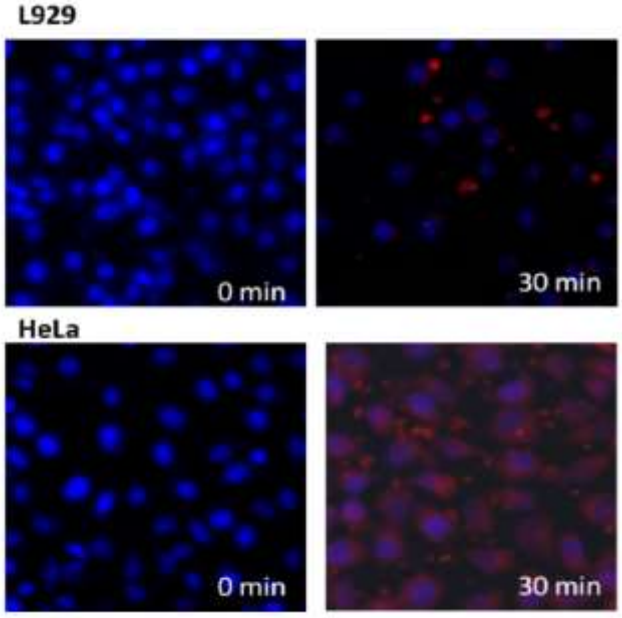

Fig. 4.13 Uptake of $CoFe_2O_4$@ACP–PMIDA–FA–CDDP-RITC nanoparticles in L929 and HeLa cell using fluorescence microscopy.

To verify the nuclear morphology and cell death the cell nuclei were further stained with 4'-6-diamidino-2-phenylindole (DAPI), a nuclear staining dye known to exhibit strong blue fluorescence when bound to DNA. As predicted from cytotoxicity experiments, the fluorescent images of HeLa cells incubated with drug unloaded particles (control) show the nuclear structures are almost preserved with abnormalities, whereas cells treated with $CoFe_2O_4$@ACP–PMIDA–CDDP–FA displayed typical apoptotic morphology such as nuclear fragmentation, condensation and formation of apoptotic bodies (Fig. 4.14).

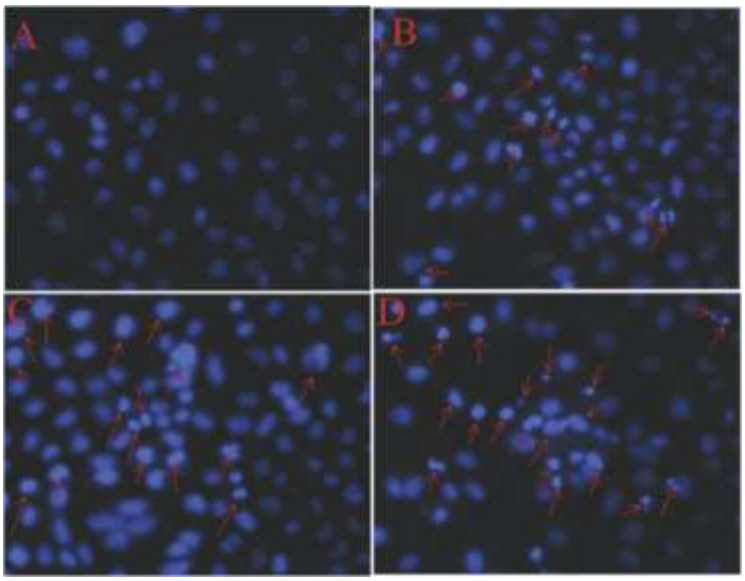

Fig. 4.14 DAPI fluorescence (200X) images of HeLa incubated with (A) PBS, (B) 5, (C) 30, (D) 60 µg ml^{-1} of $CoFe_2O_4$@ACP-CDDP-FA for 24 h.

Flow cytometry analysis

A quantitative evaluation of the $CoFe_2O_4$@ACP–PMIDA–CDDP–FA nanoparticles mediated cell death was carried out using cell cycle analysis, using propidium iodide (PI) flow cytometry .Significant DNA fragmentation was observed for $CoFe_2O_4$@ACP–PMIDA–CDDP–FA with respect to the control under similar conditions, evidenced by a sub-G1 peak in the DNA fluorescence histogram (Fig. 4.15). A decrease in cells in G0/G1 phase with an increase in cell concomitant in S and G2/M phase indicates that the arrest of cell cycle in S and G2/M phase. The S and G2/M phase distribution increased from 9.36% and 13.16% (in control) to 31.73% and 26.64% with 90 µg ml^{-1} treated cells. Consistent with the mode of action of platinum complexes, the cell cycle was arrested in both S and G2 phase.[35,36] This arrest is accountable for appreciable morphological changes in cell, as visualized by fluorescence microscopy, and ultimately resulted in cell death. In vitro drug release

experiments were carried out at 37 °C in aqueous HEPES buffer and monitored for 180 h.

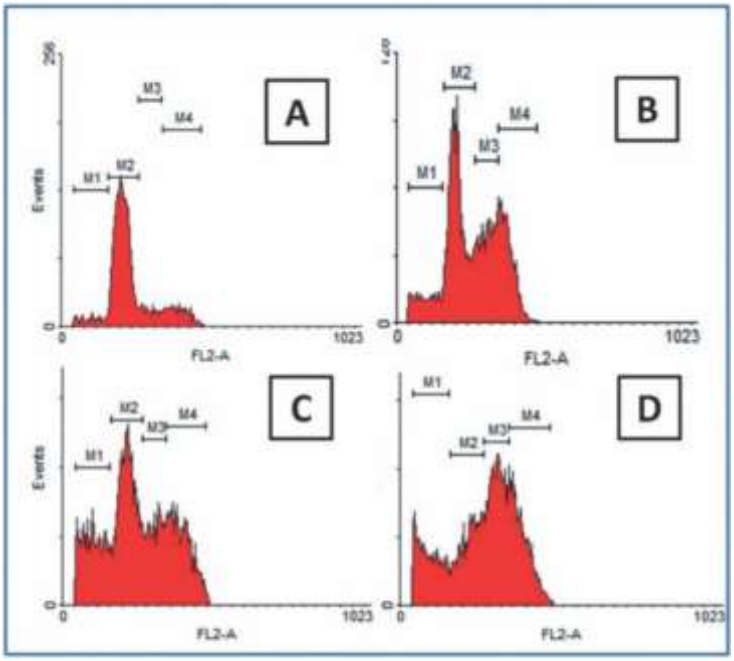

Fig. 4.15 Flow cytometric analysis of the cell cycle phase distribution in HeLa cells. HeLa cells treated with (A) PBS (control), (B) 30 μg ml^{-1}, (C) 60 μg ml^{-1}, and (D) 90 μg ml^{-1} of $CoFe_2O_4$@ACP–CDDP–FA nanoparticles for 48 h and the percentage of DNA content was determined by FACS calibour (BD) using Flow Jo software.

4.1 Conclusion

Highly water soluble magnetic mesoporous $CoFe_2O_4$@ACP composite nanoparticles with a diameter of 41 nm have been prepared using block copolymer P123. The surfaces of the amorphous calcium phosphate have been modified with phosphonomethyl iminodiacetic acid to produce a highly –COOH functionalized surface. Development a nanoparticles based formulation for the controlled as well as targeted delivery of cisplatin has been satisfied by conjugating folic acid, cisplatin and RITC on the surface following simple chemistry. The nano drug carrier is effectively targeted to cancer cells, causing the optimal delivery of cisplatin and resulting in cell death following the induction of apoptosis. The advantages of this drug delivery system include simple and scalable synthesis method,

multifunctionality of particles, high drug loading capacity and pH sensitive release behaviour.

4.6. References

1. M. Ferrari, *Nat. Rev. Cancer*, 2005, **5**, 5161.
2. N. Sanvicens and M. P. Marco, *Trends Biotechnol*., 2008, **26**, 425.
3. O. C. Farokhzad and R. Langer, *Adv. Drug Delivery Rev*., 2006, **58**, 1456.
4. V. P. Torchilin, *Adv. Drug Delivery Rev*., 2006, **58**, 1532.
5. C. Sun, J. S. H. Lee and M. Q. Zhang, *Adv. Drug Delivery Rev*., 2008, **60**, 1252.
6. O. C. Farokhzad and R. Langer, *ACS Nano*, 2009, **3**, 16.
7. M. Epple, K. Ganesan, R. Heumann, J. Klesing, A. Kovtun, S. Neumann and V. Sokolova, *J. Mater. Chem*., 2010, **20**, 18.
8. Q. Tang, Y. J. Zhu, Y. R. Duan, Q. Wang, K. W. Wang, S. W. Cao, F. Chen and J. Wu, *Dalton Trans*., 2010, **39**, 4435.
9. M. C. Chang, C. C. Ko and W. H. Douglas, *Biomaterials*, 2003, **24**, 2853.
10. L. D. Tung, V. L. Kolesnichenko, D. Caruntu, N. H. Chou, C. J. O'Connor and L. Spinu, *J. Appl. Phys*., 2003, **93**, 7486.
11. R. E. Rosenweig, J. Magn. Magn. *Mater*., 2002, **252**, 370.
12. J. P. Fortin, C. Wilhelm, J. Servais, C. Menager, J. C. Bacri and F. Gazeau, *J. Am. Chem. Soc*., 2007, **129**, 2628.
13. S. Mohapatra, S. R. Rout, S. Maiti, T. K. Maiti and A. B. Panda, *J. Mater. Chem*., 2011, **21**, 9185–993.
14. B. Lippert, Cisplatin: *Chemistry and Biochemistry of a Leading Anticancer Drug*, *Wiley-VCH*, 1999.
15. L. Kelland, *Nat. Rev. Cancer*, 2007, **7**, 573.
16. R. Xing, X. Wang, C. Zhang, J. Wang, Y. Zhang, Y. Song and Z. Guo, *J. Mater. Chem*., 2011, **21**, 11142.
17. C. Xu, B. Wang and S. Sun, *J. Am. Chem. Soc*., 2009, **131**, 4216.
18. S. Likhitkar and A. K. Bajpai, *Carbohydr. Polym*., 2012, **87**, 300.
19. A. Taylor, Y. Krupskaya, K. Krämer, S. Füssel, R. Klingeler, B. Büchner and M. P. Wirth, *Carbon*, 2010, **48**, 2327.

20. S. Mohapatra, S. K. Mallick, T. K. Maiti, S. K. Ghosh and P. Pramanik, *Nanotechnology*, 2007, **18**, 385102.
21. S. Maiti, S. K. Bhutia, S. K. Mallick, A. Kumar, N. Khargi and T. K. Maiti, *Environ. Toxicol. Pharmacol*., 2008, **26**, 187.
22. A. K. Gupta and M. Gupta, *Biomaterials.*, 2005, **26**, 3992.
23. J. L. Lyon, D. A. Fleming, M. B. Stone, P. Schiffer and M. E. Williams, *Nano Lett.*, 2004, **4**, 719.
24. J. Lim, A. Eggeman, F. Lanni, R. D. Tilton and S. A. Majetich, *Adv. Mater.*, 2008, **20**, 1721.
25. H. Y. Park, M. J. Schadt, L. Wang, I. I. S. Lim, P. N. Njoki, S. H. Kim, M. Y. Jang, J. Luo and C. J. Zhong, *Langmuir*, 2007, **23**, 9050.
26. D. Rautaray, S. Mandal and M. Sastry, *Langmuir*, 2005, **21**, 5185.
27. I. Ming-Tang, N. Krishnamra, N. Charoenphandhu, R. Hoonsawat and W. Pon-On, *Nanoscale Res. Lett*., 2011, **6**, 19.
28. M. Tanahashi and T. Matsuda, *J. Biomed. Mater. Res*., 1997, **34**, 305.
29. Y. E. Greish and P. W. Brown, *Biomaterials*, 2001, **22**, 807.
30. N. Pramanik, S. Mohapatra, P. Bhargava and P. Pramanik, *Mater. Sci. Eng., C*, 2009, **29**, 228.
31. A. M. Puziy, O. I. Poddubnaya and A. M. Ziatdinov, A*ppl. Surf. Sci.*, 2006, **252**, 8036.
32. J. Y. Han, T. T. Y. Tan and J. S. C. Loo, *J. Nanopart. Res*., 2011, **13**, 3441.
33. B. Martínez, X. Obradors, L. I. Balcells, A. Rouanet and C. Monty, *Phys. Rev. Lett*., 1998, **80**, 181.
34. M. V. Limaye, S. B. Singh, S. K. Date, D. Kothari, V. R. Reddy, A. Gupta, V. Sathe, R. J. Choudhary and S. K. Kulkarni, *J. Phys. Chem.*, 2009, **113**, 9070.
35. G. Zhu and S. J. Lippard, *Biochemistry*, 2009, **48**, 4916.
36. X. Pan, M. Wilson, L. Mirbahai, C. McConville, T. N. Arvanitis, J. L. Griffin, R. A. Kauppinen and A. C. Peet, *J. Proteome Res*., 2011, **10**, 3493.

Chapter-5

Multifunctional cobalt ferrite encapsulated mesoporous hollow silica nanocapsules for targeted co-delivery of cisplatin-premetrexed and MR imaging

5.1. Introduction

Multifunctional nanomaterials with combined features of diagnostic and therapeutic applications have been one of the key issues in nanomedicinal research.[1–4] The main approach for the design of multifunctional theranostic nanoparticles is the simultaneous incorporation of a diagnostic element and therapeutic agents into a single particle. Among the matrix materials used for theranostic applications, mesoporous silica is a promising platform for the delivery of drug molecules and imaging agents due to its well documented biocompatibility.[5–14] Importantly, by adding diverse functional inorganic nanostructures (such as Fe_3O_4 magnetic nanoparticles,[15] Au nanocrystals,[16] and quantum dots[17]) or by chemically grafting functional groups (tumor-targeting moieties,[18] fluorescent molecules,[19] PEG,[20] etc.) onto the mesoporous silica surface, multifunctional nanostructured materials can be produced that are potential platforms for biomedical imaging and simultaneous therapy for lesion sites such as cancers.[21] Compared to conventional mesoporous materials, hollow mesoporous spheres are expected to show increasing therapeutic efficiency because of their large surface area, high pore volume, and tunable pore sizes which facilitate incorporation of ample therapeutic agents.[22–26] In addition, the large fraction of voids in their inner space can seal drugs, thus protecting biomedicines from degradation or interaction with the biological environment before they reach the target site. Several research groups have made extensive reports on the synthesis of hollow mesoporous silica or heteroatom incorporated mesoporous silica for the delivery of a number of hydrophobic as well as hydrophilic anticancer drugs.[27–30]

On the other hand, combination therapy or simultaneous administration of multiple drugs has become a widely adopted strategy in clinical cancer therapy.[31] Clinical and preclinical studies have shown that cocktail therapy of cancer with dual drug combinations may lead to better tumor regression than either drug alone.[32] For instance, cisplatin has been the mainstay chemotherapy drug for the treatment of

mesothelioma and non-small cell cancers. However, it has been verified that a relatively new drug, pemetrexed (Alimta, Eli Lily), when given with cisplatin, can reduce tumor size up to 40% and thus increase the longevity of the patient.[33] Pemetrexed is a new generation antifolate antimetabolite that exhibits its anticancer activity by potentially inhibiting the action of multiple enzymes such as dihydrofolate reductase (DHFR), glycinamide ribonucleotide formyl transferase (GARFT), and thymidyl synthetase which are involved in de novo purine synthesis.[34] However, the prominent molecular action of pemetrexed is essentially governed by its efficient cellular internalization and retention. In the form of free acid, pemetrexed is poorly water-soluble and sensitive to light, heat, and moisture, and also has a strong tendency for degradation.[35] Also, the administration of pemetrexed in the form of a disodium salt fails to provide a high aqueous solubility and more stable storage.[36] Thus the administration of the drug at a high dose and frequent dosage program results in systemic toxicity.[37] To the best of our knowledge, there are very few reports on the development of stealth drug delivery systems for the successful administration of pemetrexed in its acid form.[38,39]

The necessity of enhancing the therapeutic efficiency of pemetrexed by active targeting and the success in combining pemetrexed with platinum anticancer drugs inspired us to synthesize a highly water soluble multifunctional biocompatible mesoporous drug delivery vehicle not only to safeguard both the drugs but also to enable the real time monitoring of the treatment by magnetic resonance imaging or fluorescence imaging. In the present work, we have developed hollow mesoporous silica nanoparticles with high surface area which are capable of delivering both the therapeutic cargoes. The hollow interior space can encapsulate the hydrophobic drug pemetrexed and the magnetic oxide based T2 contrast agent where the hydroxyl groups on the exterior surface can be chemically modified to conjugate platinum anticancer drugs, folic acid and the fluorescent molecule RITC. The structure and physical properties of the multifunctional nanoparticles were established through a series of

physical characterization like X-ray diffraction analysis (XRD), superconducting quantum interference devices (SQUID), scanning electron microscopy (SEM), transmission electron microscopy (TEM), Fourier transform infrared spectroscopy (FTIR) and X-ray photoelectron spectroscopy (XPS) studies. The dynamic light scattering (DLS) and zeta potential studies confirm the excellent stability of our system over time. We have demonstrated that such a dual drug loaded nanoparticle would be more effective than a single drug by the cytotoxicity assay and cell apoptosis studies.

5.2. Experimental

Materials

Calcium nitrate and di-ammonium hydrogen phosphate were obtained from Merck, Germany. Silver nitrate and diammonium hydrogen phosphate, and ethylene glycol were procured from Rankem, RFCL Limited. Benzyl ether, cetyltrimethylammonium bromide (CTAB), $Fe(acac)_3$, $Co(acac)_2$, 3-aminopropyltrimethoxy silane (APTS), oleic acid, oleylamine, tetraethyl orthosilicate (TEOS), folic acid (FA), cisplatin, pemetrexed disodium, rhodamine B isothiocyanate (RITC), 2,2′- (ethylene dioxy)-bis-(ethyl amine) (EDBE), di-tert-butyl-dicarbonate anhydrate (BoC_2O) and dimercaptosuccinic acid (DMSA) were purchased from Sigma Aldrich. Dicyclohexylcarbodiimide (DCC), N-hydroxysuccinamide (NHS) and 1-[3dimethylamino) propyl]-3-ethyl carbodiimide hydrochloride (EDC) were obtained from spectrochem, India. Commercially available toluene was purified by distillation over sodium metal with benzophenone. Prior to use, dimethylsulfoxide (DMSO) was vacuum distilled. All other reagents and solvents were used without further purification. Millipore water (18.2 MΩ cm) was used throughout the experiment.

Synthesis of monodisperse hydrophobic $CoFe_2O_4$ nanoparticles

$CoFe_2O_4$ nanoparticles were prepared by the solvothermal method (Figure. 5.1). Briefly, $Fe(acac)_3$ (706 mg, 2 mmol), $Co(acac)_2$ (257 mg, 1 mmol), 1,2 dodecanediol (2.023 g, 10 mmol), oleic acid (1.9 ml, 6 mmol), oleylamine (1.97 ml, 6 mmol) and benzyl ether (30 ml) were mixed and stirred for 15 minutes at room temperature. Then the total mixture was transferred to a teflon lined stainless steel autoclave and heated for 10 h at 190 °C. Then the as synthesized mixture was allowed to cool to room temperature and $CoFe_2O_4$ nanoparticles were precipitated by adding ethanol. The precipitate was collected by centrifugation at a speed of 1600 rpm for 10 minutes and dried under vacuum for 48 h.

Transferring hydrophobic $CoFe_2O_4$ nanoparticles to water through ligand exchange

Hydrophobic $CoFe_2O_4$ nanoparticles synthesized above were oil soluble and not suitable for biological application. To make this sample water soluble, a ligand exchange reaction was carried out with dimercapto succinic acid (DMSA). 200 mg of the dried sample was dispersed in 80 ml of hexane and 100 mg DMSA was dispersed in 100 ml acetone as well as 0.1 ml of TEA were added to a 250 ml flask one after another. The total mixture was stirred and refluxed for 4 h, and a black precipitate appeared at the bottom, signifying that the DMSA molecules have been conjugated on the surface of $CoFe_2O_4$ NPs. A homogeneous colloid was obtained by dissolving it with deionized water.

Synthesis of $CoFe_2O_4$/HAP/SiO_2 composite nanoparticles

The DMSA coated $CoFe_2O_4$ nanoparticles were dispersed in 40 ml water followed by addition of an aqueous solution of calcium nitrate. Then the total mixture was stirred for 30 minutes at pH 10. After that 10 ml diammonium hydrogen phosphate was added dropwise to the above solution at pH 10. The particles were separated using a magnetic separator (Dynamag2, Invitrogen). 200 mg of the

$CoFe_2O_4$/HAP composite nanoparticles were dispersed ultrasonically into a mixture of 140 ml of water and 180 ml of ethanol for 10 minutes and then stirred for 10 minutes in a beaker. Then 0.5 g of CTAB was added to the above suspension; after that, 3 ml of ammonia was added and stirred for 30 minutes and then 2 ml of TEOS was added dropwise into the reaction mixture slowly for 10 minutes to reach the pH value of 11. Now the above suspension was stirred for 4 h at room temperature, and then the particles were washed with a mixture of water and ethanol and dried under vacuum.

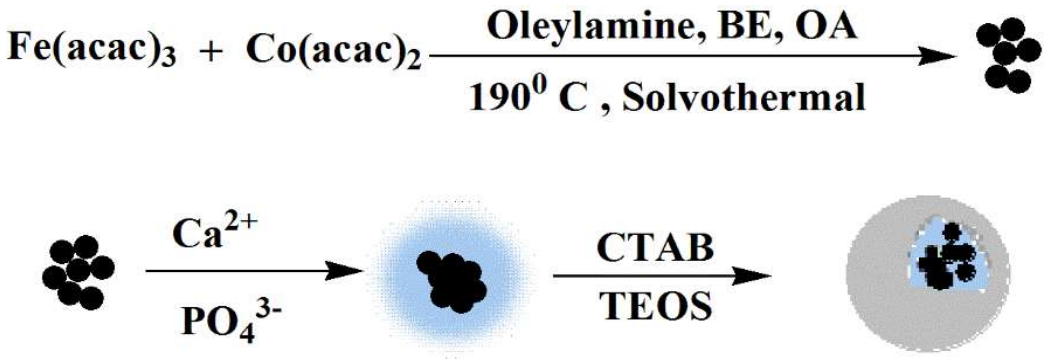

Fig. 5.1 Schematic presentation of the synthesis of $CoFe_2O_4$ encapsulated mesoporous hollow silica particles.

Synthesis of exterior aminopropyl grafted $CoFe_2O_4$@m-SiO_2 hollow nanoparticles

The selective grafting of the exterior surface of $CoFe_2O_4$@m-SiO_2 hollow particles was done by following the procedure reported by Lin et al.[40] $CoFe_2O_4$@-HAP@m-SiO_2 sphere nanocomposites (200 mg) were added to 30 ml dry toluene with 0.5 ml of aminopropyltrimethoxy silane (APTS) under refluxing under an N_2 atmosphere for 24 h (Fig. 5.2). The amine modified $CoFe_2O_4$@HAP@m-SiO_2 particles were washed with acidic ethanol to remove CTAB. The hydroxyapatite core was removed by immersing the composite nanoparticles in dilute acetic acid (HAC/H_2O = 1: 15) for 6 h. Finally the sample was dried in an oven at 65 °C. The sample is named $CoFe_2O_4$@m-SiO_2 hollow nanocapsules.

Iminodiacetic acid modified $CoFe_2O_4$@m-SiO_2 hollow mesoporous sphere nanoparticles.

The amine-modified $CoFe_2O_4$@m-SiO_2 hollow spheres were treated with a mixture of 30 ml ethanol and 20 ml triethylamine that contained excess amount of sodium chloroacetate at 80 °C for 48 h. The molar ratio of sodium chloroacetate and amine modified particles was 5:1. Then the final product was washed with water and ethanol, and then dried at 80 °C under vacuum.

Preparation of $CoFe_2O_4$@m-SiO_2–CDDP–FA

30 mg of cisplatin was taken in 10 ml of water, and 33 mg of $AgNO_3$ was added to it (Fig. 5.2). The solution was stirred at room temperature for 48 h in the dark. The white precipitate of AgCl was removed by centrifugation and didechlorinated CDDP [cis-diaquadiamino platinum(II)] was obtained in the supernatant. 120 mg of iminodiacetic acid functionalized $CoFe_2O_4$@m-SiO_2 nanoparticles were dispersed in the solution of CDDP and sonicated to give a suspension, which was stirred at 200 rpm for 48 h at 45 °C in dark after the pH was adjusted to 9 with NaOH (2 M). The obtained product was purified with a magnetic separator and washed with water for at least five times to remove the reductant CDDP. The marker molecule folic acid and RITC functionalized with $–NH_2$ groups (FA-NH_2 and RITC-NH_2) were conjugated in stoichiometric amounts through the remaining –COOH groups on the surface following our previously reported protocol.[41] Now the obtained magnetic hollow sphere, grafted with folic acid, RITC and the platinum pharmacophore CDDP on its exterior surface, still has enough free interior space which can be further utilized to load hydrophobic drugs.

Conversion of hydrophilic pemetrexed into hydrophobic form

Pemetrexed disodium salt (50 mg) was dissolved with 5 ml of water with stirring; one drop of conc. HCl was added and continuously stirred for 10 h. During

the reaction time a white precipitate came; after completion the white precipitate was filtered and dried.

Preparation of pemetrexed loaded into the hollow cavity of $CoFe_2O_4$@m-SiO_2@CDDP@-FA@RITC.

The nano-precipitation method was used to load the hydrophobic drugs into the hollow cavity of $CoFe_2O_4$@m-SiO_2@CDDP@-FA@RITC nanoparticles (Fig. 5.2). 50 mg of $CoFe_2O_4$@m-SiO_2@CDDP@-FA@RITC nanoparticles and 10 mg of hydrophobic pemetrexed were mixed with 5 ml of methanol solution and stirred for 2 h. 6 ml of water was then added dropwise into the suspension with stirring. The suspension was stirred under vacuum for 5 h until the methanol evaporated. The drug loaded particles pemetrexed@$CoFe_2O_4$@m-SiO_2@CDDP@-FA@RITC were collected by magnetic separation and washed with methanol repeatedly to remove the free drug. Finally, the drug loaded particles were dispersed in PBS buffer (pH 7.4). The drug concentration and loading capacity were calculated by measuring the visible absorbance at 274 nm for pemetrexed after the drugs were extracted from the hollow sphere by a mixture of ethyl acetate and water.

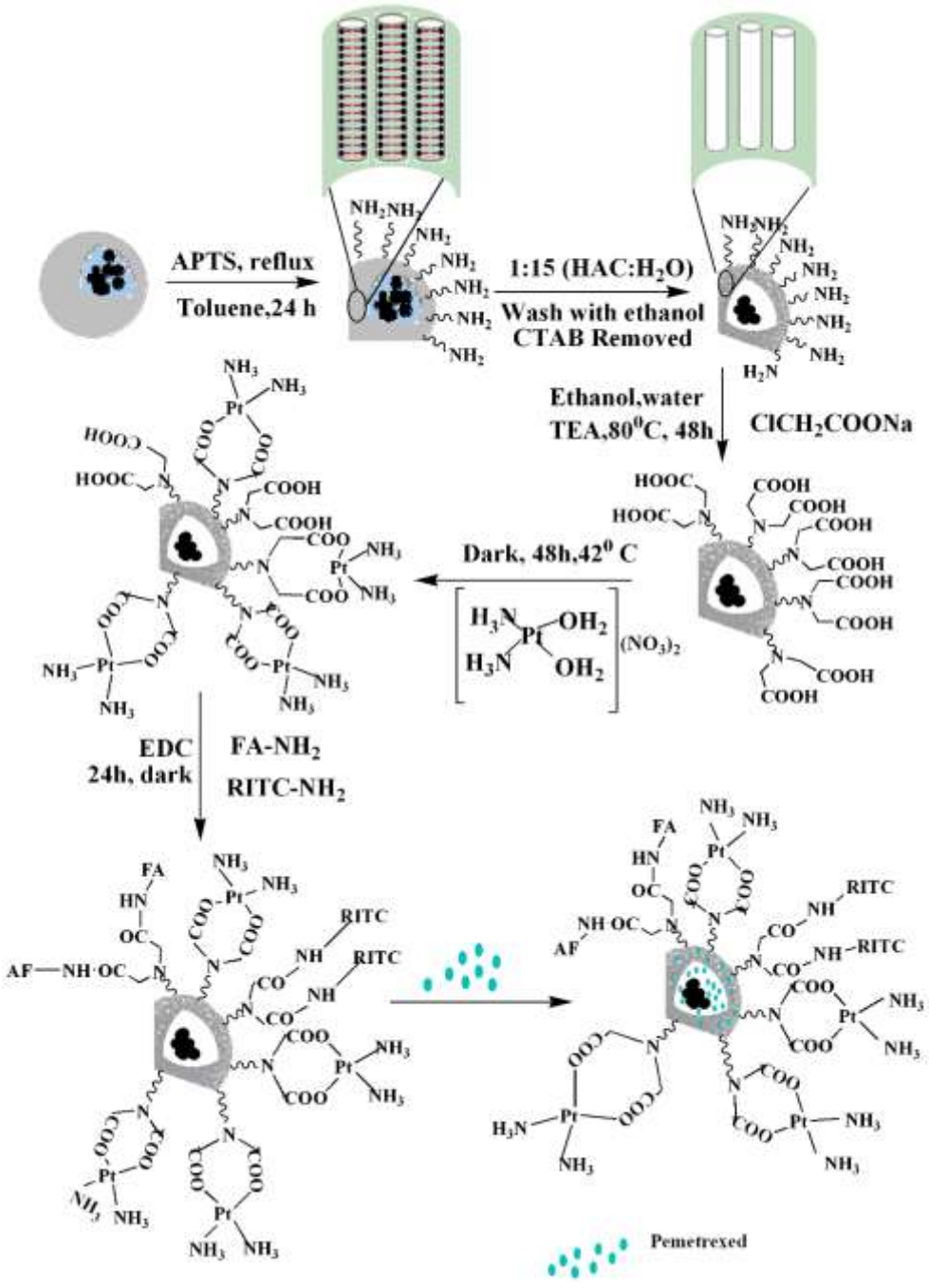

Fig. 5.2 The selective functionalization of the exterior surface of silica nanoparticles with iminodiacetic acid to conjugate platinum drugs, folic acid and RITC.

5.3. Characterization

The synthesized materials were well characterized by using standard techniques as described in chapter-3. The cytotoxicity and intracellular uptake experiments were performed following the protocol already described in chapter 3.

MR imaging

MRI contrast agents are a group of materials which are used to increase the visibility of the internal body structure in MRI. MRI contrast agents can alter the relaxation times of the atoms present in tissues where they are present. T_2 contrast agents are a class of contrast agents which can reduce the transverse relaxation time which can introduce negative contrast into the image. Superparamagnetic iron oxide nanoparticles were widely used as a T_2 contrast enhancing agent. The relaxation time (T_2) and transverse relaxivity (r_2) of the nanoparticles were measured with varying iron concentration (0.015–0.075 mM) using a clinical MRI scanner (MAGNETOM Symphony, SIEMENS) at a magnetic field of 1.5 T. T_2-weighted images were obtained with a spin echo multisection pulse sequence having a fixed repetition time (T_R) of 4000 ms with various echo times (T_E) ranging from 105 to 291 (105, 116, 128, 139, 151, 163, 174, 186, 198, 291). The spatial resolution parameters were as follows: field of view FOV = 300 × 300 mm2, matrix = 358 × 358, slice thickness = 4.0 mm. The MRI signal intensity (SI) was measured using in-built software. T_2 values were obtained by plotting the SI of each sample over a range of T_E values. T_2 relaxation times were then calculated by fitting a first-order exponential decay curve to the plot. The fitting equation can be expressed as:

$$SI = S_0 e^{-TE/T_2} + B$$

Where SI is the signal intensity, T_E is the echo time, S_0 is the amplitude, and B is the offset. The relaxivity value r_2 is determined from the slope of the linear plots of the relaxation rate R_2 ($1/T_2$, s^{-1}) against Fe concentrations (mM). Here, R_2^0 is regression coefficient of the plot.

$$R_2 = R_2^0 + r_2 [Fe]$$

5.4. Results and discussion

The synthetic strategy for hollow mesoporous silica spheres having magnetic $CoFe_2O_4$ inner particles has been shown in Fig. 5.1. Di-mercapto succinic acid (DMSA) coated $CoFe_2O_4$ nanoparticles were prepared from hydrophobic oleic acid capped $CoFe_2O_4$ nanoparticles by a simple phase transfer method.[43] Later this DMSA coated $CoFe_2O_4$ acts as a seed for the growth of hydroxyapatite. Crystal growth is promoted by a monolayer of DMSA bound to the surface of the $CoFe_2O_4$ nanoparticles; the carboxylate ions in DMSA are excellent binging sites for Ca^{2+} ions. Subsequently, the formation of m-SiO_2 on the surface of the $CoFe_2O_4$@HAP was performed by sol-gel method using CTAB template (Fig. 5.2). The as synthesized CTAB containing $CoFe_2O_4$@HAP@mSiO_2 was functionalized with $–NH_2$ by grafting by grafting an organoalkoxysilane, aminopropyltrimethoxysilane (APTMS), onto the exterior surfaces of these particles by refluxing in toluene. The resulting $–NH_2$ functionalized $CoFe_2O_4$@HAP@mSiO_2 particles were washed with water and recovered. Then CTAB and HAP were removed according to the procedure described in experimental section. HAP serves as a sacrificial template for the formation of hollow capsule which was utilised in accommodating another hydrophobic anticancer drug pemetrexed. The hollow $CoFe_2O_4$@mSiO_2 nanocapsules were further functionalized with iminodiacetic acid not only to hold platinum pharmacophore $Pt[OH_2](NH_3)_2$ but also to be used as a functional site for the attachment of marker molecule folic acid and fluorescent dye RITC.

XRD

In the wide angle XRD pattern of $CoFe_2O_4$/HAP (Fig. 5.3A), in addition to the reflection planes corresponding to the inverse spinel $CoFe_2O_4$ (JCPDS no. 22-1086), the lines corresponding to the reflection of the planes [002], [211], [130], [213], and [004] of hexagonal hydroxyapatite (JCPDS no. 72-1243) are prominent. In the case of

$CoFe_2O_4$/HAP@m-SiO_2, a broad peak in the range 2θ = 20°–30° was observed in addition to all the characteristic peaks of the $CoFe_2O_4$ and HAP. The absence of any HAP peak in the XRD pattern of $CoFe_2O_4$@m-SiO_2 and the retention of $CoFe_2O_4$ indicates that the HAP template has been completely removed after etching whereas magnetic $CoFe_2O_4$ nanoparticles still exist in the hollow sphere.

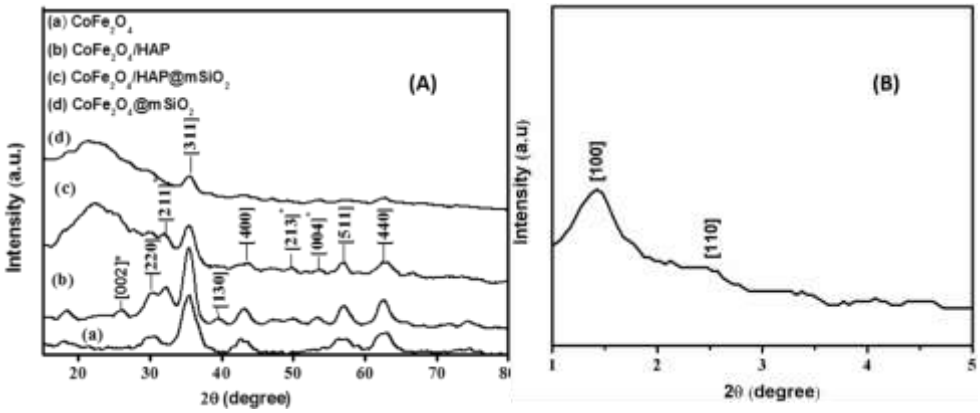

Fig. 5.3 (a) Wide angle diffraction pattern of $CoFe_2O_4$@m-SiO_2 hollow sphere at different stages of synthesis, (b) is the low angle XRD pattern of $CoFe_2O_4$@m-SiO_2 hollow spheres.

The mesoporous structure is indicated by low angle XRD. The low angle XRD pattern of the $CoFe_2O_4$@m-SiO_2 hollow spheres (Fig. 5.3B) shows well resolved peaks between 0.5 and 4° representing long range ordering. The peaks have d-spacing ratios corresponding to ordered 2D hexagonal mesostructure (p6mm).[44]

SEM and TEM

The SEM image presents well dispersed spherical hollow particles (Fig. 5.4a). TEM image of $CoFe_2O_4$@HAP@m-SiO_2 clearly shows the formation of spherical particles of size 120–150 nm with the interior cavity crowded with $CoFe_2O_4$ and HAP nanoparticles. After etching with acidic ethanol, the interior HAP particles were completely removed, leading to a hollow sphere (Fig. 5.4b) with the shell thickness of 30 nm. The hollow capsule with ample inner space and a robust as well as chemically stable Si–O–Si structured shell opens up the possibility for a wide range of applications. The magnified image of one capsule shows inclusion of an uneven

number of $CoFe_2O_4$ nanoparticles in its interior cavity. However, still a profitable space is left for the accommodation of therapeutic cargoes. The high resolution image clearly shows the lattice fringes of [220] and [111] crystalline planes of the inverse spinel $CoFe_2O_4$. EDX analysis shows that the atomic ratio of Si:Ca of 20:10 as found in precursor $CoFe_2O_4$@HAP@m-SiO_2 nanoparticles appreciably decreases to 50 : 1 indicating complete erosion of the HAP template.

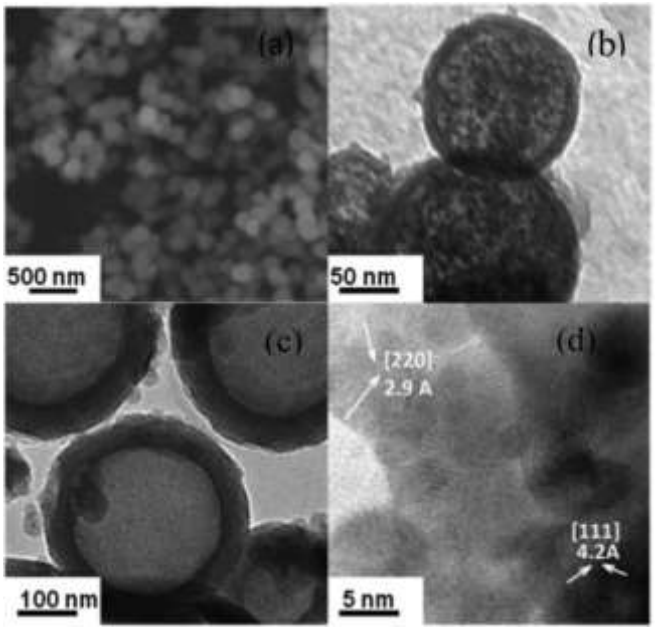

Fig. 5.4 (a) SEM image of $CoFe_2O_4$@m-SiO_2, (b) TEM image of $CoFe_2O_4$@m-SiO_2, (c) image at high magnification, (d) Image showing a single hollow capsule having inner $CoFe_2O_4$ particles..

Nitrogen adsorption-desorption study

A comparison of N_2 adsorption–desorption isotherms of $CoFe_2O_4$@HAP@m-SiO_2 and $CoFe_2O_4$@m-SiO_2 has been presented in Fig. 5.5A. Both the samples reveal type IV isotherms. In the case of $CoFe_2O_4$@m-SiO_2 hollow spheres, a very large hysteresis loop exists at P/P_0 of 0.3 to 0.4 which is indicative of the mesoporosity produced by the ion exchange process.[45] The BET surface area of the as synthesized $CoFe_2O_4$@HAP@m-SiO_2 nanospheres is found to be 297 m^2 g^{-1} which appreciably increases to 542 m^2 g^{-1} after removal of the HAP template. The pore size of the

hollow capsule has been calculated using BJH and is found to be 7.2 nm (Fig. 5.5B). The unique structures of the hydrophilic nanospheres with their mesostructured pore walls and the hollow cavities are ideal for small molecules delivery.

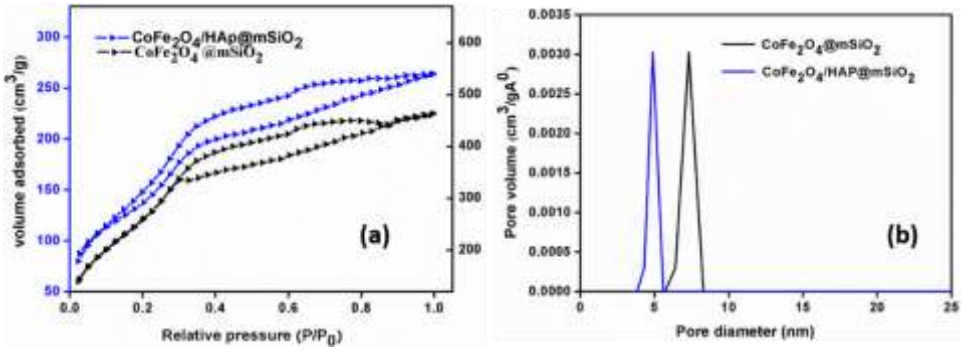

Fig. 5.5 (A) N_2 adsorption isotherm and (B) Pore size distribution of $CoFe_2O_4$@m-SiO_2 and $CoFe_2O_4$@HAP@m-SiO_2.

FTIR

The comparison of FTIR (Fig. 5.6) spectra at different stages of synthesis clearly establishes the functionalization of the hollow sphere with pemetrexed and CDDP. The strong absorption bands near 500–600 cm^{-1} are due to the M–O stretching in the ferrite nanoparticles. The peak centered at 1080 and 794 cm^{-1} corresponds to asymmetric and symmetric stretching vibrations of the Si–O–Si bond respectively. A broad prominent peak at 3400 cm^{-1} clearly shows the presence of hydroxyl groups or physically adsorbed water on the surface of $CoFe_2O_4$@m-SiO_2 hollow particles. After APTS modification on the surface of $CoFe_2O_4$@m-SiO_2, the peaks at 1640 cm cm^{-1} and 1480 cm cm^{-1} correspond to N–H bending and C–N stretching of amine functionalized $CoFe_2O_4$@m-SiO_2. In addition to N–H bond vibration there are two other peaks centered at 2923 cm^{-1} and 2857 cm^{-1} corresponding to asymmetric and symmetric stretching vibrations of methylene protons. In the case of iminodiacetic acid modified particles the appearance of a strong asymmetric stretching band near 1635 cm^{-1} and a weaker symmetrical stretching band near 1400 cm^{-1} corresponds to the C–O bond of the carboxylate ion.

After the conjugation of folic acid through carbodiimide, bands in the range of 1680 to 1410 cm^{-1} appeared. The appearance of two prominent characteristic bands at 1680 (amide I) and 1514 (amide II) cm^{-1} indicates that folic acid has been conjugated to $CoFe_2O_4$@m-SiO_2 nanoparticles through amide linkage. The high resolution XPS scan shows two peaks centered at 76.75 and 79.7 eV for Pt4f7/2 and Pt4f5/2 respectively.

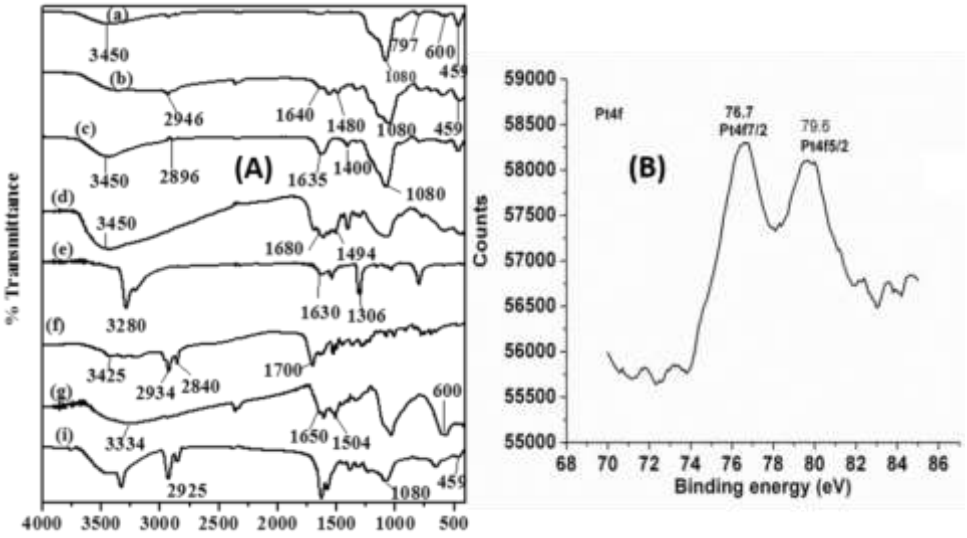

Fig. 5.6 (A) FTIR at various stages of synthesis: (a) $CoFe_2O_4$@m-SiO_2 hollow spheres, (b) $CoFe_2O_4$@m-SiO_2@APTS, (c) $CoFe_2O_4$@m-SiO_2@IDA, (d) $CoFe_2O_4$@m-SiO_2@IDA-FA, (e) CDDP, (f) pemetrexed in acid form, (g) pemetrexed encapsulated $CoFe_2O_4$@m-SiO_2@IDA-FA, (h) pemetrexed@$CoFe_2O_4$@m-SiO_2@IDA-FA@CDDP dual drug nanoparticles , (B) High resolution XPS scan of pemetrexed@$CoFe_2O_4$@m-SiO_2@IDA-FA@CDDP showing Pt peaks.

Magnetic measurement

Field dependent magnetization curves of both precursors $CoFe_2O_4$@HAP@m-SiO_2 and $CoFe_2O_4$@m-SiO_2 nanocapsules show no coercivity and hence is superparamagnetic at room temperature (Fig. 5.7). The saturation magnetization values are found to be 20 and 59 e.m.u. g^{-1} respectively at high magnetic field (2 T). The substantial increase in saturation magnetization is attributed to the removal of nonmagnetic HAP in the etching process. The HAP coating screens and decreases the

magnetic coupling interaction between neighboring $CoFe_2O_4$ nanoparticles. However, the high saturation magnetization along with superparamagnetism is highly desirable for application of the synthesized hollow spheres in magnetically guidable drug delivery and as a contrast enhancing agent in MRI.

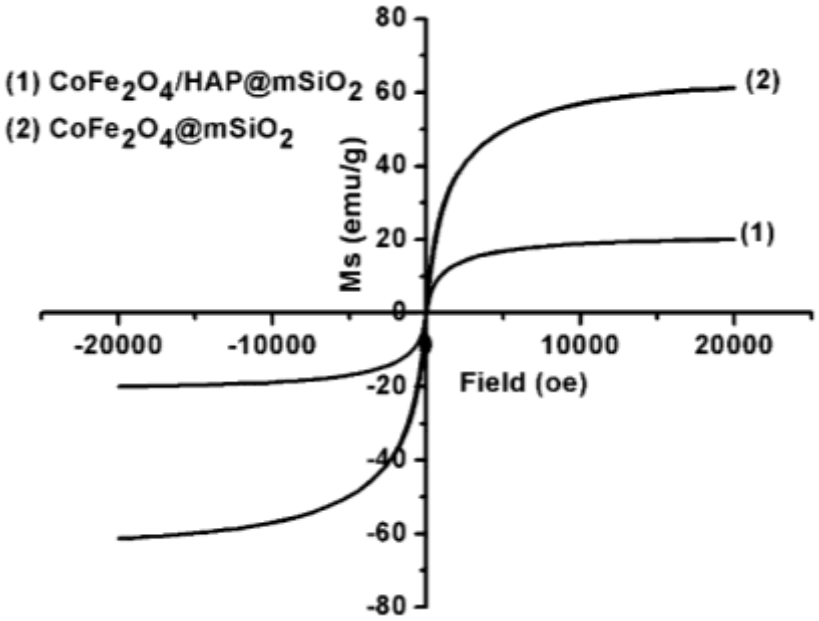

Fig. 5.7 Comparison of magnetisation curves of $CoFe_2O_4$@$mSiO_2$ and $CoFe_2O_4$@HAP@$mSiO_2$ at room temperature.

Magnetic Resonance Imaging (MRI)

To verify the potential imaging applications of the synthesized magnetic mesoporous hollow spheres we further carried out relaxometric measurements with a MRI scanner (1.5 T). The relaxivity coefficient was determined from the slope of the 1/T2 vs. metal ion plot and found to be 421 mM^{-1} s^{-1} (Fig. 5.8a). With increasing concentration of $CoFe_2O_4$@m-SiO_2 in the phantom solution the signal intensity decreased, showing that the particles have generated magnetic resonance contrast (Fig. 5.8b). The transverse relaxivity coefficient is higher than that for the commercially available iron oxide based contrast agents such as ferumoxytol (91 mM^{-1} s^{-1}) and feridex (120 mM^{-1} s^{-1}). However, the relaxivity value is consistent with the r_2 values for $CoFe_2O_4$ as reported by other groups.[46–49] The higher value of r_2 is attributed to the high saturation magnetization of $CoFe_2O_4$ nanoparticles. All these results point out that due to higher transverse relaxivity this dual drug loaded hollow capsules will have a better negative contrast effect than commercially available iron oxide based MRI contrast agents.

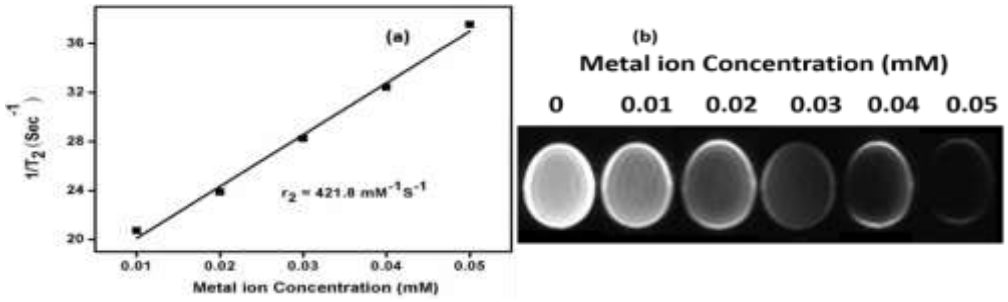

Fig. 5.8 (a) Relaxivity (r_2) measurement and (b) MR phantom images of pemetrexed@$CoFe_2O_4$@mSiO_2-FA-CDDP in water.

Hydrodynamic size and zeta potential measurement

The surface modification processes were further verified by investigating surface charge properties. The iminodiacetic acid modified particles showed a zeta potential of −30 mV at neutral pH which increases to −45.4 mV with an increase in

pH, indicating the transformation of the carboxylic acid group of the iminodiacetic acid into a carboxylate anion. The hydrodynamic size of the functionalized nanoparticles after each step of the synthesis has been presented in Fig. 5.9. The HD size increases after each step of modification indicating addition of one molecular layer. The size of the final dual drug loaded particles is 85 nm with polydispersity index PDI < 0.5. The HD size increases to 40% after 4 weeks. However, PDI and zeta potential remain almost unchanged over a long period demonstrating the suitability of this dual drug capsule in practical applications.

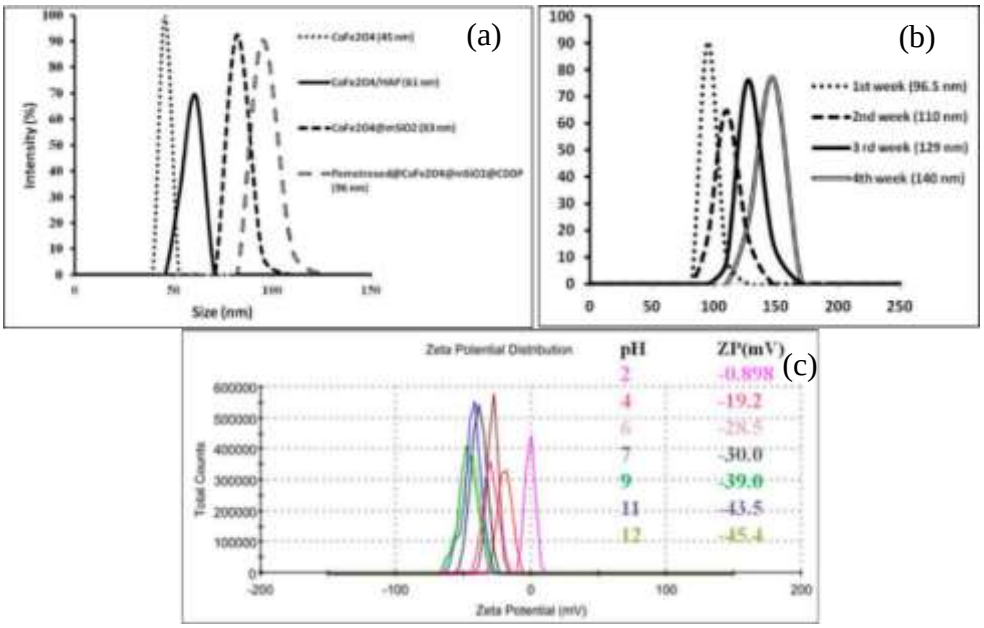

Fig. 5.9 (a) HD sizes at different stage of modification (b) Stability of particles with Pemetrexed@$CoFe_2O_4$@$mSiO_2$@IDA-FA@CDDP after several weeks. (c) Zeta potential of Pemetrexed@$CoFe_2O_4$@$mSiO_2$@IDA-FA@CDDP over different pH.

Loading capacity and pH dependent drug release

To demonstrate the material's potential use as a drug delivery system, the drug loading capacity of the capsules was investigated by stirring it with respective drug solutions (1.0 mg ml^{-1}). The percentages of CDDP and pemetrexed adsorbed on

the $CoFe_2O_4$@m-SiO_2 hollow capsules are 76% and 64% respectively (Fig. 5.10 a). The cumulative releases of both CDDP and pemetrexed were found to increase with a decrease in environmental pH. In all pHs CDDP showed a burst release followed by a sustained release pattern (Fig. 5.10 b). Particularly at pH 4.5, a burst release of 45% of CDDP was observed from the hollow capsules in the first 20 h which was reduced to 10% as the pH was increased to 7.4. CDDP is bonded to the nanoparticles surface through covalent coordinate bonds by the interaction of –COOH groups of the iminodiacetic acid on the nanoparticles surface with Pt (II). The bonding of –COOH to Pt is well established in the literature and supported by a decrease in carbonyl stretching frequency in the IR spectra. This type of bonding is acid sensitive and is cleavable at low pH. In our case a distinctly prolonged and pH-responsive release of therapeutic platin is observed which is very similar to the release profile of platin from dumb bell-like Au–Fe_3O_4 nanoparticles, where the platin complex was anchored on the Au-side by reacting Au–S-$CH_2CH_2N(CH_2COOH)_2$ with cisplatin,[54] in the case of high density surface carboxylic groups grafted on mesoporous silica,[55] and also in our previously designed mesoporous calcium phosphate for the delivery of cisplatin where the CDDP was adsorbed on the calcium phosphate surface through surface iminodiacetate groups.[51] This indicates that the presence of pemetrexed did not significantly affect the release of CDDP in the dual delivery system.

In the case of the hydrophobic drug pemetrexed, the release from the functionalized multidrug capsule is triggered when the environmental pH value was decreased similarly to the release behavior of pemetrexed from mesoporous silica particles. The significant pH-dependent release observed for pemetrexed may be mainly due to the change in the ionization state of the molecule and the subsequent interaction with the silica surface. Pemetrexed is a polyelectrolyte carrying two carboxyl groups, with pKa of 3.46 (α-carboxyl) and 4.77 (γ-carboxyl), and the guanidinic N-1 on the pterine ring (pKa 5.27).[56] At physiological pH, pemetrexed exists in a predominantly negatively charged form due to the deprotonation of the two carboxyl groups. When the pH decreased from 7.4 to 5.5, there is negligible change in

the ionization of carboxyl groups (i.e., from 99% to 97%), but a marked increase in the calculated ionization of nitrogen groups (i.e., from 0% to 30%) in water. It is possible that at acidic pH (4.5–5.5) the enhanced positive potential of the inner silica surface weakens the electrostatic interaction between the positively charged pemetrexed leading to a faster release. Thus, both the releases can occur across the range of pH found in intracellular lysosomes (4–5) or the local environment of some cancerous tissues, thereby enabling targeted therapeutic capacity by passive release at the pathologically relevant sites in addition to active targeting through the folate receptor.

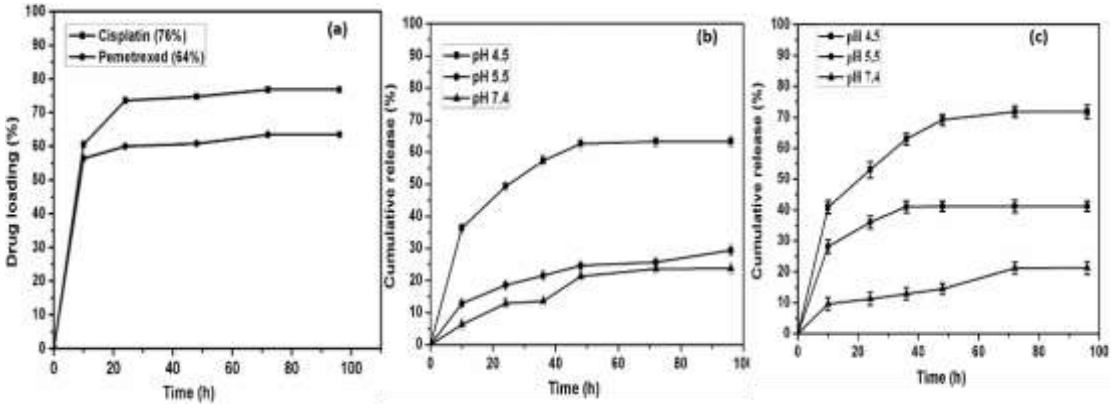

Fig. 5.10 (a) Percentage of drug loading with time, drug release profile over time at different pH: (b) Cisplatin, (b) Pemetrexed.

Calculation of drug loading content and encapsulation efficiency

For cisplatin

$$\text{Drug loading content (\%)} = \frac{Weight\ of\ the\ drug\ in\ nanoparticles}{Weight\ of\ the\ nanoparticles} \times 100$$

$$= \frac{0.024}{0.140} \times 100$$

$$= 17.14\%$$

Encapsulation efficiency (%) = $\frac{Weight\ of\ the\ drug\ in\ nanoparticles}{Weight\ of\ the\ feeding\ drug} \times 100$

$= \frac{0.024}{0.030} \times 100$

$= 80\%$

For Pemetrexed

Drug loading content (%) = $\frac{Weight\ of\ the\ drug\ in\ nanoparticles}{Weight\ of\ the\ nanoparticles} \times 100$

$= \frac{0.008}{0.140} \times 100$

$= 5.71\%$

Encapsulation efficiency (%) = $\frac{\text{Weight of the drug in nanoparticles}}{\text{Weight of the feeding drug}} \times 100$

$= \frac{0.008}{0.013} = 61.53\%$

Both cis-Platin and Pemetrexed

Drug loading content (%) = $\frac{Weight\ of\ the\ drug\ in\ nanoparticles}{Weight\ of\ the\ nanoparticles} \times 100$

$= \frac{0.032}{0.140} \times 100$

$= 22.85\%$

Encapsulation efficiency (%) = $\frac{Weight\ of\ the\ drug\ in\ nanoparticles}{Weight\ of\ the\ feeding\ drug} \times 100$

$= \frac{0.032}{0.038} \times 100 = 84.21\%$

Cytotoxicity

The biocompatibility of the carrier is a key factor in evaluating the potential of the drug delivery systems. It has been already reported that mesoporous silica based nanocapsules do not show any cytotoxicity or show very low cytotoxicity.[50] Our synthesized $CoFe_2O_4$@m-SiO_2 hollow capsules showed more than 85% cell viability against HeLa cells, HaCat and mouse fibroblast 3T3 cells. In contrast, pemetrexed@$CoFe_2O_4$@m-SiO_2–FA–CDDP particles showed remarkably high cytotoxicity (Fig. 5.11). Also the cytotoxic effect of folate modified dual drug loaded particles was compared with the free drugs cisplatin, pemetrexed and the dual drug loaded nanocapsule. The results indicate that the cytotoxicity of the dual cargo loaded capsule is significantly enhanced compared to individual free drugs. In addition to this, the toxic effect was further increased when the capsule was modified with marker molecules such as folic acid as observed in our previously reported cases.[51–53]

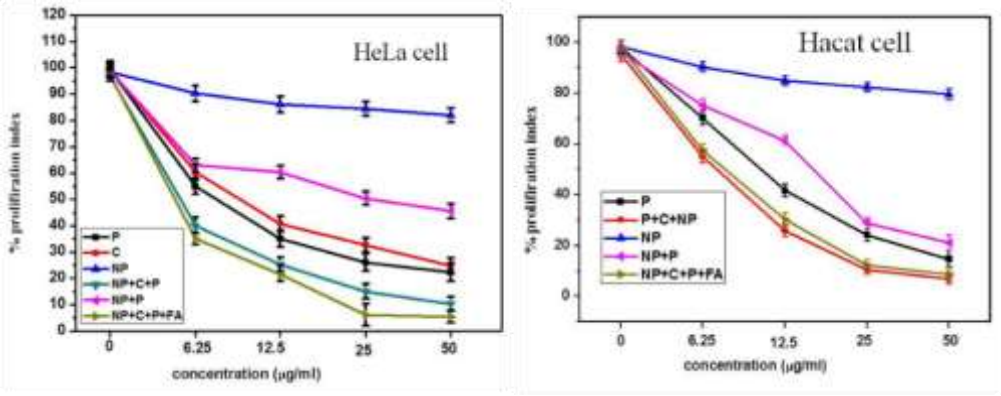

Fig. 5.11 MTT assay of the dual drug loaded hollow capsule with HeLa cells and HaCaT cells. In the legends, P – pemetrexed, C – cisplatin, NP – as prepared $CoFe_2O_4$@m-SiO_2 hollow spheres, FA – folic acid.

Cellular uptake

In vitro cellular uptake of pemetrexed@$CoFe_2O_4$@m-SiO_2– FA–CDDP nanocapsules by the folate receptor overexpressed HeLa (FR+ve) cells was investigated using fluorescence microscopy. Cells incubated with pemetrexed@$CoFe_2O_4$@m-SiO_2–FA–CDDP–RITC nanocapsules for 60 min

endocyted the capsules as evidenced by the intense red fluorescence signal coming from RITC. With the increase of time the red luminescence in the cytoplasm was increased leaving a clear nuclear zone (Fig. 5.12). In contrast, no such increase in RITC signal was observed in the case of pemetrexed@$CoFe_2O_4$@m-SiO_2–CDDP–RITC nanoparticles. Additionally, when pemetrexed@Co-Fe_2O_4@m-SiO_2–FA–CDDP–RITC was incubated with FR(−ve) HaCat cells no such time dependent increase in the RITC signal was observed. This clearly indicates that the dual drug loaded nanocapsules are selectively targeted to the folate receptor overexpressed HeLa cells.

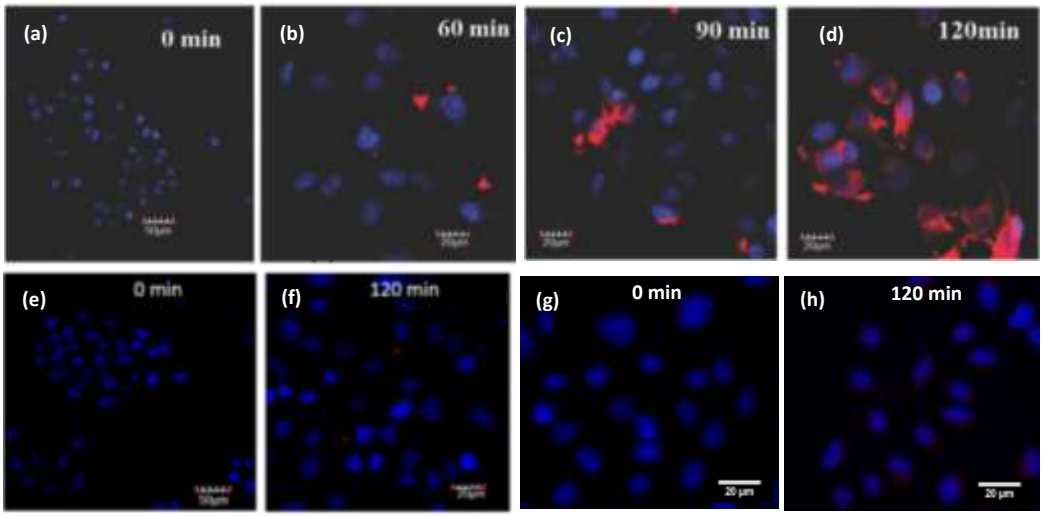

Fig. 5.12 Fluorescence images showing intracellular uptake of (a) to (d) pemetrexed@$CoFe_2O_4$@m-SiO_2–FA–CDDP–RITC nanospheres by HeLa cells, (e) and (f) HaCat cells and (g) and (h) Fluorescence image of pemetrexed@$CoFe_2O_4$@m-SiO_2–CDDP–RITC in HeLa cells.

Cell apoptosis

The internalization of drug capsules results in cell death or apoptosis. The cell breaks apart into several vesicles called apoptotic bodies. To verify the rampant chromatin condensation and apoptotic body formation, the cell nuclei were further stained with 4′-6-diamidino-2-phenylindole (DAPI), a nuclear staining dye, known to

exhibit strong blue fluorescence when bound to DNA. It was observed that the capsules loaded with both pemetrexed and cisplatin show better apoptotic features than capsules loaded with individual drugs (Fig. 5.13).

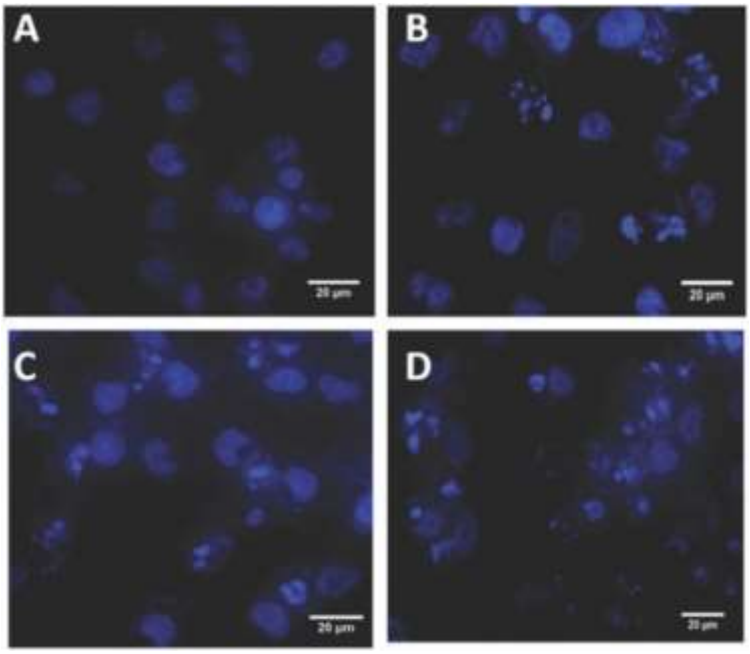

Fig. 5.13 DAPI fluorescence (200×) images of HeLa cells incubated with (A) PBS, (B) 1.5, (C) 3.0, (D) 6.0 μg mL^{-1} pemetrexed@$CoFe_2O_4$@m-SiO_2–FA–CDDP nanospheres

A quantitative evaluation of dual drug loaded capsule mediated apoptosis was investigated by fluorescence activated cell sorting (FACS) or fluorescence flow cytometry. It is a laser based, biophysical technology employed in cell counting and cell sorting by suspending cells in a stream of fluid and passing them through an electronic detection apparatus. It allows fluorescence analysis of up to thousands of particles per second based upon the specific light scattering and fluorescence characteristics of each cell. It is observed that both cisplatin and pemetrexed cause apoptosis in HeLa cells to a similar extent (M1). However, cisplatin arrests the cell cycle at the S phase (or synthesis phase when replication of DNA starts) as reported in the case of cisplatin,[57,58] and promotes cells towards apoptosis whereas pemetrexed does not allow cells to go to the S phase and promotes the cells towards apoptosis by

arresting them at the G1 phase (it is the first of the four phases of the cell cycle that takes place in eukaryotic cell division, after G1 phase comes to S phase) in accordance with the earlier reported results with pemetrexed conjugated nanoparticles.[59] However with dual drug loaded nanocapsules (pemetrexed@$CoFe_2O_4$@m-SiO_2–FA–CDDP) apoptotic population increases in a dose dependent manner. According to the flow cytometry data, it may be inferred that, at lower concentration of our multidrug loaded nanocapsules, the cells are arrested at the S-phase and then apoptosis starts whereas, at higher concentration, cells go to apoptosis from the G1 phase without entering the S-phase. The arrest is responsible for appreciable morphological changes as monitored by fluorescence microscopy that eventually resulted in cell death.

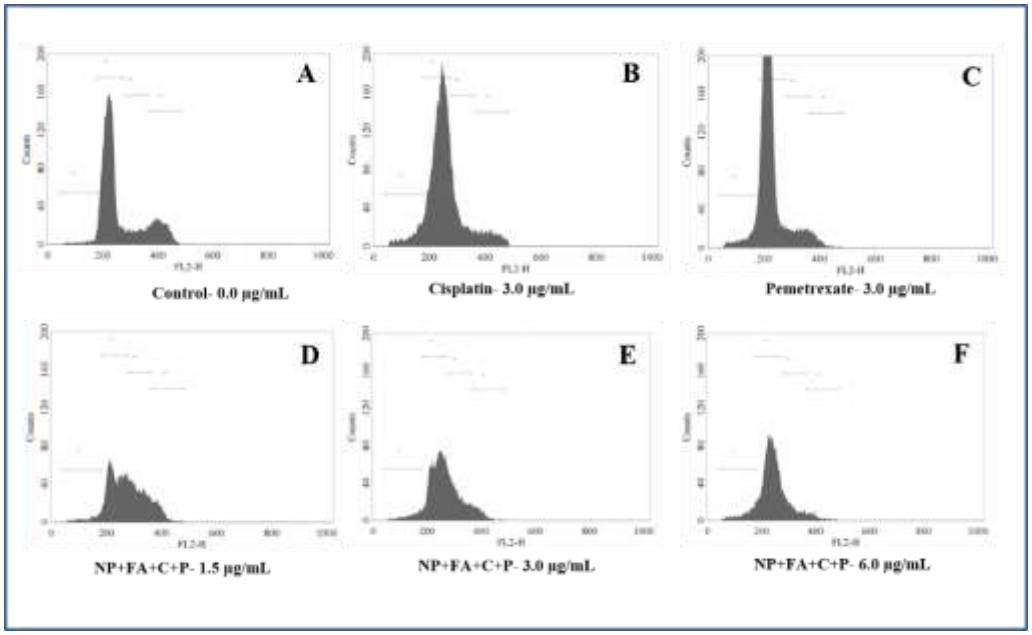

Fig. 5.14 Flow cytometric analysis of the cell cycle phase distribution in HeLa cells.

5.5. Conclusion

We report the synthesis of mesoporous hollow spherical silica nanoparticles with a size of 130 nm using the calcium phosphate template. The internal space of

hollow spheres was utilized to cluth the hydrophobic anticancer drug pemetrexed and superparamagnetic $CoFe_2O_4$ nanoparticles while the external surface was chemically modified to grasp the platinum pharmacophore CDDP [cis-diaquadiamino platinum (II)], the marker molecule folic acid and the fluorescent dye RITC.The combined advantages of enhanced therapeutic efficacy due to drug synergism, site specific targeting through folate receptor mediated endocytosis, fluorescence properties and T2 contrast enhancement in MRI make these multifunctional nanoparticles a suitable platform for cancer treatment and further exploration in pharmaceutical industries.

5.6. References

1. J. Lee, H. Kim, S. Kim, H. Lee, J. Kim, N. Kim, J. H. Park, E. K. Choi, J. S. Lee and C. Kim, *J. Mater. Chem.*, 2012, **22**, 1401.
2. E. C. Dreaden, M. A. Mackey, X. Huang, B. Kang and M. A. El-Sayed, *Chem. Soc. Rev*., 2011, **40**, 3391.
3. J. R. McCarthy, *Adv. Drug Delivery Rev*., 2010, **62**, 1023.
4. P. Zrazhevskiy, M. Sena and X. Gao, *Chem. Soc. Rev*., 2010, **39**, 4326.
5. J. L. Vivero-Escoto, I. I. Slowing, B. G. Trewyn and V. S. Y. Lin, *Small*, 2010, **6**, 1952.
6. I. I. Slowing, J. L. Vivero-Escoto, C. W. Wu and V. S. Y. Lin, *Adv. Drug Delivery Rev*., 2008, **60**, 1278.
7. L. Chen, J. Di, C. Cao, Y. Zhao, Y. Ma, J. Y. Luo, W. Wen, Y. Song and L. A. Jiang, *Chem. Commun*., 2011, **47**, 2850.
8. L. Chen, Y. Wen, B. Su, J. Di, Y. Song and L. Jiang, *J. Mater. Chem*., 2011, **21**, 13811.
9. M. Z. Bulatović, D. Maksimović-Ivanić, C. Bensing, S. Gmez-Ruiz, D. Steinborn, H. Schmidt, M. Mojić, A. Korać, I. Golić, D. Pérez-Quintanilla, M. Momčilović, S. Mijatović and G. N. Kaluđerović, *Angew. Chem., Int. Ed*., 2014, **53**, 5982.
10. G. N. Kaluđerović, D. Pérez-Quintanilla, Ž. Žižak, Z. D. Juranić and S. Gómez-Ruiz, *Dalton Trans*., 2010, **39**, 2597.
11. A. García-Peñas, S. Gómez-Ruiz, D. Pérez-Quintanilla, R. Paschke, I. Sierra, S. Prashar, I. del Hierro and G. N. Kaluđerović, *J. Inorg. Biochem*., 2012, **106**, 100.
12. G. N. Kaluđerović, D. Pérez-Quintanilla, I. Sierra, S. Prashar, I. del Hierro, Ž. Žižak, Z. D. Juranić, M. Fajardo and S. Gómez-Ruiz, *J. Mater. Chem*., 2010, **20**, 806.

13. D. Pérez-Quintanilla, S. Gómez-Ruiz, Ž. Žižak, I. Sierra, S. Prashar, I. del Hierro, M. Fajardo, Z. D. Juranić and G. N. Kaluđerović, *Chem – Eur. J.*, 2009, **15**, 5588.
14. J. Ceballos-Torres, P. Virag, M. Cenariu, S. Prashar, M. Fajardo, E. Fischer-Fodor and S. Gómez-Ruiz, *Chem – Eur. J.*, 2014, **20**, 10811.
15. Y. F. Zhu, T. Ikoma, N. Hanagata and S. Kaskel, *Small.*, 2010, **6**, 471.
16. Y. Chen, H. R. Chen, L. M. Guo, Q. J. He, F. Chen, J. Zhou, J. W. Feng and J. L. Shi, *ACS Nano*, 2010, **4**, 529.
17. J. Kim, J. E. Lee, J. Lee, J. H. Yu, B. C. Kim, K. An, Y. Hwang, C. H. Shin, J. G. Park, J. Kim and T. Hyeon, *J. Am. Chem. Soc*., 2006, **128**, 688.
18. M. Rosenholm, E. Peuhu, J. E. Eriksson, C. Sahlgren and M. Linden, *Nano Lett*., 2009, **9**, 3308.
19. J. Lu, M. Liong, Z. X. Li, J. I. Zink and F. Tamanoi, *Small*, 2010, **6**, 1794.
20. Q. J. He, J. M. Zhang, J. L. Shi, Z. Y. Zhu, L. X. Zhang, W. B. Bu, L. M. Guo and Y. Chen, *Biomaterials*, 2010, **31**, 1085.
21. H. Wu, S. Zhang, J. Zhang, G. Liu, J. Shi, L. Zhang, X. Cui, M. Ruan, Q. He and W. Bu, *Adv. Funct. Mater*., 2011, **21**, 1850.
22. W. R. Zhao, H. R. Chen, Y. S. Li, L. Li, M. D. Lang and J. L. Shi, *Adv. Funct. Mater*., 2008, **18**, 2780.
23. T. Chen, N. Yang and J. Fu, *Chem. Commun*., 2013, **49**, 6555.
24. A. P. R. Johnston and F. Caruso, *Angew. Chem., Int. Ed*., 2007, **46**, 2677.
25. C. S. Peyratout and L. Dähne, *Angew. Chem., Int. Ed*., 2004, **43**, 3762.
26. P. S. Ga Yang and J. Lin, *Chem. Soc. Rev*., 2012, **41**, 3679.
27. J. Zhou, W. Wu, D. Caruntu, M. H. Yu, A. Martin, J. F. Chen, C. J. O. Connor and W. L. Zhou, *J. Phys. Chem. C*, 2007, **111**, 17473.
28. Y. Chen, H. Chen, L. Guo, Q. He, F. Chen, J. Zhou, J. Feng and J. Shi, *ACS Nano*, 2009, **4**, 529.
29. M. Yoon, Y. Kim and J. Cho, *ACS Nano*, 2011, **5**, 5417.
30. C. Bae, H. Kim, D. Han, H. Yoo, J. Kim and H. Shin, *Small*, 2009, **5**, 1936.

31. C. M. J. Hu and L. Zhang, *Biochem. Pharmacol*., 2012, **83**, 1104.
32. T. O. Harasym, P. G. Tardi, N. L. Harasym, P. Harvie, S. A. Johnstone and L. D. Mayer, *Oncol. Res*., 2007, **16**, 361.
33. R. K. Gudar, Ther. Clin. *Risk Manage*., 2008, **4**, 205.
34. A. R. Hanauske, V. Chen, P. Paoletti and C. Niyikiza, *Oncologist*, 2001, **6**, 363.
35. T. Min, H. Ye, P. Zhang, J. Liu, C. Zhang, W. Shen, W. Wang and L. Shen, *J. Appl. Polym. Sci*., 2009, **111**, 444.
36. Y. Zhang and A. L. Ann, *Pharmacotherapy*, 2006, **40**, 1082.
37. M. Vandana and S. K. Sahoo, *Mol. Pharm*., 2012, **9**, 2828.
38. C. Müller, J. A. Reddy, C. P. Leamon and R. Schibli, *Mol. Pharm*., 2010, **7**, 597.
39. A. O. Saeed, J. P. Magnusson, E. Moradi, M. Soliman, W. Wang, S. Stolnik, K. J. Thurecht, S. M. Howdle and C. Alexander, *Bioconjugate Chem*., 2011, **22**, 156.
40. J. L. Vivero-Escoto, I. I. Slowing and V. S. Y. Lin, *Biomaterials*, 2010, **31**, 1325.
41. S. Mohapatra, S. K. Mallick, T. K. Maiti, S. K. Ghosh and P. Pramanik, *Nanotechnology*, 2007, **18**, 385102.
42. S. Maiti, S. K. Bhutia, S. K. Mallick, A. Kumar, N. Khargi and T. K. Maiti, *Environ. Toxicol. Pharmacol.*, 2008, **26**, 187.
43. M. Songa, Y. Zhanga, S. Hua, L. Songa, J. Donga, Z. Chenb and N. Gua, *Colloids Surf., A*, 2012, **408**, 114.
44. *Handbook of Applied Surface and Colloid Chemistry, J. and Sons*, 2001, 330.
45. F. Zhang, Y. Shi, X. Sun, D. Zhao and G. D. Stucky, *Chem. Mater*., 2009, **21**, 5237.
46. H. M. Joshi, Y. P. Lin, M. Aslam, P. V. Prasad, E. A. S. Sikma, R. Edelman, T. Meade and V. P. Dravid, *J. Phys. Chem. C*, 2009, **113**, 17761.

47. S. Kuckelhaus, S. C. Reis, M. F. Carniero, A. C. Todesco, D. M. Oliveira, E. C. D. Lima and P. C. Morais, *J. Magn. Magn. Mater.*, 2004, **272**, 2402.
48. J. Kang, H. Lee, Y. N. Kim, A. Yeom, H. Jeong, Y. T. Lim and K. S. Hong, *Nanoscale Res. Lett.*, 2013, **8**, 376.
49. M. Nidhin, S. S. Nazeer, R. S. Jayasree, M. Kiran, B. U. Nair and K. J. Sreeram, *RSC Adv*., 2013, **3**, 6906.
50. Y. Zhao, L. N. Lin, Y. Lu, S. F. Chen, L. Dong and S. H. Yu, *Adv. Mater.*, 2010, **22**, 5255.
51. S. R. Rout, B. Behera, T. K. Maiti and S. Mohapatra, *Dalton Trans*., 2012, **41**, 10777.
52. S. Mohapatra, S. R. Rout, S. Maiti, T. K. Maiti and A. B. Panda, *J. Mater. Chem.*, 2011, **21**, 9185.
53. S. Sahu and S. Mohapatra, *Dalton Trans*., 2013, **42**, 2224.
54. C. Xu, B. Wang and S. Sun, *J. Am. Chem. Soc*., 2009, **131**, 4216.
55. J. Gu, S. Su, Y. Li, Q. He, J. Zhong and J. Shi, *J. Phys. Chem. Lett.*, 2010, **1**, 3446.
56. L. Li, Y. Y. Sham, Z. Bikadi and W. F. Elmquist, *Drug Metab. Dispos*., 2011, **19**, 1478.
57. G. Zhu and S. J. Lippard, *Biochemistry.*, 2009, **48**, 4916.
58. X. Pan, M. Wilson, L. Mirbahai, C. McConville, T. N. Arvanitis, J. L. Griffin, R. A. Kauppinen and A. C. Peet, *J. Proteome Res*., 2011, **10**, 3493.
59. T. Li, Y. H. Ling, I. D. Goldman and R. Perez-Soler, *Clin. Cancer Res*., 2007, **13**, 3413.

Chapter-6

Synthesis of luminescent magnetic mesoporous carbon nanosphere for the delivery of doxorubicin and MR imaging

6.1. Introduction

Development of drug encapsulated nanoparticles that effectively detect and treat malignancy is an emerging area in the field of nanobiotechnology.[1] In this regard, increasing attention has been paid to mesoporous nanoparticles due to their open-framework structure, large surface area and well-defined mesoporosity, which make them greatly interesting and potentially useful as a drug carrier and control release system.[2-7] Especially mesoporous silica nanoparticles are widely used as drug carriers due to their large pore volume,[8] high surface area,[9] ease of functionalization,[10] biodegradability[11] and generally low cytotoxicity.[12] MSNs with a diameter below 200 nm can be effectively internalized into cells by intracellular endocytosis and thus have been successfully investigated by several groups as anti-cancer drugs,[13] protein[14] and gene delivery vehicles.[15] Although silica based drug delivery system has been explored more in the field of biomedical applications still there remain some difficulties for large scale fabrication and industrial/clinical translations.[16] Apart from this, construction of a smart mesoporous nanoplatform which can simultaneously perform as a diagnostic imaging and stimuli-responsive anticancer drug-release is still in its infancy. As compared to mesoporous silica, mesoporous carbon nanoparticles (mCN) are less toxic and biocompatible.[17]

Furthermore, the mCN have also high surface area and large pore diameter. In contrast mCN have been less exploited as a drug delivery carrier in the field of biomedical applications as probably due to the hydrophobic nature of the matrix. However, a few reports have been published on ordered mesoporous carbons (OMC) as an effective drug delivery carrier due to the following facts. First, OMC fabricated by conventional methods usually have irregular particle shape with a large average size (>1 mm).[18] These randomly aggregated particles with large size cannot be effectively taken up by most types of cells. Second, those OMCs could hardly be dispersed in aqueous solution due to their inherent hydrophobicity, which in turn makes the intravenous administration of drugs and their circulation in blood almost impossible. So, it is still a great challenge to prepare mCN with a uniform size below

200 nm and hydrophilicity for good water dispersibility. Recently, Sun and Li[19] have reported one hydrothermal synthesis route for fabricating monodisperse carbon microspheres with a hydrophilic surface and good stability in aqueous systems. Unfortunately, due to nonporous structure and large particle size of the resultant material, it cannot be used as anti-cancer drug carriers. Recently, Zhu et al. synthesized mesoporous carbon nanospheres (mCNs) with small diameters of ~90 nm that can effectively regulate the release of anticancer drugs in response to a pH change.[20]

On the other hand, luminescent magnetic carbon spheres are newcomers to the world of nanomedicines and have shown great impact in the field of magnetic drug targeting and imaging applications. Huang et al have reported the synthesis of graphitic carbon@silica nanospheres with dual ordered mesopores for cancer targeted doxorubicin delivery and photothermal therapy.[21] Recently, our research group has published fabrication of luminescent magnetic mesoporous silica nanoparticles decorated with carbon dots which have been successfully used in multifunctional applications such as a T_2 contrast agent in MRI, fluorophore in luminescence imaging and for targeted delivery of anticancer drug camptothecin.[22] Instances have also been reported to enhance the luminescence property of carbon shells by doing nitrogen or other heteroatoms.[23]

Doxorubicin (DOX) is one of the commonly used chemotherapeutic agents (the p*Ka* of its amino group is 7.6) and highly toxic to humans and result in severe suppression of hematopoiesis, and gastrointestinal and cardiac toxicity.[24, 25] Hence, the development of an appropriate delivery vehicle for DOX and simultaneous monitoring of the therapeutic response through MRI and/or fluorescence imaging would provide important feed back towards the disease treatment. Taking the advantage of significant π-π stacking interaction of aromatic ring of DOX at different pH values based on its nonionized and ionized states with mesoporous carbon materials,[20] we design highly hydrophilic magnetic mesoporous carbon nanoparticles which may exhibit significant interaction with anticancer drug doxorubicin.

In the present study, we have focused on the development of highly luminescent magnetic nanoparticles by employing superparamagnetic $CoFe_2O_4$ as magnetic component and mesoporous carbon as luminescent component. Mesoporous carbon was synthesized by carbonization of resorcinol-formaldehyde polymer (RF) on $CoFe_2O_4$@*m*SiO_2 nanospheres which were prepared by employing an in situ polymerization of resorcinol and formaldehyde on $CoFe_2O_4$@mSiO_2 seeds in aqueous solutions. We choose RF as a polymer shell because it provides large number of aromatic π- electrons after carbonization for π-π stacking with small aromatic anticancer agent doxorubicin. The hydrophilicity of as synthesized $CoFe_2O_4$@mCs was increased by simple thermal activation in oxygen atmosphere at 300ºC without using any harsh chemical for oxidation. The silica template was removed to form mesoporous magnetic carbon nanospheres ($CoFe_2O_4$@mC). The DLS and zeta potential studies overtime ensure excellent stability of the nanoparticles in physiological medium. The in vitro cytotoxicity of the drug carrier as well as intracellular uptake and cell apoptosis were evaluated in HeLa cells through confocal microscopy. The pH dependent drug release has been investigated by using UV spectrophotometer. The possible application of the developed multifunctional particles was also evaluated through MR imaging.

6.2. Experimental

Materials

$Fe(acac)_3$, $Co(acac)_2$, oleic acid, oleylamine, Doxorubicin hydrochloride (DOX.HCl) were obtained from Sigma Aldrich. Tetraethyl orthosilicate (TEOS), cetyltrimethylammonium bromide (CTAB), resorcinol, formaldehyde solution, ammonium nitrate were purchased from spectrochem India. All other reagents and solvents were used without further purification. Millipore water (18.2 M Ω cm) was used throughout the experiment.

Synthesis of monodisperse hydrophobic $CoFe_2O_4$ nanoparticles

$CoFe_2O_4$ nanoparticles were prepared by solvothermal method. Briefly $Fe(acac)_3$ (706 mg, 2 mmol), $Co(acac)_2$ (257 mg, 1 mmol) , 1,2 dodecanediol (2.023 g, 10 mmol), oleic acid (1.9 ml, 6 mmol) oleylamine (1.97 ml, 6 mmol) and benzyl ether (30ml) were mixed and stirred for 15 minutes at room temperature and then the total mixture was transferred to a teflon lined stainless steel autoclave for 10h at 190^0C. Then as synthesized mixture was allowed to cool to room temperature and $CoFe_2O_4$ nanoparticles were precipitated by adding ethanol. The precipitate was collected by magnetic separator and dried in vacuum for 48h.

Synthesis of cobalt ferrite nanoparticles embedded in mesoporous silica spheres ($CoFe_2O_4$@m-SiO_2)

20 mg of oleic acid stabilized monodisperse $CoFe_2O_4$ nanoparticles dispersed in 1.5 mL of chloroform was added to a 20 mL of aqueous solution containing 0.4 g of CTAB (1.096 mmol). After vigorous stirring, a homogeneous oil-in-water micro emulsion was obtained. The resulting mixture was heated at 60 ºC for 10 min induced evaporation of the chloroform of the solution, which generated aqueous phase dispersed nanoparticles. Then 20 mL of the resulting aqueous solution was diluted with 200 ml of water. After that 1.5 ml of NH_4OH solution, 0.15 ml of tetraethyl orthosilicate, were successively added drop wise to the diluted aqueous solution containing the $CoFe_2O_4$ nanoparticles. The resulting mixture was heated at room temperature for 3 h to ensue complete polymerization of silica. Then the particles were washed three times with ethanol to remove the unreacted species and dispersed in 20 mL of ethanol separated by using a magnetic separator (DynaMag-2, Invitrogen). CTAB was removed from the matrix by dispersing the as-synthesized nanoparticles in a solution of 160 mg of ammonium nitrate and 60 mL of 95% ethanol and heating the mixture at 60 °C for 15 min.[26] Nanoparticles were then washed with ethanol and separated using the magnetic separator.

Synthesis of $CoFe_2O_4$@$mSiO_2$@RF and $CoFe_2O_4$@mC

For polymer coating, 0.08 g of as obtained $CoFe_2O_4$@$mSiO_2$ was homogeneously dispersed in deionized water (10 mL). 0.035 g of resorcinol, 2.82 ml of ethanol and 0.01 mL of ammonia were stirred at 35 °C for 30 min to form a uniform dispersion. Then, 0.05 ml of formalin was added to the above solution. After 6 h, the total mixture was heated at 100 ºC for another 24 h. Then the entire mixture was cooled to room temperature overnight without stirring. $CoFe_2O_4$@$mSiO_2$@RF was collected by centrifugation and then repeatedly washed with water and ethanol. The obtained $CoFe_2O_4$@$mSiO_2$@RF was heated at 5°C min^{-1} from room temperature to 150 °C and kept at this temperature for 1 h under a nitrogen flow. The temperature was again raised at 5°C min^{-1} to 600 °C and maintained at this temperature for 2 h. $CoFe_2O_4$@$mSiO_2$@mC nanoparticles were obtained after the product was cooled to room temperature. After that mesoporous magnetic carbon nanospheres ($CoFe_2O_4$@mC) were formed by etching silicon dioxide with 2M sodium hydroxide solution.[27] The surface of $CoFe_2O_4$@mC was oxidized to -COOH by oxidation of $CoFe_2O_4$@mC in air at 300 ºC for 1 h.[28] After thermal treatment, particles were dispersed in aqueous medium, which is necessary for bio applications.

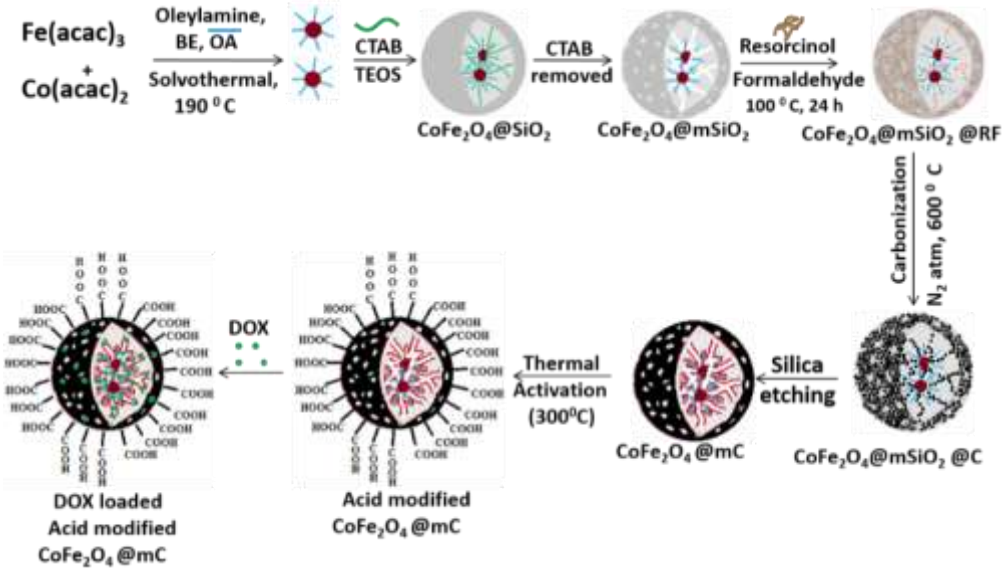

Fig. 6.1 Schematic representation of synthesis of $CoFe_2O_4$@MC.

Calculation of fluorescence quantum yield

The quantum yield (Φ) of the $CoFe_2O_4$@mC was calculated using quinine sulfate as reference. For calculation of quantum yield, five concentrations of each compound were made, all of which had absorbance less than 0.1 nm at 360 nm. Quinine sulfate (literature Φ = 0.54) was dissolved in 0.1 M H_2SO_4 (refractive index (η) of 1.33) while the nanoparticles were taken in water (η = 1.33). Their fluorescence spectra was recorded at same excitation of 360 nm. Then by comparing the integrated photoluminescence intensities (excited at 360 nm) and the absorbance values (at 360 nm) of the sample with the references quinine sulfate, quantum yield was determined. The quantum yield was calculated using the following equation

$$\Phi_x = \Phi_{ST} \ (m_x / m_{ST}) \ (\eta^2_x / \eta^2_{ST})$$

Where Φ is the quantum yield, m is slope, η is the refractive index of the solvent, ST is the standard and X is the sample. The quantum yield for $CoFe_2O_4$@mC is found to be 9.5.

Magnetic resonance imaging

The relaxation time (T_2) and transverse relaxivity (r_2) of the nanoparticle were measured with varying iron concentration (0.015-0.075 mM) using a clinical MRI scanner (MAGNETOM Symphony, SIEMENS) at a magnetic field of 1.5 T. T_2-weighted images were obtained with a spin echo multisection pulse sequence having fixed repetition time (TR) of 4000 ms with various echo times (TE) ranging from 105 to 291 (105, 116, 128, 139, 151, 163, 174, 186, 198, 291). The spatial resolution parameters were as follows: field of view (FOV) = 300×300 mm^2, matrix = 358×358, slice thickness = 4.0 mm. The MRI signal intensity (SI) was measured using in-built software. T_2 values were obtained by plotting the SI of each sample over a range of TE values. T_2 relaxation times were then calculated by fitting a first-order exponential decay curve to the plot. The fitting equation can be expressed as:

$$SI = S_0 e^{-TE/T_2} + B$$

Where SI is the signal intensity, TE is the echo time, S_0 is the amplitude, and B is the offset. The relaxivity value r_2 is determined from the slope of the linear plots of relaxation rate R_2 ($1/T_2$, s^{-1}) against Fe concentrations (mM).

$$R_2 = R_2^0 + r_2[Fe]$$

Loading and release of DOX

$CoFe_2O_4$@mCNs (20 mg) and DOX (10 mg) were added to 15 ml of water. The mixture was stirred at room temperature for 48 h. The drug loading capacity was measured by UV/Vis spectrophotometry with different time intervals. To verify drug release, $CoFe_2O_4$@mCNs were dispersed in buffers with different pH values and shaken at 100 rpm at 37 ºC. The supernatant after magnetic separation was collected for quantitative analysis by UV/Vis spectrophotometry.

In vitro applications

The cytotoxicity and intracellular uptake experiments were performed following the protocol already described in chapter 3.

6.3. Characterization

The synthesized materials were well characterized by using standard techniques as described in chapter-3. Additionally the Raman spectrum of as synthesized sample was recorded at ambient temperature on Renishaw in via Raman (UK make). Fluorescence microscopy images were captured using Axiovert 40 Carlzeiss India fluorescence microscope. Fluorescence spectroscopy was performed with a Horiba Fluoromax 4 spectrophotometer at different excitation energies ranging from 320 to 450 nm. Live-cell and plane particles imaging was done under Olympus FV-1000 confocal microscope with laser excitations of 405, 488 nm and 561 nm.

6.4. Results and discussion

Fig.1 illustrates the synthetic strategy for $CoFe_2O_4$@mCN nanospheres. The mesoporous silica coated $CoFe_2O_4$ nanoparticles were synthesized using CTAB as a surfactant where it plays dual role such as (1) for the transfer of hydrophobic $CoFe_2O_4$ to aqueous phase, (2) organic soft template for the formation of mesoporous silica spheres. The pores of the mesoporous silica can be filled up with resorcinol and formaldehyde by capillary force and in situ polymerization takes place in presence of ammonia.[29] The $CoFe_2O_4$@$mSiO_2$@RF nanocomposite spheres were further carbonized in a nitrogen flow to obtain $CoFe_2O_4$@$mSiO_2$@C. Removal of silica on washing with 5M NaOH gives highly luminescent magnetic $CoFe_2O_4$@MCN nanospheres which are sparingly dispersible in water. These hydrophobic $CoFe_2O_4$@MCN nanospheres were purified by thermal treatment in order to remove disordered carbon and also to oxidize their surface with –COOH groups as reported by Gabriel et al in case of carbon nanotubes.[28]

Investigation of phase by XRD and Raman spectroscopy

The phase purity of $CoFe_2O_4$, $CoFe_2O_4$@$mSiO_2$, $CoFe_2O_4$@$mSiO_2$@RF and $CoFe_2O_4$@mCNs were investigated through powder X-ray diffraction analysis (Fig. 6.2). In case of free cobalt ferrite nanoparticles five diffraction peaks were indexed at 30°, 35.40°, 43.16°, 57.01° and 62.63°, which correspond to reflection of plane of (220), (311), (400), (511), (440) indicating the inverse spinel structure of $CoFe_2O_4$ (JCPDS no 22-1086). The crystallite size was also calculated by using Debye Scherer equation and it was found to be 9.2 nm. $CoFe_2O_4$@$mSiO_2$ did not show any characteristics peaks within $2\theta = 15^o$-35^o indicating amorphous silicon dioxide phase coated on the surface of magnetic nanoparticles.[35] After polymer modification, broad peak in the range $2\theta=12^o$-25^o degree originated from amorphous phase of RF component which overlaps with the amorphous mesoporous silica range.[30] After carbonization the peaks corresponding to cobalt ferrite nanoparticles are intensify and shows decomposition of organic polymer.

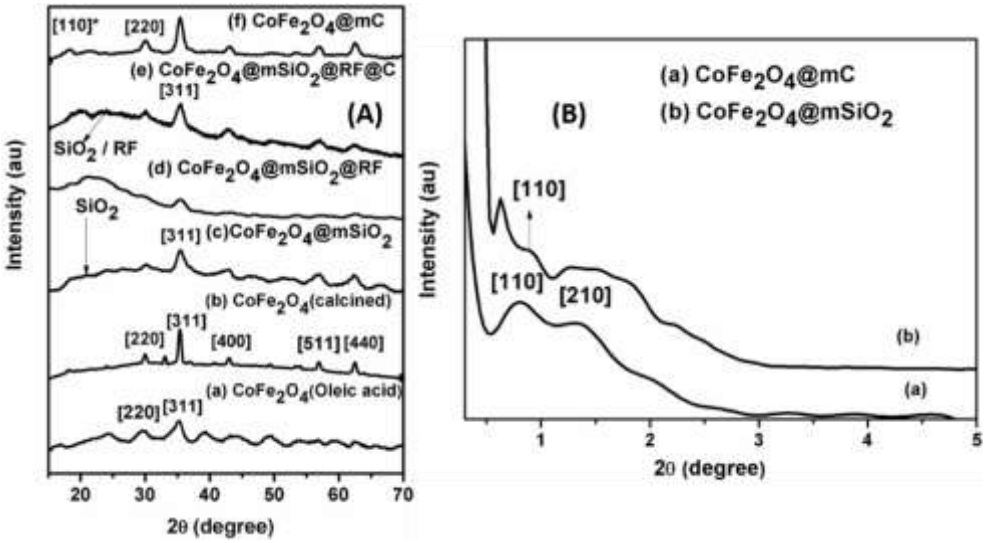

Fig. 6.2 (A) Wide angle diffraction pattern of $CoFe_2O_4$@mC nanoparticles at different stages of synthesis, *marks indicate the peaks from graphitic carbon (a) $CoFe_2O_4$ (Oleic acid), (b) $CoFe_2O_4$ (calcined), (c)$CoFe_2O_4$@$mSiO_2$, (d)$CoFe_2O_4$@$mSiO_2$@RF, (e)$CoFe_2O_4$@SiO_2@RF@C, (f) $CoFe_2O_4$@mC and: (B) Low angle diffraction pattern of (a) $CoFe_2O_4$@mC and (b) $CoFe_2O_4$@$mSiO_2$.

The absence of amorphous range and appearance of new plane at $(110)^*$ for graphitic carbon (JCPDS no 82-0505) indicates that silicon dioxide template has been completely removed after etching. The low-angle X-ray diffraction pattern of mC nanospheres exhibited two resolved diffraction peaks at 2θ values of 0.78º and 1.3º, respectively (Figure 6.2B), which can be indexed as the typical (110) and (210) reflections of a highly ordered body-centered cubic *Im3m* mesostructure.[21] The N_2 adsorption-desorption isotherm and corresponding pore diameter distribution curve well agree with it, having pore diameter 4 nm.

The bonding, order, and crystallinity of the materials are studied by Raman spectroscopy (Figure 6.3). Figure 6.3 reveals disordered graphitic materials, as suggested by the two Raman modes. The peak at 1594 cm^{-1} (G-band) corresponds to an E_{2g} mode of hexagonal graphite and is related to the vibration of sp^2 hybridized carbon atoms in a graphite layer. This means that the magnetic mesoporous carbon spheres are composed of graphitic carbon, and is related to sp^2 hybridized carbon atom in a graphite layer, which is consistent with the XRD results. The D-band at

about 1360 cm^{-1} is associated with the vibration of carbon atoms with dangling bonds in the plane termination of disordered graphite.[31] Due to this graphite with defects aromatic molecules can strongly interact with the basal plane of graphite via π-π stacking. The peak at 2702 cm^{-1} corresponds to the 2D band of the Raman spectrum, which shows signature of graphitic sp^2 materials. The Raman bands at 2950 cm^{-1} corresponds to the combination mode of the D-band and G-band.

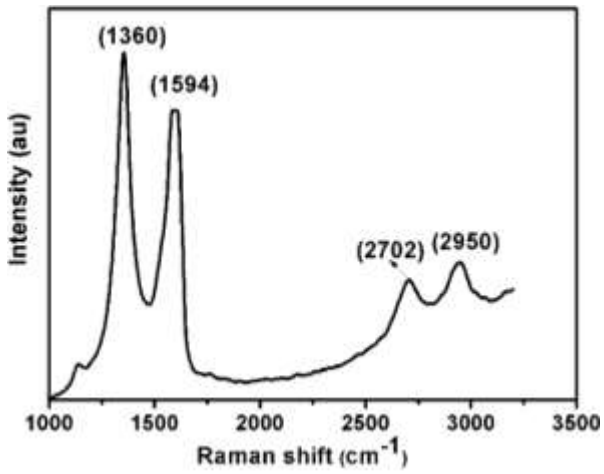

Fig. 6.3 Raman spectra of $CoFe_2O_4$@mC

SEM and TEM

SEM images indicate that size of $CoFe_2O_4mSiO_2$ is 55-60 nm and are spherical in nature (Figure 6.4a). FESEM image of $CoFe_2O_4$@mC shows that the magnetic carbon nanoparticles are spherical in nature and size varies from 100-130 nm. TEM image of $CoFe_2O_4$@mCNs is found to be 100-140 nm and the particles are porous in nature (Figure 6.4c).

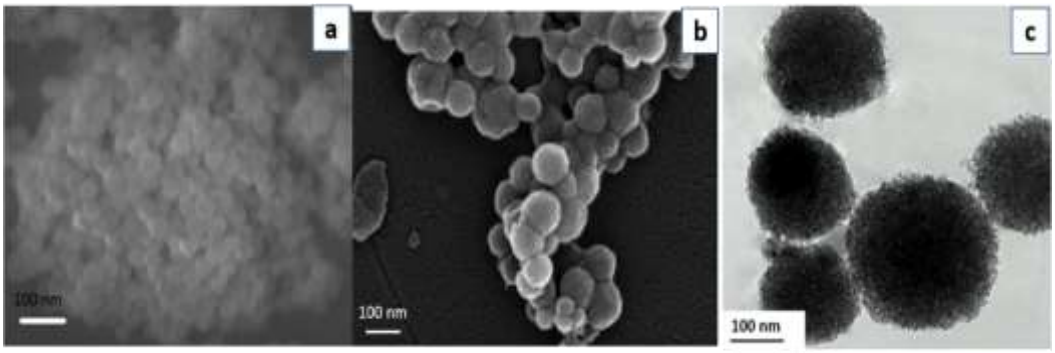

Fig. 6.4 (a) SEM image of$CoFe_2O_4$@$mSiO_2$ (b) FESEM image of $CoFe_2O_4$@mCNs (c) TEM image of $CoFe_2O_4$@mC

Hydrodynamic size and zeta potential

An investigation on hydrodynamic size after each step of modification of magnetic nanocomposites and stability of drug adsorbed DOX@$CoFe_2O_4$@mC was carried out using dynamic light scattering (Figure 6.5) in PBS. $CoFe_2O_4$@*m*SiO_2 shows the presence of stable non aggregated particles with hydrodynamic size 52 nm, PDI<0.2. After polymer modification the particle size was found to be 70 nm, PDI<0.3. The size of final product, magnetic mesoporous carbon nanoparticles after surface modification with acid group ($CoFe_2O_4$@*m*C-COOH) and DOX adsorbed $CoFe_2O_4$@mC@DOX was found to be 71 nm and 95 nm with a narrow size distribution. Again, the stability of DOX@$CoFe_2O_4$@mC were studied by measuring hydrodynamic size against time shows that there is almost no significant change of hydrodynamic size even after several weeks. This observation implies that such stable drug adsorbed particles can be circulated in blood stream for a long period.

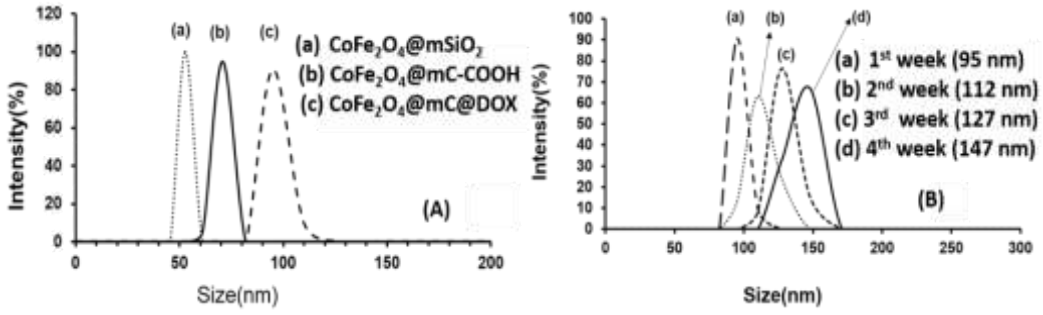

Fig. 6.5 (A) Particle size distribution at each step of modification (B) Stability of DOX@$CoFe_2O_4$@mC after several weeks.

In case of $CoFe_2O_4$-mCNs the surface charge varied from 40 mV at lower pH (2) to -11.2 mV at pH (11.2). After thermal activation the surface charge increases significantly in negative direction, with increase in pH indicating the presence of –COOH groups on the surface (Figure 6.6).

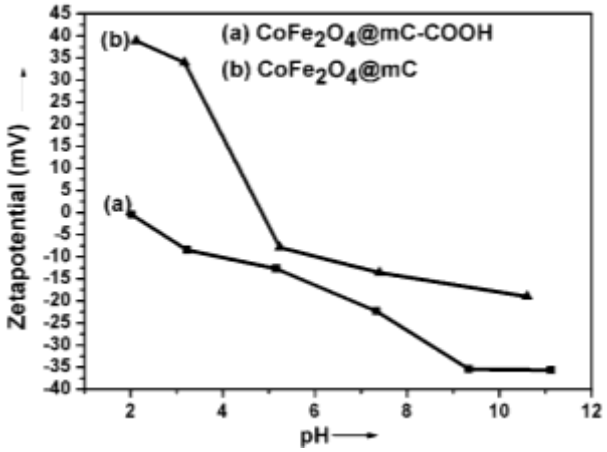

Fig. 6.6 Change in zeta potential of (a) $CoFe_2O_4$@mC-COOH and (b) $CoFe_2O_4$ @ mC nanoparticles with time.

N_2 adsorption – desorption study

Nitrogen sorption experiments were conducted to investigate further the porous nature of the $CoFe_2O_4$@$mSiO_2$ nanoparticles and $CoFe_2O_4$@mC. A comparison of N_2 adsorption-desorption isotherms of $CoFe_2O_4$@$mSiO_2$ and $CoFe_2O_4$@mC has been represented in Figure 6.7. All the samples reveal type IV isotherms which is a characteristic feature of mesoporous samples. The BET surface area of the as synthesized $CoFe_2O_4$@$mSiO_2$ and $CoFe_2O_4$@mC was found to be 925 m^2/g and 542 m^2/g. In case of $CoFe_2O_4$@$mSiO_2$ nanoparticles, the mesopores were formed due to the removal of soft template CTAB and aggregation of spherical particles. After polymer coating, the surface area of $CoFe_2O_4$@$mSiO_2$ nanoparticles decreases to 236 m^2/g, due to blocking of the pores.

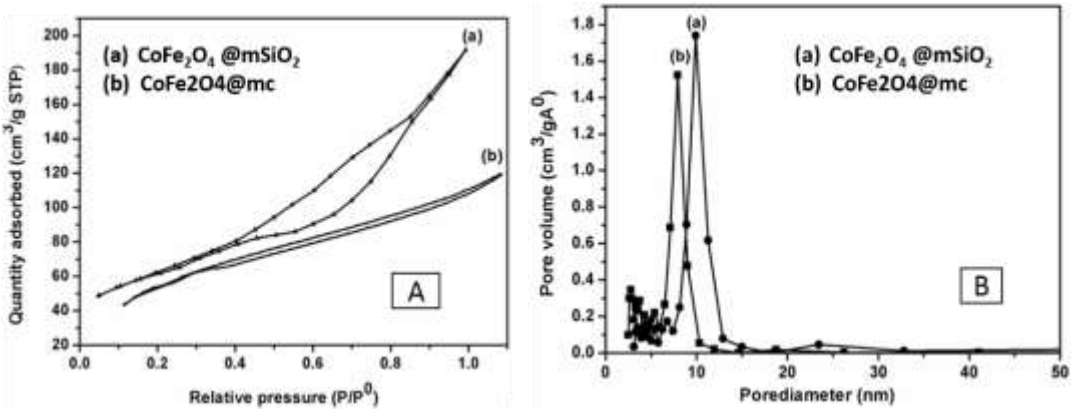

Fig. 6.7 (A) Nitrogen adsorption-desorption isotherm and (B) pore size distribution of $CoFe_2O_4$@$mSiO_2$ and $CoFe_2O_4$@mC nanoparticles.

In case of $CoFe_2O_4$@mC, the surface area appreciably increases due to the removal of hard template silicon dioxide in the etching process, which indicates the opening of pores. BJH shows a narrow pore size distribution and is found to be 10 nm for $CoFe_2O_4$@$mSiO_2$ and 8 nm for $CoFe_2O_4$@mC. Such type of unique structures having large surface area and pore size are advantageous for maximum adsorption of small drug molecules.

FTIR

Figure 6.8 shows FTIR spectra at various stages of synthesis of DOX loaded $CoFe_2O_4$@mC. The broad band located at 3450 cm^{-1} is the stretching absorption peak of −OH and the broad peak appears in the lower region (500-600 cm^{-1}) is due to metal-oxygen stretching vibrations. The sharp peaks appeared at 1080 and 797 cm^{-1} corresponds to asymmetric and symmetric stretching vibration of the Si-O-Si bond respectively. The peak showed at 2910 cm^{-1} is due to the methylene proton of CTAB for $CoFe_2O_4$@SiO_2/CTAB, which was disappeared in case $CoFe_2O_4$@$mSiO_2$ after washing with ammonium nitrate solutions. In case of figure 6.8(d-g) the bands at 1600, 1400 and 879 corresponds to the characteristic absorption bands of the benzene rings. After thermal activation of $CoFe_2O_4$@mCNs, a peak corresponds to the

carbonyl group of acids appears at 1710 cm^{-1} indicates the presence of surface –COOH groups.

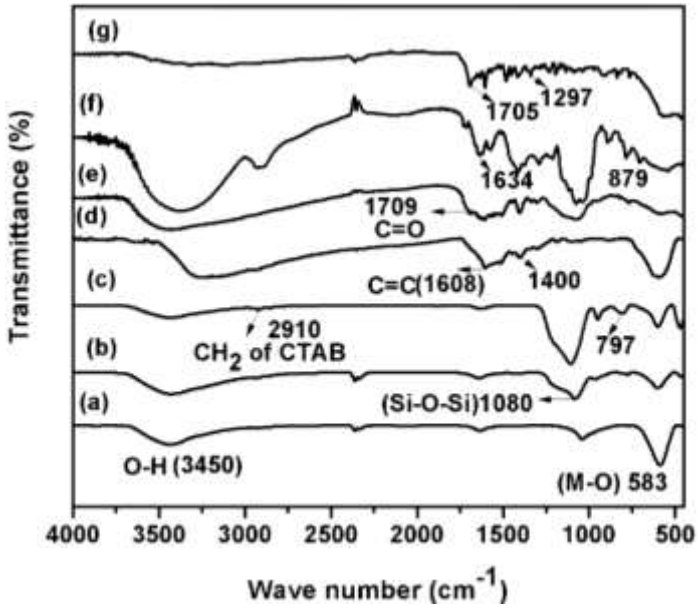

Fig. 6.8 FTIR spectra of (a) $CoFe_2O_4$, (b) $CoFe_2O_4$@$mSiO_2$, (c) $CoFe_2O_4$@SiO_2/CTAB, (d) $CoFe_2O_4$@mC, (e) $CoFe_2O_4$@mC/COOH, (f) DOX and (g) $CoFe_2O_4$@mC@DOX.

XPS

X-ray photoelectron spectra were further used to confirm the surface composition of $CoFe_2O_4$@mC. The different binding energy of C1s, O1s, Co2p and Fe2p electrons are shown in Figure 6.9. The spectrum of C1s can be deconvoluted into four single peaks which correspond to C-C (284.98 eV), C-O (285.97), C=C (284 eV) and C=O (289.2 eV) functional groups, which have a good consistence with the results of FTIR.[32] The spectrum of O1s further confirms the four characteristic oxygen states as shown in FTIR, such as C-C=O(530.4), C-C-O(531.4), O-H(532 eV), C=O/COOH(533.3 eV). The peak appearing at 284 eV indicates the presence of aromatic unsaturated carbon containing π electrons which is responsible for the adsorption of anticancer drug doxorubicin by π- π stacking. The peak at 533.3 eV of O1s and 289.2 eV of C1s validate the generation of carboxylic group on the surface of magnetic mesoporous carbon nanoparticles after thermal activation in oxygen atmosphere. Also $Co2p_{3/2}$ and $Co2p_{1/2}$ electrons show binding energy at 779 and

795.3 eV associated with corresponding shake ups at 785 and 801 eV.[33] In addition to this the asymmetric nature of the peak is ascribed to Co^{2+} present in Octahedral/tetrahedral sites.[34] Fe2p region shows two peaks at 713.5 and 727.6 eV which is consistent with Fe2p binding energy for $CoFe_2O_4$ nanoparticles.

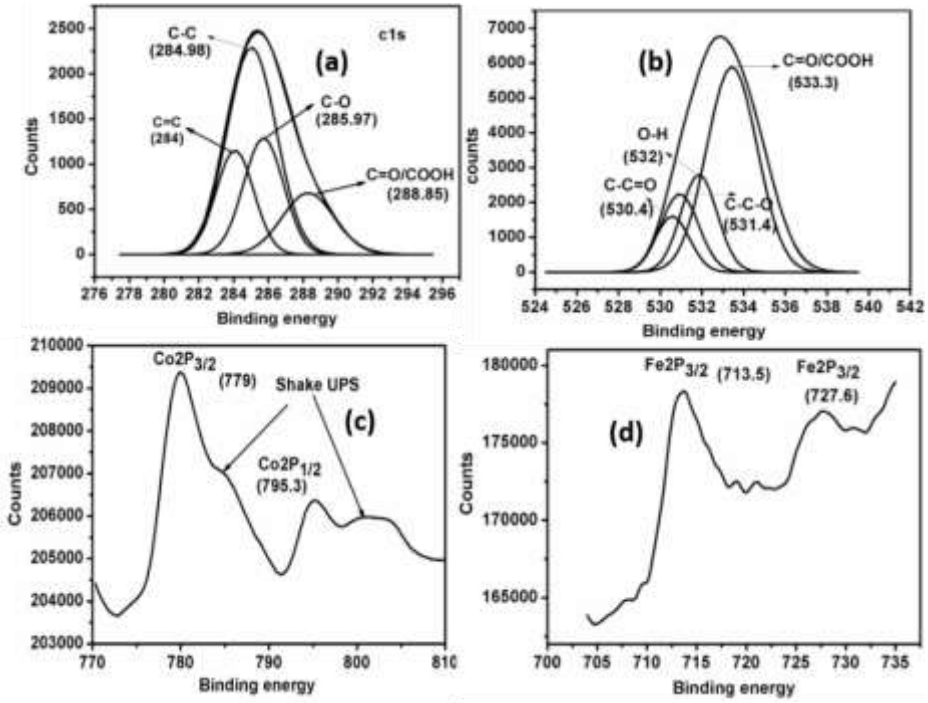

Fig. 6.9 High resolution scan corresponding to (a) C1s (b) O1s (c) Co2P (d) Fe2P binding energy.

Luminescence and magnetic properties

The aqueous solution of –COOH functionalized $CoFe_2O_4$@mCNs was yellow and transparent in day light but changes to intense green under UV excitation. The absorption in UV region is attributed to the presence of aromatic π orbitals. At a fixed excitation of λ_{ex}=360 nm, $CoFe_2O_4$@mC shows an emission peak at 500 nm. Furthermore, the unique property of excitation dependent PL was observed in case of $CoFe_2O_4$@mC in consistence with carbon quantum dots already reported by Mohapatra et al. and other researchers.[35,36] Luminescence of the as-prepared magnetic mesoporous carbon nanoparticles was studied at different excitation wavelengths, ranging from 300 to 500 nm (Fig 6.10). Similar to carbon dots the excitation

dependent PL may be ascribed to the presence of surface states. As evident from FTIR and XPS there are several functional groups like C=O, -COOH etc. present on the surface which creates a series of emissive traps between π and π* orbital of mesoporous carbon. PL intensity of the synthesized sample remains unchanged over pH 4.5 to 8 (Figure 6.11a). The measurement of fluorescence intensity with time shows mesoporous carbon does not show photo bleaching for hours (Fig. 6.11b). The PL quantum yield was found to be 9.5% which is significantly high compared to other magnetic carbon samples (Fig. 6.12). Laser confocal microscopy images show that these $CoFe_2O_4$@mC are excellent imaging agents. The excitation dependent luminescence gives rise several visible advantages in imaging. When the laser excitation was changed to 405, 488 and 561 nm, blue, green and red colors were observed respectively. In addition to this there was no reduction in luminescent intensity even after prolonged exposure.

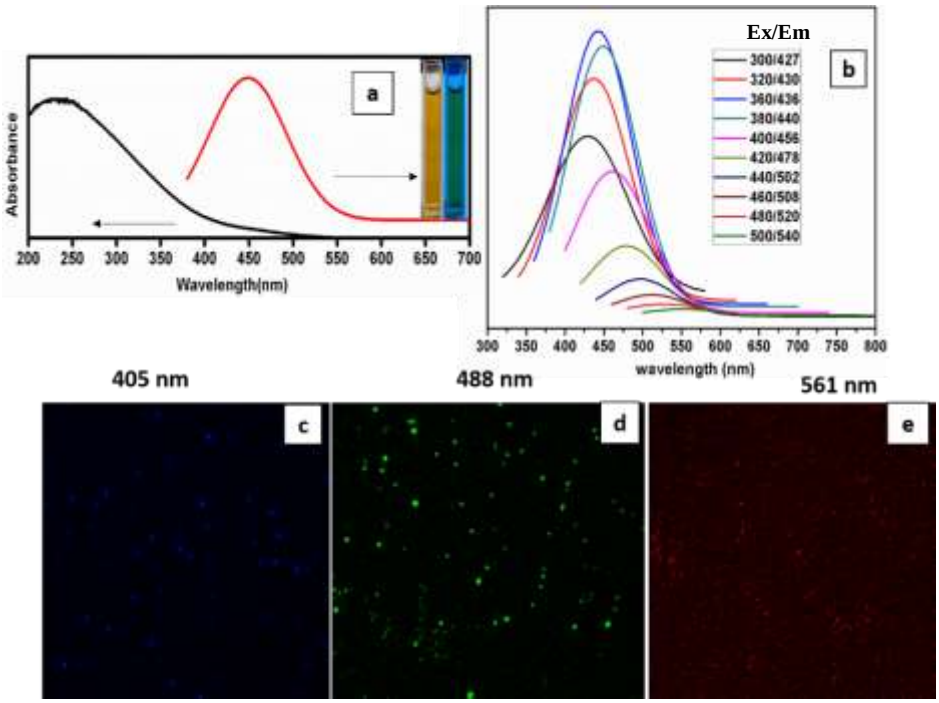

Fig. 6.10 (a) UV absorbance and PL emission spectra (λ_{ex}= 360 nm), inset optical images under daylight (left) and UV light (right), (b) emission spectra of $CoFe_2O_4$@mCN recorded for

progressively longer excitation wave length of 20 nm , confocal images of particles (c) 405 nm, (d) 488 nm, and (e) 521 nm.

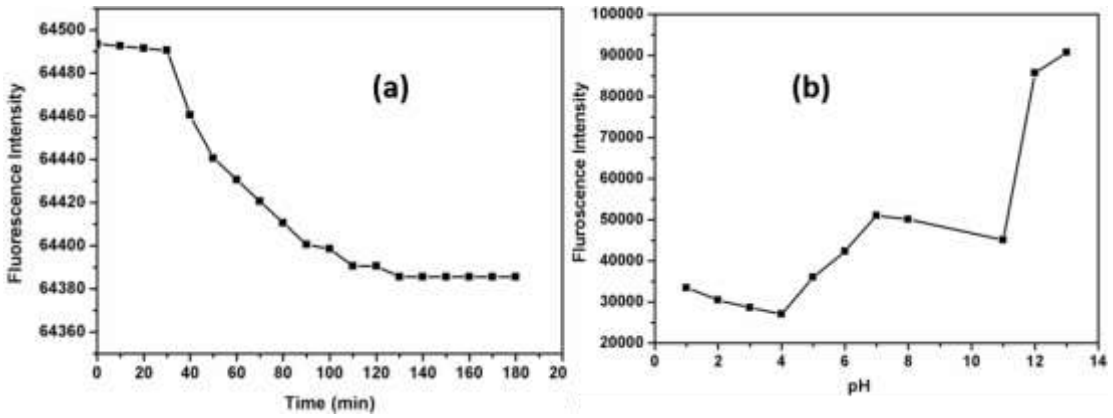

Fig. 6.11(a) Effect of time on fluorescence intensity of magnetic mesoporous carbon in DI water, (b) Effect of pH on the fluorescence intensity of magnetic mesoporous carbon.

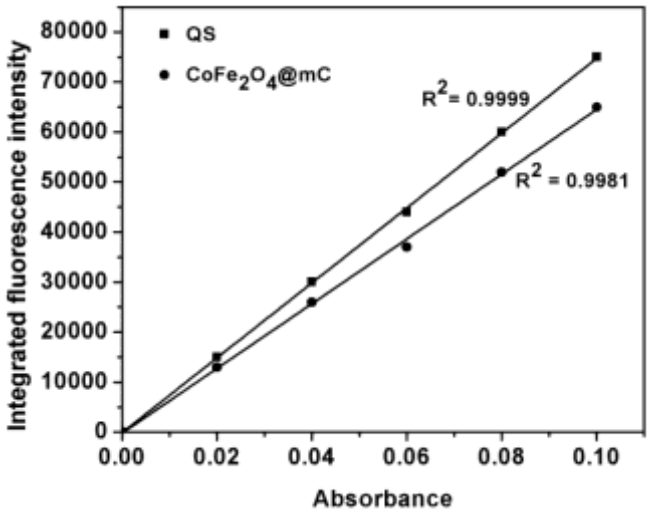

Fig. 6.12 Fluorescence intensity ~ UV absorbance of $CoFe_2O_4$@mC particles, **QS**: Quinine sulfate

$CoFe_2O_4$@mSiO_2@RF and $CoFe_2O_4$@mC show no hysteresis opening and hence are superparamagnetic at room temperature (Figure 6.13). The saturation magnetization values were found to be 20 and 51 e.m.u/g at high magnetic field (2T). The low Ms Value of $CoFe_2O_4$@mSiO_2@RF is attributed due to the presence of thick inert

material silicon dioxide and a polymer which is coated on the surface of cobalt ferrite nanoparticles. The substantial increase in saturation magnetization of $CoFe_2O_4$@mC has been attained after removal of nonmagnetic SiO_2 in the etching process. High saturation magnetization of $CoFe_2O_4$@mC along with superparamagnetism is highly desirable for application in magnetically guidable drug delivery and as a contrast-enhancing agent in MRI. Hence, $CoFe_2O_4$@mC would be a suitable material for the above applications.

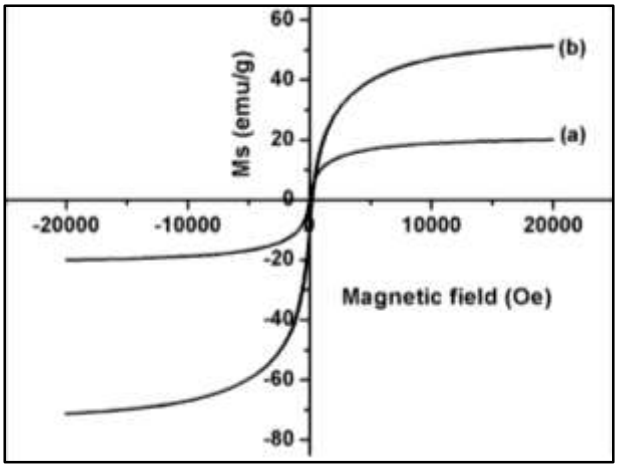

Fig. 6.13 Field dependent magnetization curve of (a) $CoFe_2O_4$@mSiO_2@RF and (b) $CoFe_2O_4$@mC.

Relaxometric measurements

As an initial investigation towards potential imaging functionality during chemotherapy, the visibility of DOX@$CoFe_2O_4$@mCNs was tested in water, PBS and minimal essential medium (MEM) by MRI scanner (1.5 T). As shown in Figure 6.14 with an increase in concentration of particles in the phantom solution, the signal intensity decreased, indicating that the magnetic mesoporous carbon spheres have generated magnetic resonance contrast on the transverse (T2) proton relaxation time weighted sequences due to the dipolar interaction of magnetic moments between the nanoparticles and proton in the water.[22] The T_2 relaxation time was inversely

proportional to the particle concentration, as expected. The transverse relaxivity (r_2) of the drug DOX adsorbed particles is found to be 380 mM^{-1} S^{-1}, resulting in better negative contrast effect than commercially available dextran coated cobalt ferrite such as feridex (120 mM^{-1} S^{-1}), combidex (65 mM^{-1} S^{-1}) and CLIO-tat (62 mM^{-1} S^{-1}).

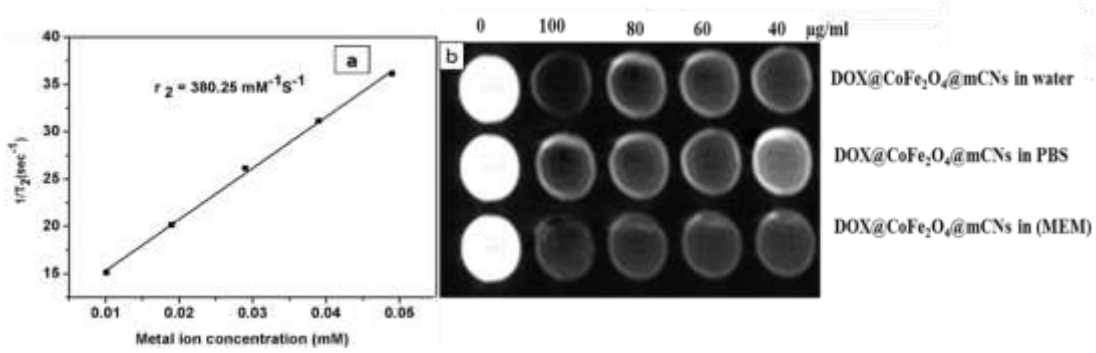

Fig. 6.14 Relaxivity (r_2) measurement of $CoFe_2O_4$@mCNs particles in water and MR phantom images of $CoFe_2O_4$@mCNs in three different medium.

DOX loading and pH dependent release

To further examine the doxorubicin (DOX) loading and delivery in the matrix $CoFe_2O_4$@mC, doxorubicin, a widely used anticancer drug, loaded into this matrix to form the product DOX@$CoFe_2O_4$@mC. The loading efficiency of DOX was measured to be as high as 86.1% due to the high BET surface area and pore volume of the prepared $CoFe_2O_4$@mC particles. Before drug loading to the matrix, free DOX exhibited high fluorescence intensity, while the fluorescence of extracted supernatant decreased significantly after DOX was bound to magnetic mC (Figure 6.15a). This high degree of fluorescence quenching is evidence of π-stacked DOX with magnetic mesoporous carbon.

The driving force acting here is π-π stacking between graphitic defects of aromatic carboneous framework and aromatic DOX molecules which contributes to the high loading capacity. Figure 6.15(b) shows the DOX release profile of the DOX@$CoFe_2O_4$@mC with three different pH in PBS at 37ºC, which shows initial burst release up 40% in first 10h which slowly increases up 70% with 100h at pH 4.

In vitro drug release experiments were carried out within buffer solutions with different pH (pH 7.4, 6.0 and 4.6). The acidic release medium was used to mimic the essential tumor acidic microenvironment. The amount of DOX released form the matrix over 10h at neutral pH condition was only 5.5%.

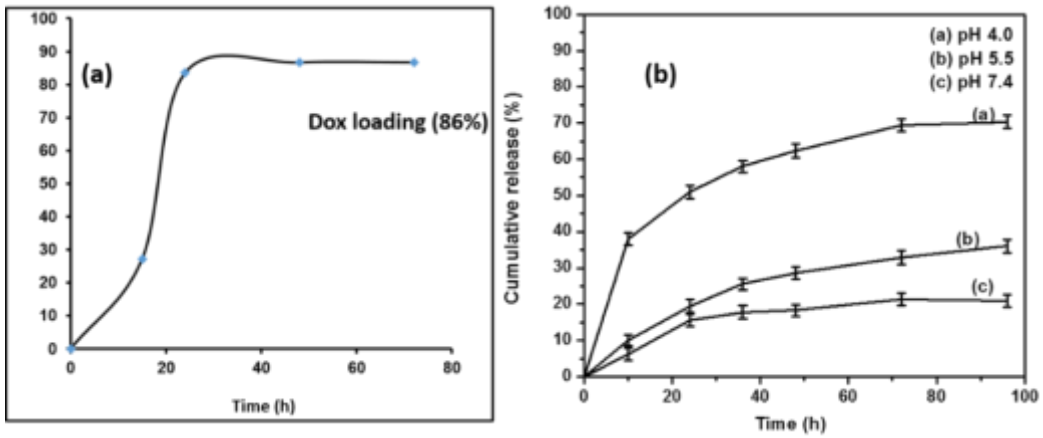

Fig. 6.15 (a) 86 % of total drug loaded on the $CoFe_2O_4$@mCNs@DOX and (b) pH-dependent drug-release behavior of DOX@$CoFe_2O_4$@mCNs. The highest percentage of DOX released was observed at pH 4.

However, 10% and 40% release percentages could be achieved within 10 h in pH 5.5 and pH 4 buffer solutions, respectively. Such a pH-responsive drug release behavior was based on the unique supramolecular π-π stacking between the carbonaceous framework and aromatic DOX molecules, which could be interfered with and broken in a mild acidic environment. Importantly, such a special non-covalent π-π stacking could also be broken by ionized state of doxorubicin. The above observation indicates that DOX is easier to load in basic solutions in its nonionized form, where as it is easier to release in acid solution

The doxorubicin loaded on the mesoporous magnetic carbon nanoparticles was also supported by decrease of fluorescence intensity of free DOX (Fig. 6.16). Here the concentration of free drug showing very high concentration and it was decreased after adsorption on the mesoporous carbon matrix by aromatic π-π stacking.

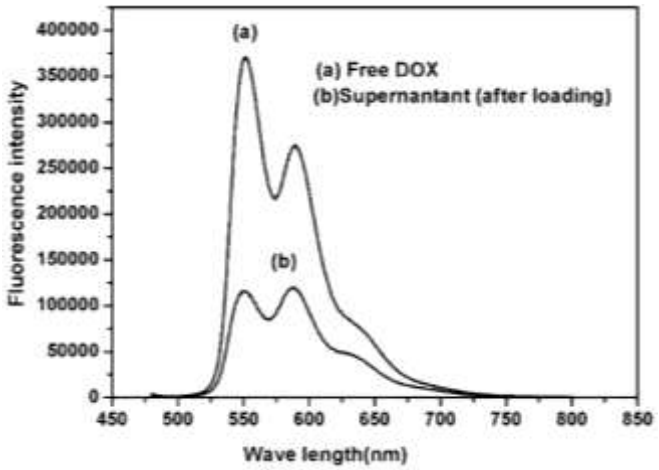

Fig. 6.16 (a) Fluorescence spectra intensity of free DOX and (b) supernatant after loading

Calculation of drug loading content and encapsulation efficiency

$$\text{Drug loading content (\%)} = \frac{\text{Weight of the drug in nanoparticles}}{\text{Weight of the nanoparticles}} \times 100$$

$$= \frac{6.023}{20} \times 100$$

$$= 30.115\%$$

$$\text{Encapsulation efficiency (\%)} = \frac{\text{Weight of the drug in nanoparticles}}{\text{Weight of the feeding drug}} \times 100$$

$$= \frac{6.023}{10} \times 100$$

$$= 60\%$$

The drug loading content and encapsulation efficiency of DOX was found to be 30.115% and 60% respectively.

Cytotoxicity

Here we investigate the cytotoxic effect of the $CoFe_2O_4$@mC, DOX and $CoFe_2O_4$@mC@DOX against HeLa cells to verify wheather the released DOX was

pharmacologically active. From Figure 6.17, it was observed that $CoFe_2O_4$@mC did not induce any significant change in the proliferation with a concentration up to 20 µg/ml with respect to the control, suggesting the absence of toxicity of the $CoFe_2O_4$@mC. The DOX loaded particles ($CoFe_2O_4$@mC@DOX) exhibit significantly higher cytotoxicity than free DOX, especially at relatively low DOX concentrations. This may be attributed to the easier uptake of the $CoFe_2O_4$@mC@DOX via endocytosis by HeLa cells as compared to the passive diffusion of free drug molecules which is believed to be highly important in minimizing the toxic side effect of free drugs to normal tissues/cells. The IC_{50} values of plain DOX and $CoFe_2O_4$@mC@DOX were found to be 10 µg/ml and 5 µg/ml.

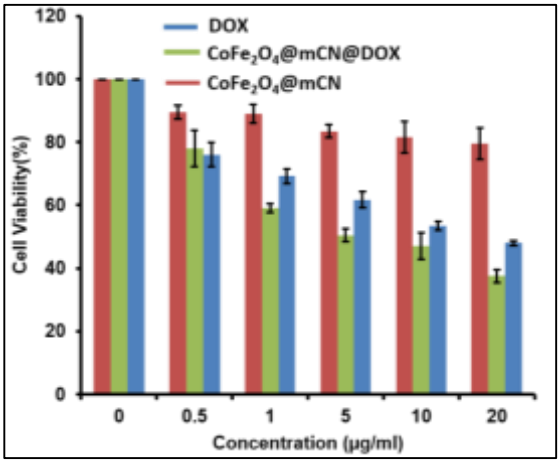

Fig. 6.17 Cytotoxicity assay of nanoparticles on HeLa cells.

Intracellular uptake and imaging

The satisfactory biocompatibility of $CoFe_2O_4$@mC nanospheres along with excellent luminescent properties makes it a reliable bioimaging agent. Figure 6.18 shows the fluorescence images of HeLa cells incubated with DOX loaded $CoFe_2O_4$@mC particles revealing that the $CoFe_2O_4$@mC particles can be easily internalized within and label the Hela cells. Further demonstrate that the mC nnosphers are accumulated and distributed uniformly in the whole region of the cytosol, which indicates that the $CoFe_2O_4$@mC can be well endocytosized by living

Hela cells, favoring the fluorescence imaging of the whole cells and drug delivery into the cytoplasm. To further investigate the bioimaging application under varied excitations, we varied the excitation wavelengths. For fluorescence excitation set at 360 nm, intense blue colour was observed.

When excitation light vary to 360 and 480 nm green and light blue colour were observed. In addition to his there was no significant loss in fluorescence intensity even after excitation for a prolonged time. All the precluded indicate that our designed $CoFe_2O_4$@mC nanospheres can be used to as a potential substitute to organic dyes in fluorescence imaging.

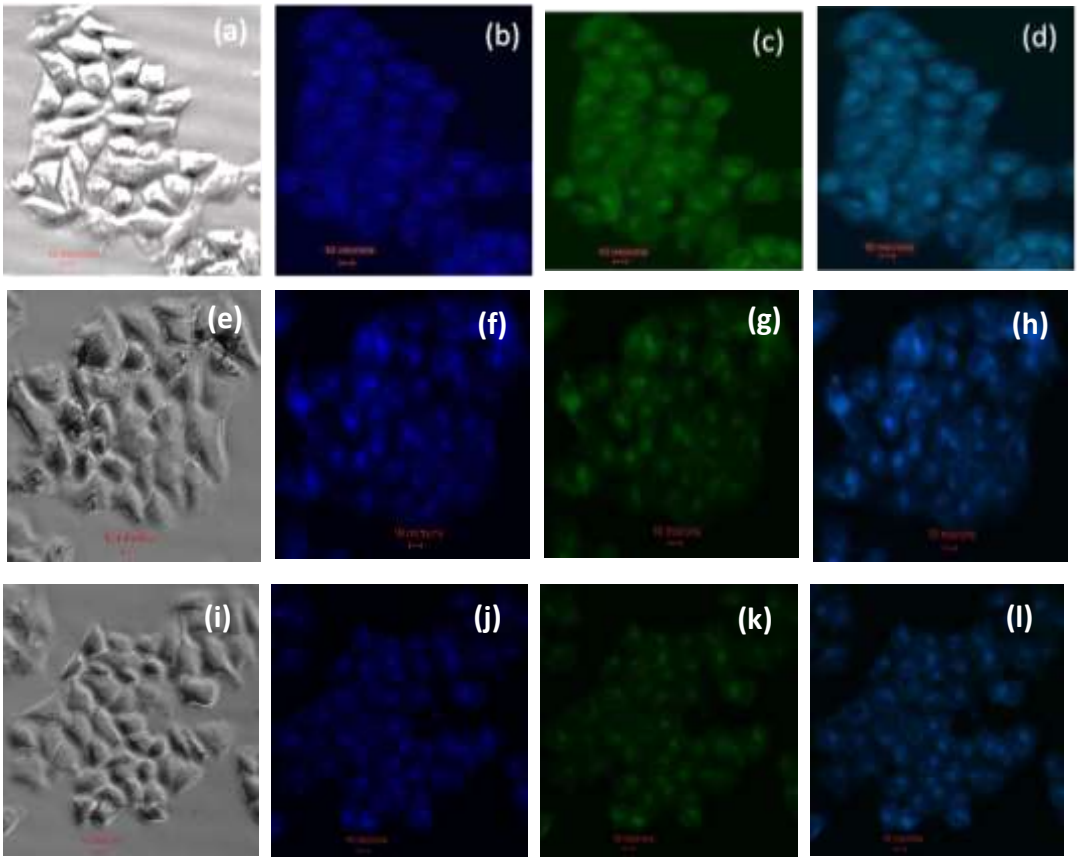

Fig. 6.18 (a) Fluorescence image of HeLa cells incubated with $CoFe_2O_4$@mC@DOX nanospheres for 2h in MEM, (b) image excited under λex = 360 nm and detected using UV filter, (c) excited under λex = 450 nm and detected using blue filter, (d) under λex = 470 nm

and detected using blue filter, (e) to (h) images taken after 1 h, (i) to (l) images taken after 3h at respective excitation wavelengths.

6.5. Conclusion

Simple and inexpensive magnetic mesoporous carbon-based multimodal theranostic nanoagents best owed with magnetic targeting, magnetic resonance, fluorescence imaging, high loading and controlled release of the anticancer drug doxorubicin have been developed. Due to surface modification with carboxylic acid groups the nanoparticles are highly stable in aqueous buffer. Our surface engineered design promotes a reliable strategy for the administration of doxorubicin. The dual optical and magnetic properties of the mesoporous spheres may be utilize in advanced imaging technologies to track the curative responses. This approach opens a possibility for application of magnetic carbonaceous nanocomposites for cancer treatment and may be of particular interest in pharmaceutical industries.

6.6. References

1. L. Li, F. Tang, H. Liu, T.Liu, N. Hao, D. Chen, Y. Tang and J. He, *ACS Nano.*, 2010, **4**, 6874-6882.
2. J. L. Vivero-Escoto, I. I. Slowing, B. G. Trewyn and V. S. Y. Lin, *Small*, 2010, **6**, 1952.
3. L. Yuan, Q. Tang, D. Yang, J. Z. Zhang, F. Zhang and J. Hu, *J. Phys. Chem. C*, 2011, **115**, 9926.
4. Y. Gao, Y. Chen, X. Ji, X. He, Q. Yin, Z. Zhang, J. Shi and Y. Li, *ACS Nano*, 2011, **5**, 9788.
5. S. Gai, P. Yang, C. Li, W. Wang, Y. Dai, N. Niu and J. Lin, *Adv. Funct. Mater.*, 2010, **20**, 1166.
6. I. Slowing, J. Viveroescoto, C. Wu and V. Lin, *Adv. Drug Delivery Rev.*, 2008, **60**, 1278.
7. Y. Zhao, B. G. Trewyn, I. I. Slowing and V. S. Y. Lin, *J. Am. Chem. Soc.*, 2009, **131**, 8398.
8. M. Manzano, M. Colilla and M. Vallet-Regi, *Expert Opin. Drug Delivery*, 2009, **6**, 1383.
9. (a) S. B. Wang, *Microporous Mesoporous Mater*., 2009, **117**, 1; (b) B. G. Trewyn, S. Giri, I. I. Slowing and V. S. Y. Lin, *Chem. Commun*., 2007, 3236.
10. C. H. Lei, P. Liu, B. W. Chen, Y. M. Mao, H. Engelmann, Y. Shin, J. Jaffar, I. Hellstrom, J. Liu and K. E. Hellstrom, *J. Am. Chem. Soc*., 2010, **132**, 6906.
11. Q. J. He, Z. W. Zhang, Y. Gao, J. L. Shi and Y. P. Li, *Small.*, 2009, **5**, 2722.
12. Q. J. He, J. L. Shi, M. Zhu, Y. Chen and F. Chen, *Microporous Mesoporous Mater*., 2010, **131**, 314.
13. (a) J. Roseholm, C. Sahlgren and M. Linden, J. *Mater. Chem.*, 2010, **20**, 2707; (b) C. P. Tsai, C. Y. Chen, Y. Hung, F. H. Chang and C. Y. Mou, *J. Mater. Chem*., 2009, **19**, 5737; (c) Z. M. Tao, B. Toms, J. Goodisman and T. Asefa, *ACS Nano.*, 2010, **4**, 789; (d) J. M. Rosenholm, E. Peuhu, J. E. Eriksson, C. Sahlgren and M. Linden, *Nano Lett.*, 2009, **9**, 3308.

14. I. I. Slowing, B. G. Trewyn and V. S. Y. Lin, *J. Am. Chem. Soc*., 2007, **129**, 8845.
15. A. M. Chen, M. Zhang, D. Wei, D. Stueber, O. Taratula, T. Minko and H. He, *Small*, 2009, **5**, 2673.
16. S. Zhang, X. Qian, L. Zhang, W. Peng and Y. Chen, *Nanoscale.*, 2015, **7**, 7632.
17. (a) B. Hu, K. Wang, L. H. Wu, S. H. Yu, M. Antonietti and M. M. Titirici, *Adv. Mater.*, 2010, **22,** 813; (b) R. Ryoo, S. H. Joo and S. Jun, J. Phys. Chem. B, 1999, **103**, 7743.
18. 10 T. W. Kim, P. W. Chung, I. Slowing, M. Tsunoda, E. S. Yeung and V. S.-Y. Lin, *Nano Lett.*, 2008, **8,** 11.
19. 11 Y. Fang, D. Gu, Y. Zou, Z. X. Wu, F. Y. Li, R. C. Che, Y. H. Deng, B. Tu and D. Y. Zhao, *Angew. Chem.*, Int. Ed., 2010, **49**, 7987.
20. J. Zhu, L, Liao, X. Bian, J. Kong , P. Yan, Y. Wang, K. Wang, R. Zhang and B. Liu *Small.*, 2012, 8, 2715.
21. Y. Wang, K. Wang, R. Zhang, X. Liu, X. Yan, J. Wang, E. Wagner and R. Huang, *ACS Nano*., 2014, **8**, 7870.
22. S. Sahu, N. Sinha, S. K. Bhutia, M. Majhic and S. Mohapatra, *J. Mater. Chem. B*, 2014, **2**, 3799.
23. S. Mohapatra, S. Sahu, N. Sinha and S. K. Bhutia, *Analyst*, 2015, **140**, 1221.
24. D. Morelli, S. Menard, M. I. Colnaghi, A. Balsari, *Cancer Res.*, 1996, **56,** 2082.
25. D. Vonhoff, M. W. Layard, P. Basa, H. L. Davis, A. L. Vonhoff, M. Rozencweig , F. M. Muggia, *Ann. Intern. Med.*, 1979, ***91,*** 710.
26. M. Liong, J. Lu, M. Kovochich, T. Xia, S. G. Ruehm, A. E. Nel, F. Tamanoi, and J. I. Zink, *ACS Nano*., 2008, 5, 889.
27. B. Guan, T. Wang, S. Zeng, X. Wang, D. An, D. Wang, Y. Cao, D. Ma, Y. Liu and Q. Huo, *Nano Research.*, 2014, **7**, 246.

28. G. Gabriel, G. Sauthier, J. Fraxedas, M. Moreno-Man˜a, M. T. Martı´nez, C. Miravitlles and J. Casabo´b, *Carbon*., 2006, **44**, 1891.
29. Y. Zhang, S. Xu, Y. Luo, S. Pan, H. Ding and G. Li, *J. Mater. Chem*., 2011, **21**, 3664.
30. S. Mohapatra, S. R. Rout, R. Narayan and T. K. Maiti, *Dalton Trans.*, 2014, **43**, 15841.
31. W. Li, L-S. Zhang, Q. Wang, Y. Yu, Z. Chen, C-Y. Cao and W-G Sang, *J. Mater. Chem.*, 2012, **22,** 15342.
32. S. Mohapatra, S. R. Rout, S. Maiti and T. K. Maiti, *J. Mater. Chem.*, 2014, **21**, 9185.
33. Q. Kong, L. Zhang, J. Liu, M. Wu, Y. Chen, J. Feng and J. Shi, *Chem. Commun.*, 2014, **50**, 15772
34. S. Mohapatra, S. R. Rout and A. B. Panda, *Colloids and Surfaces A: Physicochem. Eng. Aspects*., 2011, **384**, 453.
35. S. Sahu, B. Behera, T. K. Maiti and S. Mohapatra, *Chem. Commun*., 2012, **48**, 8835.
36. Q. Kon, L. Zhang, J. Liu, M. Wu, Y. Chen, J. Feng and J. Shi, *Chem. Commun*., 2014,**50**, 15772

Chapter-7

Summary and future scope

7.1. Summary

The development of nanoparticle based drug formulations for the administration of water insoluble anticancer drugs along with real-time monitoring of the treatment is under continuous investigation. In this regard, the work undertaken in this doctoral thesis addressed on the development of some smart multifunctional nanoagents which can be used for the administration of widely accepted anticancer drugs like doxorubicin, methotrexate, cisplatin, pemetrexed. Most importantly in all our developed formulations, the overall dimension of each multifunctional nanoparticle does not exceed 150 nm which is perfect for medical applications as discussed in section 1.3. The fluorescence as well as magnetic properties of these nanoparticles opens the possibility for monitoring the therapeutic response through fluorescence and/or magnetic resonance imaging. The major advantages of our developed multifunctional systems are summarized as follows.

Highly hydrophilic amine functionalized mesoporous MFe_2O_4 (Co, Mn, Ni) nanoparticles have been synthesized by a one-step solvochemical approach. Due to high surface area, presence of nanochannels, high dispersion stability in aqueous medium and high density of surface amine groups bioconjugation as well as incorporation of drugs has become facile. Compared to other synthesis process reported so far, our technology is easy, gives uniform mesoporous nanospheres and can be adopted to synthesize a number of magnetic ferrites. $CoFe_2O_4$ synthesized in chapter 1 has been utilized to develop multifunctional nanoparticle for the targeted delivery of anticancer drug methotrexate. This theranostic nanoagent offers combined advantages of superparamagnetism which is beneficial in MRI, receptor targeting capacity, optical imaging and pH-sensitive control release of anticancer drug methotrexate which has been first time reported. Due to specific targeting at the tumor site the therapeutic potential of the nanoparticle is enhanced. Magnetic amorphous calcium phosphate nanoparticle has been developed for folate receptor

targeted delivery of challenging anticancer drug cisplatin. Although few number of polymer and silica based nanoformulations for the delivery of cisplatin have been reported, none of them emphasize on the monitoring of the therapeutic response. In this context, choosing calcium phosphate as the carrier matrix along with our surface engineering technology has manifold benefits. First, calcium phosphate surface rigidly binds with phosphonic acid which ultimately holds cisplatin. Second, calcium phosphate becomes disintegrated at acidic surface resulting pH-sensitive drug release. For the first time we have developed theranostic formulations that can be used for monitoring therapeutic response of cisplatin using fluorescence and/or MR imaging. Novel mesoporous hollow spherical silica particles with a size of 130 nm having $CoFe_2O_4$ in its hollow cavity have been synthesized and explored for site specific co-delivery of pemetrexed and cisplatin. Due to incorporation of nanosized cobalt ferrite this nanoprobe has transverse relaxivity (r_2) 421mM^{-1} which is much better than commercially available iron oxide based contrast agents such as ferumoxytol (91 $mM^{-1}s^{-1}$) and feridex (120 $mM^{-1}s^{-1}$). Though in last couple of years few research groups have demonstrated the utility of luminescent carbon nanospheres as carriers for anticancer drugs, the integration of magnetic cobalt ferrite and luminescence has been rarely explored. Apart from this due to presence of surface carboxylic group the particle is water dispersible and stable for a prolong time. Such a uniquely designed nanosystem can open possibility for administration of other hydrophobic anticancer drugs.

7.2. Future scope

Although there are many exciting potential biomedical applications of multifunctional magnetic nanoparticles, considerable challenges and issues remain to be resolved. For instance, it is hard to accurately control the number of therapeutic entities present in the composite nanoparticle. Better synthetic strategies may be developed to fabricate multifunctional nanoparticles with precise composition,

reproducible surface functionalization and uniform surface modification. The scaling-up of the fabrication techniques is the most important for their pharmaceutical applications. Another challenge in the development of coatings involving active biomolecules for nanoparticles is to limit the overall size of particles to below 100 nm, since nanoparticles larger than 100 nm are rapidly cleared by the liver and spleen. Once their diagnostic and therapeutic purposes are achieved, these NPs should be eliminated by biological systems without any other detrimental effects. The long-term effects of these NPs and their conjugates on biological systems should be thoroughly studied *in vivo*. Toxicity of MNPs is multifactorial and depends upon their composition, physicochemical properties such as size and surface characteristics, route of administration, and dose. Also the benefit-to-risk ratio has to be balanced according to the intended medical or pharmaceutical application. Thus, from a regulatory standpoint, NPs safety has to be evaluated case-by-case.

The promise of hyperthermia as a minimal invasive treatment of malignant tumors has been well demonstrated. Magnetic hyperthermia has also been used in combination with chemotherapy for obtaining a still more efficient antitumor response. In all our cases $CoFe_2O_4$ has been successfully used as the magnetic component of the multifunctional system with low toxicity. Hence the developed systems may be evaluated as heat mediators in presence of an alternative magnetic field.

Similar to silica, carbon nanoparticles are nontoxic, biocompatible, and nonimmunogenic. Hence they may be extensively used for intracellular delivery of anticancer drugs. The excellent luminescence property of mesoporous carbon may be explored to fabricate fluorescence nanosensors for biologically important cations/anions/molecules.

List of Publications

1. One pot synthesis of uniform and spherically assembled functionalized MFe_2O_4 (M= Co, Mn, Ni) nanoparticles. Sasmita Mohapatra*, **Smruti R. Rout**, Asit B. Panda, ***Colloids and Surfaces A: Physicochemical and Engineering Aspect*. 2011, 384, 453-460. Impact factor: 2.11 citations: 26**
2. Monodisperse mesoporous cobalt ferrite nanoparticles: Synthesis and application in targeted delivery of antitumor drugs. Sasmita Mohapatra*, **Smruti R. Rout**, Tapas K. Maiti, Asit B. Panda, ***J. Mater. Chem*. 2011, 21, 9185-9193. Impact factor: 6.62 citations: 33**
3. Multifunctional magnetic calcium phosphate nanoparticles for targetd platin delivery. **Smruti R. Rout**, Tapas K. Maiti, Birendra Behera and Sasmita Mohapatra*, ***Dalton Trans*., 2012, 41, 10777-10783. Impact factor: 4.19 citations: 11**
4. Multifunctional mesoporous hollow silica nanocapsules for targeted co-delivery of cisplatin-pemetrexate and MR imaging. Sasmita Mohapatra*, **Smruti R. Rout**, Rajan Narayan and Tapas K. Maiti, ***Dalton Trans.*, 2014, 43, 15841-15850. Impact factor: 4.19 citations: 7**
5. Highly luminescent magnetic $CoFe_2O_4$@mC nanospheres for anticancer drug delivery and multimodal imaging. **Smruti R. Rout**, Rahul K. Das, Santoshi Nayak, Sudip K. Ghosh and Sasmita Mohapatra*, ***Langmuir* , 2016 (d.o.i 10.1021/acs.langmuir.5b03898). Impact factor: 4.45**

Conference Papers

1. Synthesis of multifunctional mesoporous cobalt ferrite nanoparticles for targeted delivery of antitumor drugs. **Smruti R. Rout and** Sasmita Mohapatra*,. "Chemference 2011" Indian Institute of Science Bangalore on September 23-24, 2011. **(Oral presentation).**
2. Multifunctional magnetic calcium phosphate nanoparticles for targetd platin delivery. **Smruti R. Rout** and Sasmita Mohapatra*, "National Conference on Chemistry in 21st Century" at MEMS Balasore on December 22-24, 2013. **(Oral presentation)**
3. Multifunctional magnetic mesoporous hollow silica nanocapsules for targeted co-delivery of cisplatin-pemetrexate and MR imaging. **Smruti Ranjan Rout,** and Sasmita Mohapatra* "International Conference on Overcoming the bottle necks in Drug discovery & development." At DSIN/Ranbaxy Gurgaon, India. March 25-27, 2014. **(Poster Presentation)**
4. One pot synthesis of uniform and spherically assembled functionalized MFe_2O_4 Nanoparticles. Smruti R. Rout and Sasmita Mohapatra* International Conference on innovative applications of chemistry in pharmacology and." At Berhampur University, Odisha India. February 4-6, 2015. **(Flash Poster Presentation)**